

ABSTRACT

MESSIMORE, JASON ADAM, The KamLAND Outer Detector. (Under the direction of Christopher R. Gould.)

The Kamioka Liquid Scintillator Anti-Neutrino Detector (KamLAND) consists of a one kiloton liquid scintillator Inner Detector (ID) and a three kiloton water Čerenkov Outer Detector (OD). The goal of KamLAND is to determine whether the flux and energy of electron anti-neutrinos generated by Japanese nuclear power reactors is consistent with the hypothesis that neutrinos have mass. The size and location of KamLAND allow for the first time a terrestrial test of the validity of the Large Mixing Angle solution to the Solar Neutrino Anomaly.

The anti-neutrinos are detected in the ID by a coincidence signal associated with the inverse beta decay reaction on a proton, followed by the subsequent capture of the neutron by another proton. The function of the OD is to tag cosmic ray muons and to suppress muon-induced neutron events in the ID which could otherwise be confused with real anti-neutrino events.

The Triangle Universities Nuclear Laboratory entered into the KamLAND collaboration to oversee the design, construction, testing, and operation of the OD. The OD consists of 225 twenty inch photomultiplier tubes (PMTs) arranged in four sections in a Tyvek lined cavity. The design of the detector is described, along with the testing procedures that were performed to determine the PMT operating characteristics. Simulations were performed to determine the muon-tagging efficiency of the OD as a function of the trigger conditions for an event. The neutron background caused by untagged muons was calculated for the current complement of PMTs. The efficiency of the OD was calculated to be 99.5% and the untagged neutron background was calculated to be 1.3 ± 0.4 for the 145.1 days of data-taking included in the first KamLAND result. The minimum value for the muon-tagging efficiency for the OD to be viable was determined to be 94.8%.

THE KAMLAND OUTER DETECTOR

by

JASON ADAM MESSIMORE

A dissertation submitted to the Graduate Faculty of

North Carolina State University

in partial fulfillment of the

requirements for the Degree of

Doctor of Philosophy

Department of Physics

Raleigh

2003

APPROVED BY:

Christopher R. Gould, Chair

John M. Blondin

Hugon J. Karwowski

Diane M. Markoff

Biography

Jason Adam Messimore

Personal

Born June 29, 1974

Washington, D.C.

Education

B.S. Nuclear Engineering, North Carolina State University, 1997

B.S. Physics, North Carolina State University, 1997

M.S. Physics, North Carolina State University, 2000

Thesis Title: *The KamLAND Outer Detector*

Academic Positions

Teaching Assistant, North Carolina State University, 1997–1999

Research Assistant, North Carolina State University, 1999–2002

Memberships

American Nuclear Society

Alpha Nu Sigma

American Physical Society

Sigma Pi Sigma

Omicron Delta Epsilon

Golden Key National Honor Society

Publications

First Results from KamLAND: Evidence for Reactor Anti- Neutrino Disappearance. K. Eguchi et.al. Physical Review Letters **90**, 021802 (2003).

Results of KamLAND Outer Detector Photomultiplier Testing. J.A. Messimore, H. Karowski, D.M. Markoff, K. Nakamura. KamLAND Note-01-03 (2001).

Depleted Uranium Hexafluoride Transportation Regulatory Analysis. J.A. Messimore. Lawrence Livermore National Laboratory, UCRL-AR-125086 (1996).

Contributed Abstracts

Characterization and Installation of the Photomultiplier Tubes for the KamLAND Outer Detector. J.A. Messimore, K. Nakamura. Presented at the Division of Nuclear Physics Meeting, Maui, HI (October 2001).

Test of KamLAND Photomultiplier Response and Tyvek Reflectivity. J.A. Messimore, L. DeBraekeleer, Y. Efremenko, C.R. Gould, O. Perevoztchikov, R.M. Rohm, W. Tornow. Presented at the Southeast Section of the American Physical Society Meeting, Chapel Hill, NC (November 1999).

Oral Presentations

Outer Detector NSUM Study via Simulated and Real Data. J.A. Messimore. Presented at the KamLAND Collaboration Meeting, Pasadena, CA (June 2002).

Gain Testing Procedure for 20" PMTs. J.A. Messimore. Presented at the KamLAND Collaboration Meeting, Waikiki, HI (September 1999).

Acknowledgements

I sincerely thank my advisor, Dr. Chris Gould, for his guidance and advice throughout the course of this work. I especially appreciate his understanding of my career goals and his help in directing me along the proper path to achieve them.

I wish to thank Dr. Diane Markoff for many helpful suggestions and taking the time to answer all of my questions concerning this research. Indeed, much of the manual work on the KamLAND project was performed together.

I thank Dr. Werner Tornow, Dr. Hugon Karwowski, and Dr. Kengo Nakamura for working side by side with me in Japan and their support in my effort. They have been the source of knowledge and enthusiasm for both my work and on KamLAND as a whole.

A supporting cast of fellow students also deserve mention for their contributions to the KamLAND project, which was not associated with their own research. Mr. Neil Simmons developed the cable splicing method and along with Mr. Micheal Hornish, spent several weeks in Japan testing and refurbishing pmts. Mr. Jamie Lush and Ms. Elizabeth Neidel spent many hours assisting in the cable production process.

In addition, I would like to thank Dr. Ryan Rohm for working with me on the simulations of the KamLAND detector. Without his guidance and knowledge of GEANT, I would not be in the position I am today.

Finally, Bret Carlin and Pat Mulkey of the electronics shop helped with the cables and electronics. In particular, they did excellent work with repairing and figuring out how to work the high voltage power supply that was to be used for the Outer Detector. Without

their work on this integral piece of hardware, much money and time would have been spent procuring a suitable replacement.

I express a deep thanks to my friends and family who have provided their support and understanding of the trials and tribulations one endures while working on such a project. Without their guidance and camaraderie, I would not have succeeded so splendidly.

Contents

| | |
|--|-----------|
| List of Figures | ix |
| List of Tables | xi |
| Chapter 1 Introduction | 1 |
| Chapter 2 The KamLAND Experiment | 5 |
| 2.1 Theory of Neutrino Oscillations | 5 |
| 2.2 Detection of the Neutrino | 10 |
| 2.3 Detector Location and Components | 12 |
| Chapter 3 The Outer Detector | 18 |
| 3.1 Čerenkov Radiation | 18 |
| 3.2 Neutron Spallation | 21 |
| 3.3 Relevance to KamLAND | 22 |
| Chapter 4 Photomultiplier Tube Testing | 25 |
| 4.1 Test Bench Setup | 26 |
| 4.2 Gain and Gain Response Function | 29 |
| 4.3 Analysis of the Single Photoelectron Peaks | 33 |
| 4.4 Photomultiplier Tube Testing Results | 35 |

| | |
|---|-----------|
| Chapter 5 Construction of the Outer Detector | 43 |
| 5.1 Refurbishment of the PMTs during Testing | 43 |
| 5.2 Cable Requirements and Splicing Design | 44 |
| 5.3 Cable Routing Scheme | 47 |
| 5.3.1 Signal Cables | 47 |
| 5.3.2 High Voltage Cables | 51 |
| 5.4 Cable Production | 51 |
| 5.5 PMT Frames and Shielding | 52 |
| 5.6 Installation of PMTs and Tyvek | 53 |
| Chapter 6 Startup | 57 |
| Chapter 7 Simulations | 61 |
| 7.1 GEANT Inclusions | 61 |
| 7.2 Single Photon Conversion Probability | 62 |
| 7.3 NSUM Verification | 65 |
| 7.3.1 NSUM Plot Features | 65 |
| 7.3.2 Analysis of Different NSUM Thresholds | 70 |
| 7.3.3 Efficiencies for Various Outer Detector Scenarios | 76 |
| 7.4 Neutron Background Study | 78 |
| 7.4.1 Inclusions for Neutron Studies | 79 |
| 7.4.2 Data Cuts | 81 |
| 7.4.3 Neutron Simulation Results | 82 |
| 7.4.4 Estimated Neutron Background in KamLAND | 88 |
| Chapter 8 Current Operational Status | 92 |
| Chapter 9 Conclusions | 96 |
| Appendix A PMT Test Results | 98 |

| | |
|---|------------|
| <i>CONTENTS</i> | viii |
| Appendix B PMT Positions | 111 |
| Appendix C Board and Channel Locations | 122 |
| Appendix D Deactivated PMTs | 129 |
| Bibliography | 132 |

List of Figures

| | | |
|------|--|----|
| 2.1 | Neutrino exclusion plot | 9 |
| 2.2 | Location of KamLAND and relevant neutrino sources | 13 |
| 2.3 | Muon flux at various depths | 15 |
| 2.4 | Cutaway view of the KamLAND detector | 16 |
| 3.1 | Polarization of a dielectric | 19 |
| 3.2 | Coherence of radiated wavelets | 20 |
| 3.3 | Energy spectrum of spallation neutrons | 22 |
| 3.4 | Feynman diagrams of real and fake events | 23 |
| 4.1 | Block diagram of electronics for high voltage testing | 27 |
| 4.2 | Fitted histogram for PMT #0245 | 28 |
| 4.3 | Charge per channel calibration for Bin 1 at 52 dB | 31 |
| 4.4 | Gain values for different positions of three tested PMTs | 32 |
| 4.5 | SPE spectrums for PMTs #0245 and #0021 | 34 |
| 4.6 | Gain versus high voltage plot for PMT #0245 with fit | 36 |
| 4.7 | PMT location guide 1 | 38 |
| 4.8 | PMT location guide 2 | 39 |
| 4.9 | Fitted versus Hamamatsu high voltage values at 0.6×10^7 gain | 40 |
| 4.10 | Adjusted fitted versus Hamamatsu high voltage values at 0.6×10^7 gain | 41 |

| | | |
|------|---|----|
| 5.1 | The modified ‘T’ connector | 46 |
| 5.2 | Layout of the dome area | 48 |
| 5.3 | Cable routing for top PMTs | 49 |
| 5.4 | Cable routing for bottom PMTs | 50 |
| 7.1 | Photoelectron spectrum for different photocathode conversion probabilities | 64 |
| 7.2 | NSUM plot for the Outer Detector | 67 |
| 7.3 | NSUM plots for the four Outer Detector regions | 68 |
| 7.4 | Starting points on the vertical axis for events in the four Outer Detector regions | 69 |
| 7.5 | NSUM plot of upper events with $z < 0$ cm | 70 |
| 7.6 | Angles of inclination for $z < 0$ cm events in upper region | 71 |
| 7.7 | Upper NSUM plot with $z < 0$ cm events removed | 72 |
| 7.8 | Comparison of normalized NSUM calculations with data for the four Outer Detector regions | 76 |
| 7.9 | Comparison of normalized NSUM plots with deactivated PMTs | 80 |
| 7.10 | Distance of stopped neutrons from the center of the Inner Detector | 84 |
| 7.11 | Distances to the center of the Inner Detector from various points | 85 |
| 7.12 | Histogram of E_{e^+} for fake events | 88 |
| 8.1 | Histogram of deactivated PMTs over time | 94 |

List of Tables

| | | |
|------|---|----|
| 2.1 | Isotopes in the KamLAND scintillator and selected properties | 12 |
| 4.1 | Position of a PMT during position testing | 30 |
| 4.2 | Rejected photomultiplier tubes | 42 |
| 6.1 | Final NSUM values and data rates for a one millivolt discriminator level . . | 60 |
| 7.1 | Breakdown of undetected events in Outer Detector | 65 |
| 7.2 | Efficiencies for various NSUM threshold settings | 73 |
| 7.3 | Data for under threshold events | 74 |
| 7.4 | Muon-tagging efficiencies for various scenarios of inactive PMTs | 77 |
| 7.5 | Muon-tagging efficiencies for various NSUM thresholds with 126 deactivated PMTs | 79 |
| 7.6 | Comparisons of various properties of water and KamLAND scintillator . . . | 81 |
| 7.7 | Quench factors used in the neutron background simulation | 83 |
| 7.8 | Scattering and capture of a single neutron in the fiducial volume | 86 |
| 7.9 | Distance between neutron capture and proton recoils | 87 |
| 7.10 | Simulated muon flux rates, average pathlengths, densities, and effective path- lengths | 89 |
| 8.1 | Deactivated PMTs by type and reason | 95 |
| 8.2 | The number of deactivated PMTs by region | 95 |

| | | |
|-----|---|-----|
| A.1 | Photomultiplier test results | 98 |
| B.1 | Installed PMT locations | 111 |
| C.1 | Electronics and high voltage board and channel listings | 122 |
| D.1 | Listing of deactivated PMTs in the Outer Detector | 129 |

Chapter 1

Introduction

Through the 1920s, very little was known about the makeup of the nucleus and the only particles that had been discovered were the proton, electron, and photon. This lack of knowledge caused much confusion among physicists when the process of beta decay was studied. The mysterious continuous energy spectrum of this decay threatened to break one of the sacred laws of physics, that of energy conservation. It was in 1930 when Wolfgang Pauli devised a ‘desperate remedy’ to save the law of energy conservation by introducing the concept of the neutrino.

Enrico Fermi’s successful formulation of the theory of beta decay via the weak interaction soon followed, putting the neutrino on solid theoretical footing. However, the neutrino did not become a ‘real’ particle until 1953 when the electron neutrino was experimentally discovered by Cowan and Reines during the Hanford Experiment [Rei53] and later confirmed with the Savannah River Neutrino Detector [Cow56]. The discovery of the muon neutrino in 1962 [Dan62] and the tau neutrino in 2000 [Kod01] completed the transformation of the theoretical neutrino types into three real particles.

Today, the neutrino continues to play a major role in physics. Because of their rare interaction with matter, neutrinos act as a record of the conditions that produced them, whether the events were the Big Bang, stellar fusion, or supernova explosions. If neutrinos have mass, then they make up a significant part of the energy density of the universe

because there are more neutrinos in the universe than any other type of particle except for the photon.

However, in the time since Pauli's brilliant deduction, the neutrino has remained an elusive particle, defiantly holding secret many of its properties. The difficulties encountered in determining these properties led John Updike to pen the following poem [Upd63]:

Neutrinos, they are very small
They have no charge and have no mass
And do not interact at all.
The earth is just a silly ball
To them, through which they simply pass,
Like dustmaids down a drafty hall
Or photons through a sheet of glass.
They snub the most exquisite gas,
Ignore the most substantial wall,
Cold-shoulder steel and sounding brass,
Insult the stallion in his stall,
And, scorning barriers of class,
Infiltrate you and me! Like tall
And painless guillotines, they fall
Down through our heads into the grass.
At night, they enter at Nepal
And pierce the lover and his lass
From underneath the bed - you call
It wonderful; I call it crass.

The prime motivation for studying neutrinos has been the Solar Neutrino Anomaly. The dynamics of the sun are well understood by theory and experiment such that the solar neutrino flux can be predicted with a high degree of accuracy. However, all experiments to date have consistently produced a discrepancy between the predicted and observed solar neutrino fluxes, with the measured flux being less than the predicted one. The most compelling particle physics explanation for this deficit is that neutrinos have mass and can therefore oscillate from one type of neutrino into another.

Therefore, one of the biggest questions in neutrino physics in the mid 1990's was whether it is possible to experimentally verify that neutrinos oscillate into other types of neutrinos as they travel through the universe. Results from non-accelerator based experiments

like Super-Kamiokande [Fuk98] and the Sudbury Neutrino Observatory [Ahm02] have recently shown that the answer to the above question is indeed ‘yes!’, leading to a push for higher sensitivity measurements.

To this end, a large underground detector named the Kamioka Liquid Scintillator Anti-Neutrino Detector (KamLAND) has been designed and built by a U.S.-Japan collaboration at the site of the former Kamiokande neutrino detector near Toyama, Japan. Taking advantage of the large anti-neutrino flux produced by nuclear power reactors located around the country, KamLAND has been able to increase experimental sensitivity to neutrino mass differences by two orders of magnitude over past experiments. This sensitivity allows the KamLAND collaboration to be the first to confirm or deny the most favored solution to the solar anomaly, the so-called Large Mixing Angle solution.

Underground experiments like KamLAND are based on the use of large quantities of organic liquid scintillator as the detection material and a major concern for these types of detectors is background suppression. Much effort was undertaken during the design and construction stages to make the background for KamLAND as low as possible.

The KamLAND detector is comprised of two sections. The central, Inner Detector is filled with one kiloton of liquid scintillator and is used to detect anti-neutrinos by the inverse beta decay of protons. Surrounding this central detector is a three kiloton detector filled with ultrapure water. The function of this Outer Detector is to tag through-going cosmic ray muons and to act as a passive shield against gamma rays and neutrons emitted from the surrounding rock.

The Triangle Universities Nuclear Laboratory (TUNL) took responsibility for the design and construction of the Outer Detector in KamLAND. This thesis describes the testing of detector components (Chapter 4), the construction process (Chapter 5), the simulations performed to optimize the Outer Detector’s trigger conditions (Section 7.3) and the simulations to determine the background due to fast neutrons produced by cosmic-ray spallation (Section 7.4).

KamLAND officially began taking data on January 22, 2002. The first set of results was published in January 2003, using 145.1 days of live time for the analysis [Egu03].

Chapter 2

The KamLAND Experiment

The initial goal of the KamLAND experiment is to study neutrino oscillations of the type

$$\bar{\nu}_e \rightarrow \bar{\nu}_x \tag{2.1}$$

using Japanese commercial nuclear power reactors as the source for electron anti-neutrinos. At maximum power, these nuclear reactors produce a very large flux of low energy isotropic electron anti-neutrinos of $1.3 \times 10^6 \text{ cm}^{-2}\text{s}^{-1}$ for $1.8 \leq E_{\bar{\nu}} \leq 8 \text{ MeV}$ at the detector site [Bus99]. 80% of this flux comes from sources in the range of 140 - 210 kilometers from the detector. The combination of this long baseline with the low neutrino energy will allow KamLAND to increase sensitivity to neutrino mass differences by two orders of magnitude over any previous terrestrial experiment.

2.1 Theory of Neutrino Oscillations

In the Standard Model of particle physics, there are twelve base particles that make up all matter and they are divided equally into two groups: quarks and leptons. These particles are divided into three families, each with one quark and one lepton doublet. The

particles in the first family make up ordinary matter, with the second and third families containing increasingly more massive particles.

A description of the weak interaction between the fundamental particles can be described by defining two sets of eigenstates that are related to each other by a set of unitary rotations. The weak eigenstates describe the transmutation of one member of a doublet into the other member via the charged current weak interaction. This interaction occurs when the W^\pm gauge particle is exchanged by the doublet members. The mass eigenstates are created when the doublet members interact with the Higgs field and acquire mass. The mass eigenstates are not identical to the weak eigenstates because the Higgs interaction causes the weak eigenstates to mix with each other, as in the case of quarks [Coo97].

As defined by the local symmetries of the weak force in the Standard Model, the lepton doublets consist of a charged, massive lepton (electron, muon, and tau) of charge -1 and a corresponding neutral, massless lepton, or neutrino, of the same name. The massless assumption for the three types, or flavors, of neutrinos means that the mass and weak eigenstates of the leptons are identical. However, if neutrinos have different non-zero masses, then it becomes a natural extension of the Standard Model to have neutrino mixing. In an analog to the quantum mixing of quarks, the weak states $|\nu_l\rangle$, can be written as a linear combination of the mass states $|\nu_m\rangle$,

$$|\nu_l\rangle = \sum_m U_{l,m} |\nu_m\rangle \quad (2.2)$$

where $U_{l,m}$ is the leptonic mixing matrix. For three flavors, $U_{l,m}$ is a unitary, 3×3 matrix.

To discern the effects of a non-diagonal mixing matrix, the propagation of neutrinos through a vacuum is considered. Using the simple case of two neutrino mixing (say ν_e and ν_μ), $U_{l,m}$ becomes

$$U_{l,m} = \begin{pmatrix} \cos \theta & \sin \theta \\ -\sin \theta & \cos \theta \end{pmatrix} \quad (2.3)$$

where θ is the quantum mixing angle. Writing Equation 2.2 out at time $t = 0$ gives

$$|\nu_e\rangle_{t=0} = \cos\theta|\nu_1\rangle + \sin\theta|\nu_2\rangle \quad (2.4)$$

$$|\nu_\mu\rangle_{t=0} = -\sin\theta|\nu_1\rangle + \cos\theta|\nu_2\rangle \quad (2.5)$$

where $|\nu_1\rangle$ and $|\nu_2\rangle$ are the corresponding mass eigenstates. For some time t later, the time evolution operator is applied to the above equations to get

$$|\nu_e\rangle_t = \cos\theta \exp(-iE_1t)|\nu_1\rangle + \sin\theta \exp(-iE_2t)|\nu_2\rangle \quad (2.6)$$

$$|\nu_\mu\rangle_t = -\sin\theta \exp(-iE_1t)|\nu_1\rangle + \cos\theta \exp(-iE_2t)|\nu_2\rangle. \quad (2.7)$$

The general probability of oscillation between two neutrinos is then calculated by

$$P(\nu_\alpha \rightarrow \nu_\beta, t) = |\langle \nu_\alpha | \nu_\beta \rangle|^2 \quad (2.8)$$

where α and β can represent either of two mixing neutrinos. Carrying through with the algebra in Equation 2.8 for $\nu_e \rightarrow \nu_\mu$ yields

$$P(\nu_e \rightarrow \nu_\mu, t) = \sin^2 2\theta \sin^2 \left(\frac{(E_2 - E_1)t}{2} \right) \quad (2.9)$$

where E_i is the relativistic energy associated with a particular mass eigenstate, m_i .

The momentum is the same for all $|\nu_m\rangle$ since evolution in time is being considered. Given that $E \gg m$, $E \approx p$, and that the distance traveled can be approximated by $L = ct$, the term $E_2 - E_1$ in Equation 2.9 becomes

$$E_2 - E_1 = \sqrt{m_2^2 + p^2} - \sqrt{m_1^2 + p^2} \approx \frac{\Delta m^2}{2p} \quad (2.10)$$

where $\Delta m^2 \equiv m_2^2 - m_1^2$ and is called the mass difference squared. Substitution into Equation 2.9 gives

$$P(\nu_e \rightarrow \nu_\mu, L) = \sin^2 2\theta \sin^2 \left(\frac{1.27 \Delta m^2 L}{E} \right) \quad (2.11)$$

where Δm^2 is measured in eV^2 , L is in meters, and E is in MeV. An often useful parameter, the oscillation length λ_{osc} , is defined as the distance between adjacent minima in P :

$$\left(\frac{1.27\Delta m^2 L}{E}\right) = \left(\frac{\pi L}{L_{osc}}\right). \quad (2.12)$$

Rearranging and solving yields

$$L_{osc} \approx \frac{2.48E}{\Delta m^2}. \quad (2.13)$$

Finally, the probability that the neutrino does not change flavor $P(\nu_\alpha \rightarrow \nu_\alpha, L)$, is given by $1 - P(\nu_\alpha \rightarrow \nu_\beta, L)$.

Because KamLAND cannot detect other flavors of neutrinos, the experiment focuses on measuring the loss in flux of electron anti-neutrinos produced by the nuclear reactors. This is known as a disappearance experiment. Of the factors on the right side, the baseline L and the neutrino energy spectrum E for each reactor is known. This leaves the mixing angle and the mass difference as the unknown parameters.

It is convenient to plot Δm^2 versus $\sin^2 2\theta$ to determine the regions that a particular neutrino detector has access to, as shown in Figure 2.1. Several experiments have explored various regions and have not seen evidence of oscillations, thereby excluding these areas as solutions for neutrino oscillations. There are three theoretical solutions to the solar neutrino anomaly whose regions have yet to be explored. They are named the Large Mixing Angle (LMA), Small Mixing Angle (SMA), and Vacuum solutions. The LMA solution is the favored choice with the best fit solution at the time of KamLAND construction showing $\Delta m^2 = 1.8 \times 10^{-5} \text{ eV}^2$ and $\sin^2 2\theta = 0.76$ [Bah98].

KamLAND's sensitivity to Δm^2 can be estimated by calculating the upper and lower limits for reactor neutrinos using Equation 2.13. For the upper limit, the shortest oscillation length L_{osc} is 140 kilometers and the highest possible reactor neutrino energy is 8 MeV. This gives $\Delta m^2 \approx 1.4 \times 10^{-4} \text{ eV}^2$. The lower limit uses the longest path of 210 kilometers and the lowest neutrino energy of 1.8 MeV to yield $\Delta m^2 \approx 2.1 \times 10^{-5} \text{ eV}^2$. KamLAND is expected to achieve values of $\Delta m^2 \leq 10^{-5} \text{ eV}^2$ [Bus99]. KamLAND's unique location among the neutrino sources allows it to be the first terrestrial experiment with a restricted

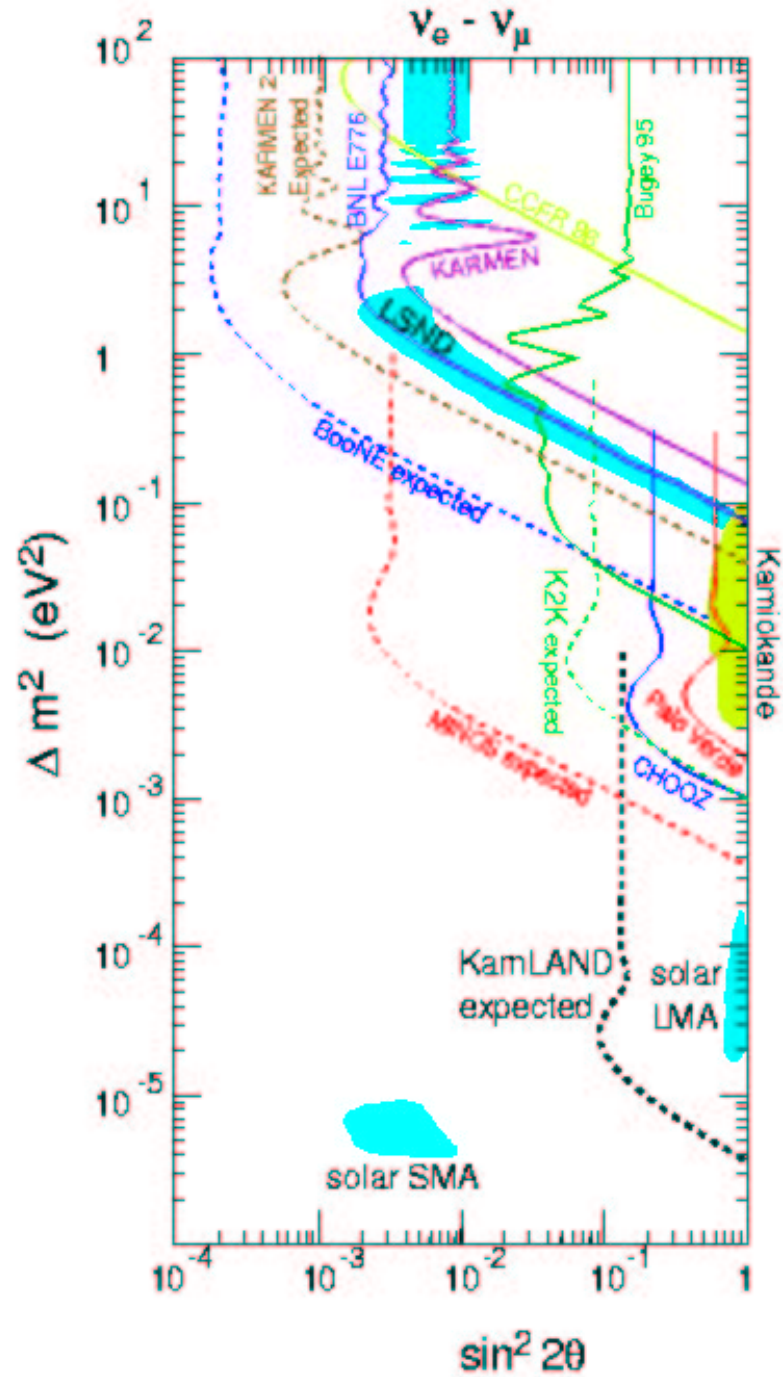


Figure 2.1: Neutrino exclusion plot as of March 1999. Allowed and excluded regions in the $\Delta m^2 - \sin^2 2\theta$ phase space for $\nu_e \rightarrow \nu_\mu$ oscillation. The existing limits are compared with current and future experiments and the regions obtained by interpreting the solar neutrino anomaly as due to oscillations. Limits are at 90% confidence levels.

range of Δm^2 that can isolate the LMA solution from the others. Thus, KamLAND is expected to decisively confirm or refute the validity of this solution.

2.2 Detection of the Neutrino

KamLAND uses the charged current reaction of inverse beta decay to identify an electron anti-neutrino capture by the following reaction:

$$\bar{\nu}_e + p \rightarrow n + e^+. \quad (2.14)$$

The positron energy is determined by the incident neutrino energy and the neutron - proton mass difference, $E_e = E_\nu - \Delta M_{n-p}$, where $\Delta M_{n-p} = 1.293$ MeV. Therefore, the energy threshold for this reaction is $\Delta M_{n-p} + m_e \simeq 1.8$ MeV.

To calculate the interaction cross section for this reaction, the general differential cross section formula is used,

$$\frac{d\sigma}{d\Omega}(a + b \rightarrow c + d) = \frac{1}{4\pi^2\hbar^4} |M_{if}|^2 \frac{p_f^2}{v_i v_f} \quad (2.15)$$

where $|M_{if}|$ is the matrix element between initial and final states involving integration over spins and angles of the particles, p_f is the center-of-mass system momentum of the final state particles, and v_i and v_f are the relative velocities in the center-of-mass system of a and b and of c and d . For inverse beta decay, the matrix element is the sum over the Fermi and Gamow-Teller terms, given by

$$|M_{if}|^2 = G (|M_F|^2 + |M_{GT}|^2) \quad (2.16)$$

where the Fermi constant $G = 1.17 \times 10^{-5}$ GeV⁻², $|M_F|^2 \simeq 1$ for total lepton spins = 0 and $|M_{GT}|^2 \simeq 3$ for total lepton spins = 1.

Using Equations 2.15 and 2.16 and integrating over $d\Omega$, the lowest order cross section for inverse beta decay is given by

$$\begin{aligned} \sigma(\bar{\nu}_e + p \rightarrow n + e^+) &= \frac{G^2}{\pi} (|M_F|^2 + |M_{GT}|^2) \frac{p^2}{v_i v_f} \\ &\simeq 10^{-43} E^2 \text{cm}^2. \end{aligned} \quad (2.17)$$

Here, v_i and v_f are $\simeq c$ and E is the positron energy in MeV [Per00]. For $E \approx 1$ MeV, this is a very small value, corresponding to a mean free path for the anti-neutrino of about 10^{20} cm, and can be compared to the low energy nucleon-nucleon scattering cross section of 20×10^{-24} cm².

The reaction in Equation 2.14 results in two signals, one prompt and one delayed that can be used to identify a neutrino event and eliminate many sources of background from consideration. The prompt signal occurs when the positron annihilates with an electron, producing two gamma rays with a total energy of 1.02 MeV plus the energy of the positron. The delayed signal occurs when the neutron thermalizes and is captured by another proton according to the reaction,



where the gamma has an energy of 2.2 MeV.

Because this delayed signal is essential for identifying a neutrino event, it is important to know the mean neutron capture time. A simple model developed by Fujikawa [Fuj01] provides an estimate of this capture time in the KamLAND scintillator through the equation

$$\frac{1}{\tau} = \frac{\rho N_A}{\sum_i n_i A_i} v_0 \sum_i n_i \sigma_i(v_0) \quad (2.19)$$

where τ is the capture time, ρ is the density of the scintillator, N_A is Avogadro's number, n_i and A_i are the relative number and atomic weight of isotopes i respectively, v_0 is the thermal neutron velocity of 2200 meters per second, and σ_i is the neutron capture cross section at v_0 for isotope i .

Since KamLAND's scintillator only contains hydrogen and carbon, Equation 2.19 can be simplified by using r_H , the hydrogen to carbon ratio,

$$\frac{1}{\tau} = \frac{\rho N_A}{r_H A_H + A_C} v_0 (r_H \sigma_H(v_0) + \sigma_C(v_0)). \quad (2.20)$$

Neutron capture cross sections at v_0 are measured by Brookhaven National Laboratory and tabulated in Report BNL325 [Bro02]. Table 2.1 lists the isotopes in the KamLAND

scintillator, their capture cross section, and the fraction of neutron captures. Only ^1H and ^{12}C need to be used, since $\sim 100\%$ of the captures occurs on these isotopes. The density of the scintillator is 0.78 g/cm^3 and the hydrogen to carbon ratio for the KamLAND scintillator is 1.97. Inserting these numbers into Equation 2.20 results in an estimated mean neutron capture time of $205.2 \mu\text{s}$ [Fuj01].

Table 2.1: Isotopes in the KamLAND scintillator and selected properties. For each isotope, the capture cross section for neutrons with velocity $v_0 = 2200 \text{ m/s}$ and the relative fraction of neutron captures are shown.

| <i>Isotope</i> | <i>Capture Cross Section (barns per atom)</i> | <i>Fraction of Neutron Captures</i> |
|-----------------|---|---|
| ^1H | 0.3326 | 99.45% |
| ^2H | 0.000519 | 2×10^{-7} |
| ^{12}C | 0.00353 | 0.55% |
| ^{13}C | 0.00137 | 2×10^{-5} |

The probability of eliminating false events is increased by introducing three cuts on possible neutrino events. Because the thermalization of neutrons can vary, a timing cut is established for the neutron capture. The captures must occur between 10 and 500 microseconds after the prompt signal occurs. The prompt gammas must have a combined energy in the range of $1.0 \leq E \leq 8.0 \text{ MeV}$ and the capture gamma energy must lie in the range between 1.8 and 2.7 MeV. Finally, the events must occur in close proximity to each other.

2.3 Detector Location and Components

The KamLAND detector is located under the peak of Mount Ikenoyama, about 50 kilometers from the city of Toyama on the west coast of Japan (see map - Figure 2.2). It is situated in the same underground cavity at the Kamioka site as the original Kamiokande neutrino experiment and 500 m from the Super-Kamiokande experiment.

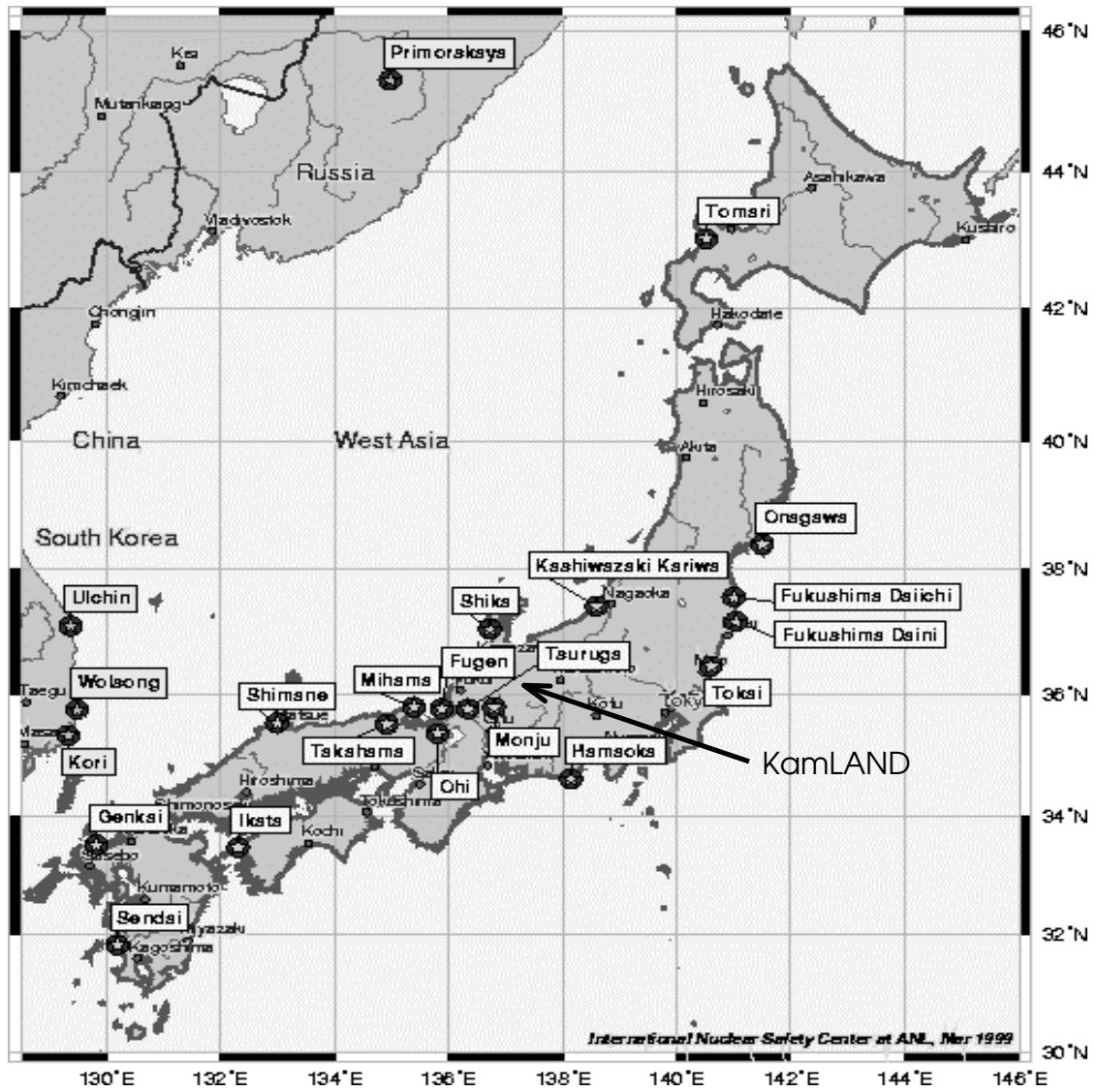


Figure 2.2: Map of Japan and locations relevant to the KamLAND experiment. The locations of the nuclear power reactors used in the experiment are shown in relation to the KamLAND site.

The muon flux at the KamLAND site is compared to other underground experiments in Figure 2.3. KamLAND is buffered by over 1000 meters of rock or about 2700 meters water equivalent, which provides shielding from cosmic rays that have energies less than 1.3 TeV at the mountain surface and provides a well known muon attenuation factor of 10^5 .

The detector is comprised of two sections, called the Inner and the Outer Detectors and is detailed in Figure 2.4. The Inner Detector is comprised of two sections separated by a 13 m diameter spherical balloon made of 135 μm thick transparent nylon/ethylene vinyl alcohol copolymer composite film. Inside the balloon is approximately one kiloton of ultrapure liquid scintillator with a density of 0.78 g/cm^3 . It is comprised of 80% Dodecane and 20% Pseudocumene (1,2,4-Trimethylbenzene) for a hydrogen to carbon ratio of 1.97. In addition, 1.5 g/ ℓ of PPO (2,5-Diphenyloxazole) is added to act as a fluor. Between the balloon and the 18 m stainless steel shell of the Inner Detector is a buffer of dodecane and isoparaffin oils that provide shielding for the liquid scintillator.

The balloon is supported and kept in an approximate spherical shape by minimizing the differences in density between the scintillator and mineral oil and by a series of support ropes. Along the inside surface of the steel sphere in the mineral oil are 1325 seventeen inch and 554 twenty inch photomultiplier tubes (PMTs). These are arranged in a hexagonal lattice array and face in towards the balloon. The scintillator and mineral oil both produce directional Čerenkov signals while the scintillator also produces large isotropic light signals from ionizing radiation.

The Outer Detector functions as both a veto detector and as a passive shield against radioactivity. It is comprised of the rest of the detector cavity surrounding the Inner Detector and is filled with 3.2 kilotons of ultrapure water. The cavity itself is approximately 20 m in diameter in the shape of a right cylinder. Installed on the cavity's surfaces and facing in towards the Inner Detector sphere are 225 twenty inch PMTs salvaged from the Kamiokande experiment. The positioning of the PMTs can be seen in Figures 4.7 and 4.8.

Since the spatial coverage of the Outer Detector PMTs is approximately 3%, a white diffusing material called Tyvek is used to increase the amount of light detected and

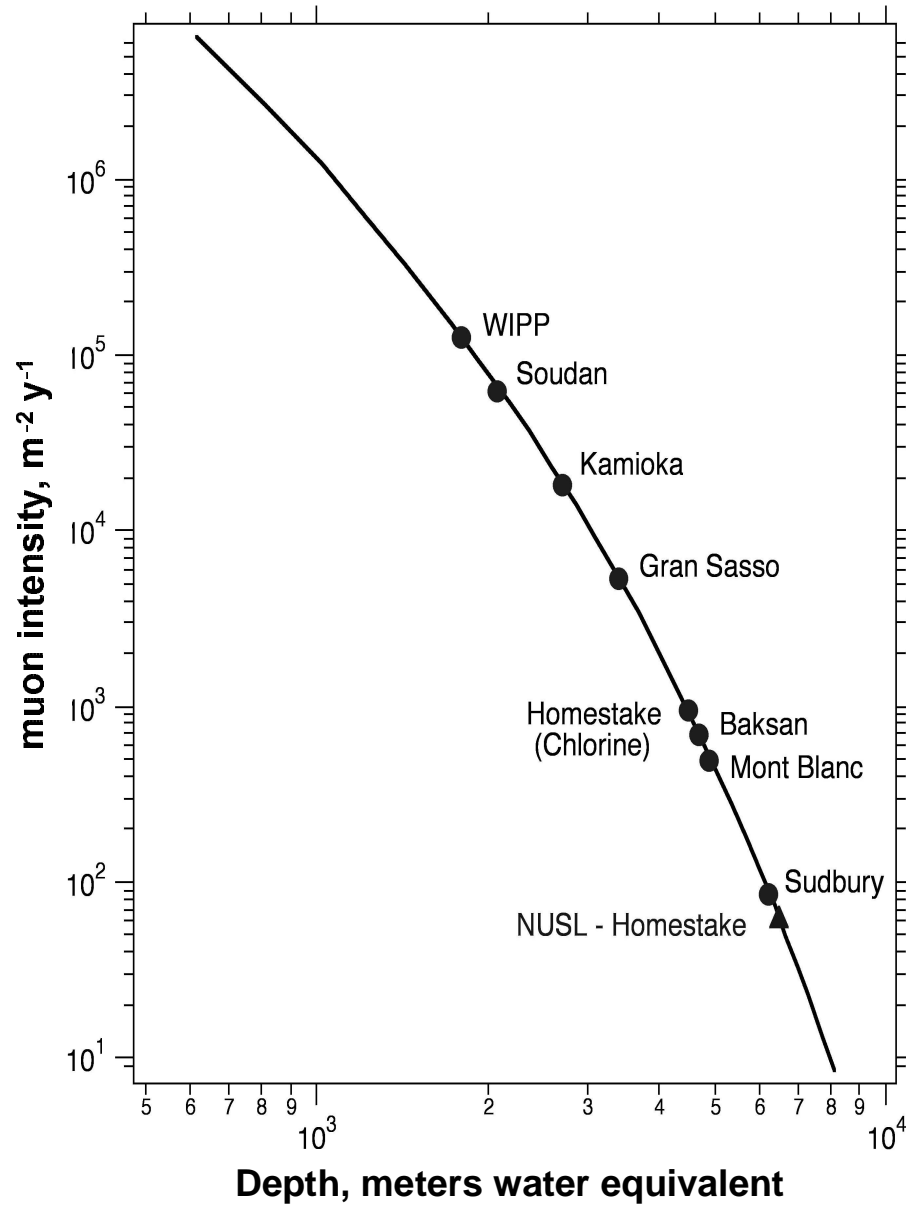


Figure 2.3: Muon flux at various depths for different experiments. Current experimental sites are denoted by a \bullet while proposed sites are denoted by a \blacktriangle . KamLAND, located at the Kamioka site, has a meters water equivalent depth of 2700 meters.

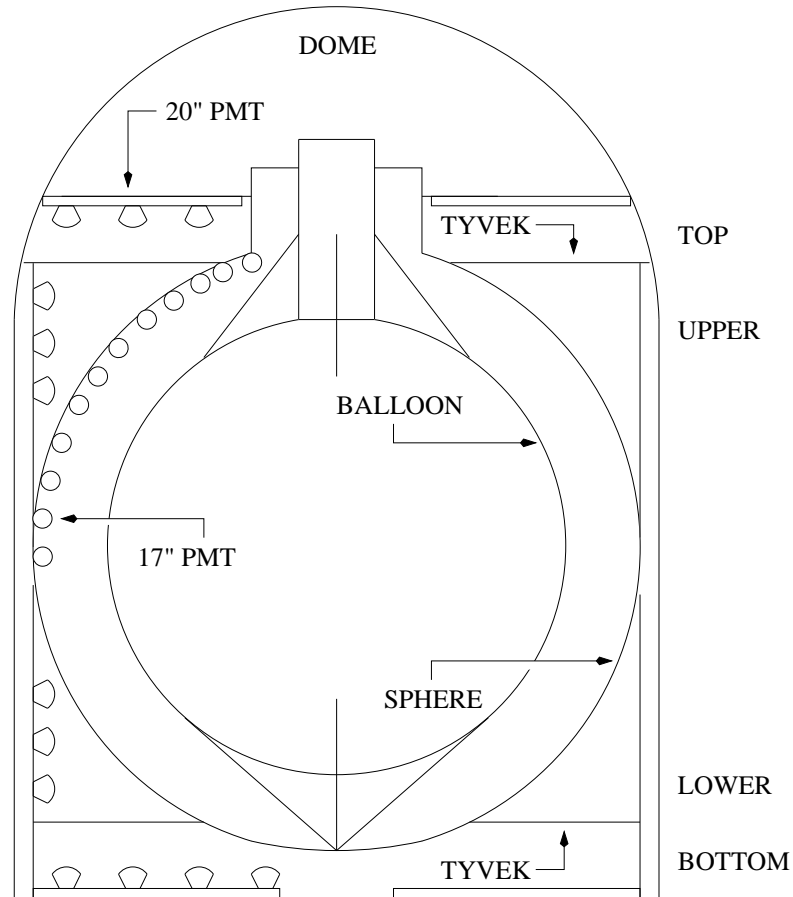


Figure 2.4: Cutaway view of the KamLAND detector showing the components of the Inner and Outer Detectors. The radius of the Inner Detector sphere is 9 m, with a balloon radius of 6.5 m. The dimensions of the cylindrical Outer Detector are a height of 20 m and a radius of 9.7 m. A dome of height 7.5 m is available above the detector for electronics and instrumentation.

to eliminate dead zones. The Tyvek is placed behind the PMTs on the cavity's surface as well as on the Inner Detector sphere.

In addition, the Tyvek is used to optically segment the Outer Detector into three distinct regions, referred to as the top, bottom, and side regions. The side region is also considered to be divided into two sections (the upper and lower) by the proximity of the Inner Detector sphere's equator to the cavity wall. The segmentation of the Outer Detector in this way allows the muons to be tracked as they travel through the detector cavity.

Chapter 3

The Outer Detector

The success of large underground detectors like KamLAND heavily depends on the ability to understand and suppress background. KamLAND's background comes from natural radioactivity and cosmic ray muon-induced processes and the Outer Detector plays an important role in discriminating this background from true events. It actively tags and vetoes through-going cosmic ray muons in offline analysis by detecting their Čerenkov radiation. It also acts as a passive shield by absorbing natural radiation and by moderating and absorbing spallation neutrons, which are produced when muons collide with nuclei in both the rock and the water.

3.1 Čerenkov Radiation

Čerenkov radiation arises from the interaction of a charged particle traveling through a transparent medium, which in the KamLAND Outer Detector is a cosmic ray muon traveling through water. The electric field of the muon causes the nearby water molecules to behave like elementary dipoles by forcing the hydrogen atoms to rotate around the oxygen atom, such that they are further away (closer) to the negatively (positively) charged muon as seen in Figure 3.1. This causes the medium to become polarized about the point P .

As the muon continues along its track, the shape of the atoms around P returns to normal. Thus, each incremental region along the muon track will receive a very brief electromagnetic pulse in turn as the muon traverses the water. If the muon has a low velocity, the polarization field around the muon is symmetric in all directions. With such symmetry, there is zero resultant field at large distances and therefore, no radiation.

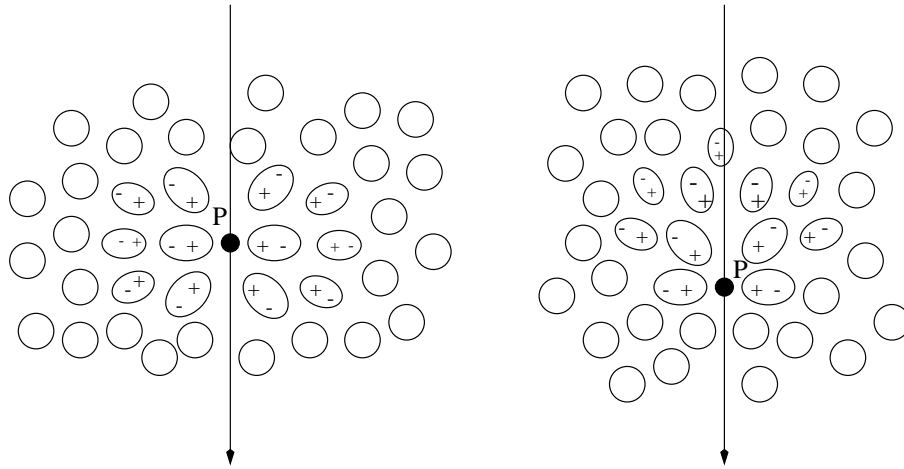


Figure 3.1: The polarization of a dielectric that is set up when a charged particle passes nearby. The figure on the left is for a negatively charged particle traveling with a low velocity, while the figure on the right is for a high velocity particle.

If the muon is moving at a speed that is faster than that of light in the medium, then the picture is different. In this case, the polarization field loses its symmetry along the axis, resulting in a dipole field that is apparent at large distances from the muon track. This dipole field is momentarily set up by the muon in turn in each incremental region. Each region then radiates an electromagnetic wavelet of light over a band of frequencies.

In most directions, these radiated wavelets from all along the track interfere destructively, so that the resultant field intensity is zero at some distant point. But when the velocity of the particle is greater than the speed of light in the medium, it is possible for the wavelets to be in phase with each other in one particular direction. This produces a resultant field at a distant point. From Figure 3.2, it can be seen that when the wavelets from different points along the muon track are in phase, a coherent plane wavefront is formed at

an angle, θ , with respect to the muon track. Although Figure 3.2 has been drawn in two dimensions, the Čerenkov radiation is produced in complete symmetry about the axis of travel and propagates along the surface of a cone with the angle θ .

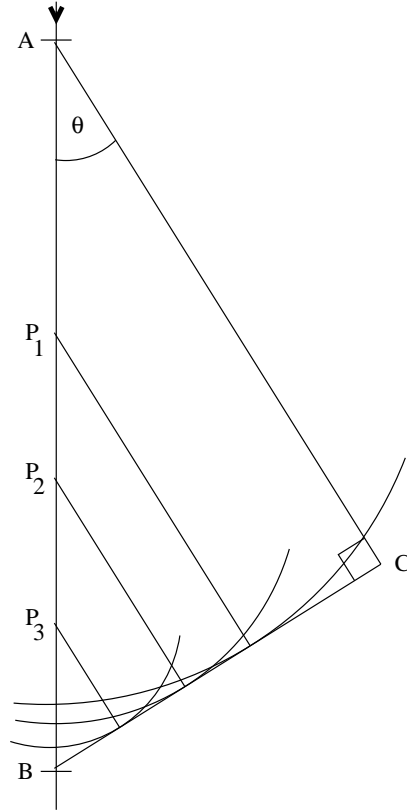


Figure 3.2: The coherence of the radiated wavelets from arbitrary points, such as P_1 , P_2 , and P_3 , produce a unified wavefront along BC at a specific angle, θ . This angle depends upon the medium through which the charged particle is traveling.

This angle can be geometrically described by noting that the particle travels from point A to B in the same time that the light travels from A to C . The relativistic velocity of the particle is given by β , which is the speed of the particle expressed as a factor of c , and the time it takes for the particle and light to travel to points B and C from A , denoted by $\Delta\tau$. Thus, the distance traveled by the particle and the light is $AB = \beta c \Delta\tau$ and $AC = \Delta\tau(c/n)$ respectively, where n is the index of refraction of the medium. Therefore, the angle θ is

given by

$$\cos \theta = \frac{1}{n\beta}. \quad (3.1)$$

From this equation, it can be seen that for a particle whose relativistic velocity approaches c , the maximum angle of emission is given by $\theta_{max} = \cos^{-1}(1/n)$. The radiation that is produced has wavelengths mainly in the visible and near-visible regions of the spectrum, as long as $n > 1$. Since the medium of the Outer Detector is water, this results in $\theta_{max} = 41.2^\circ$ with a wavelength in the blue region.

There are three more conditions that must be met in order to achieve coherence. The velocity of the particle must be above a minimum, set by $\beta_{min} = (1/n)$, in order to produce radiation. In order to avoid diffraction, the path length of the particle through the medium must be large compared to the wavelength of the emitted radiation. Finally, the velocity of the particle through the medium must remain constant [Jel58].

3.2 Neutron Spallation

Spallation is a two stage process on the nuclear level. In the first stage, the incident particle collides with nucleons inside the nucleus, which causes a series of intranuclear cascades. The end result is the ejection of various types of nucleons from the nucleus, which is now left in an excited state. As the imparted energy from the original collision is distributed over the nucleus, low energy particles evaporate from the surface as part of the second stage. Finally, the remaining excitation energy is dissipated by the emission of gamma rays.

The high energy neutrons are those that leave the nucleus during the cascade stage while the lower energy neutrons are from the evaporation stage. Due to their low energy, the evaporated neutrons are easily moderated and absorbed by the water of the Outer Detector. However, the cascade neutrons are highly penetrating and thus, difficult to shield [Bau95].

The energy spectrum of neutrons obtained from spallation processes is not well known. Figure 3.3 shows experimental models derived from the Large Volume Detector

(LVD) at Gran Sasso [Agl99] and from various proton decay experiments [Kha83]. In addition, a Monte Carlo simulation [Wan01] is also shown.

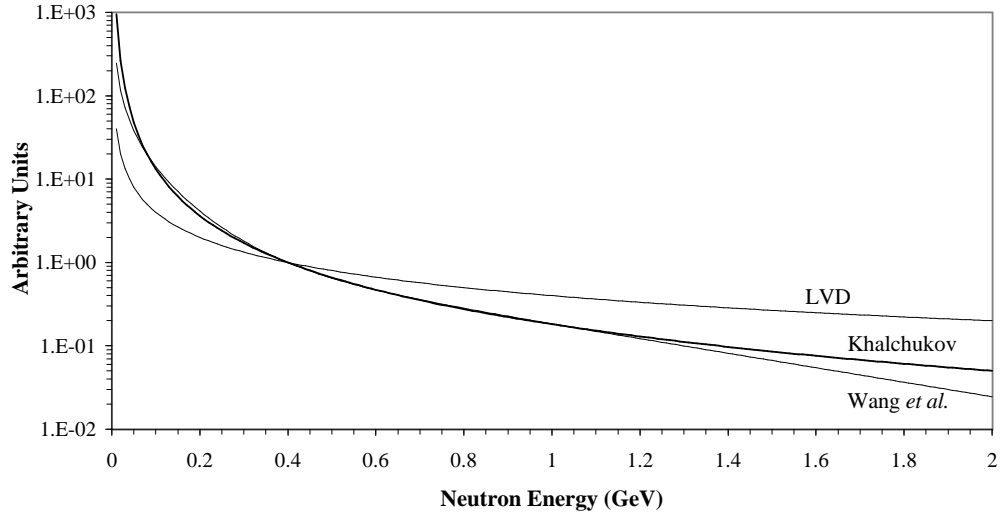


Figure 3.3: A comparison of two experimentally derived models (Large Volume Detector at Gran Sasso (LVD) [Agl99] and various proton decay experiments [Kha83]) and a Monte Carlo derived spectrum (Wang et al. [Wan01]) for spallation neutrons. Each model is normalized to unity at 400 MeV.

3.3 Relevance to KamLAND

The Outer Detector detects and tags through-going cosmic ray muons by their tell-tale Čerenkov radiation. For those muons that also pass through the Inner Detector, the Outer Detector acts as an anti-coincidence veto, thereby removing the muons from consideration.

The volume and makeup of the Outer Detector allows for passive radiation shielding from the several sources of low energy particles. Trace amounts of uranium and thorium are naturally found in the rock surrounding KamLAND and in the materials used in the construction of the detector, and emit low energy particles from radioactive decay and spontaneous fission [Cha02]. In addition, muons moving through the water ionize nearby

particles. The ionized particles are immediately slowed and neutralized and the low energy neutrons are absorbed by the water. Due to the very short distances needed to attenuate these types of particles in the Outer Detector, this background is negligible.

However, the high energy neutrons produced by spallation are the dominant source of background, one that can have a major effect on the results of KamLAND. If such a neutron scatters off protons in the Inner Detector, the proton recoils could mimic a positron signal. If the neutron is then captured by another proton and the three data cuts for a neutrino event are satisfied, a fake neutrino event will be recorded. Figure 3.4 shows the Feynman diagrams for real and fake events.

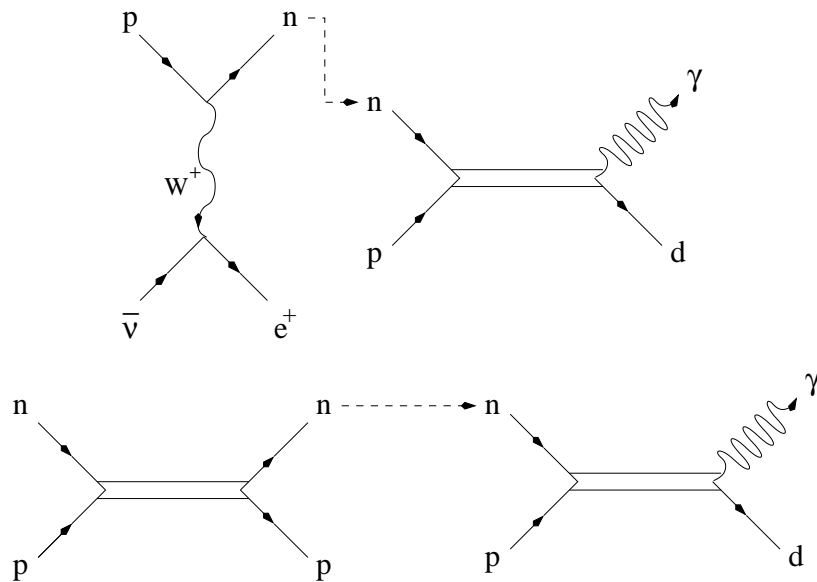


Figure 3.4: Feynman diagrams of real and fake events. The top figure shows the process for a real neutrino event: the inverse beta decay of a proton followed by the neutron capture. The bottom figure represents the fake event which is characterized by the proton-neutron scattering process, which can occur several times, followed by the neutron capture. Time increases from left to right.

Muon produced neutrons can be discriminated from the real neutrino signals, but only if the muon is recognized by the detector [Hag00]. Therefore, muons that enter the detector must be tagged and subsequent events produced by them eliminated by virtue of

spatial and time cuts around the muon path. For this reason, the muon detection efficiency by the Outer Detector must be as high as possible to identify and eliminate neutrons produced by through-going muons.

With the veto conditions on tagged muons, the remaining background source comes from spallation neutrons produced by muons that never enter the KamLAND Detector but interact with nuclei in the surrounding annulus of rock. Computer simulations, which are discussed in Chapter 7, are able to provide an estimate of the expected background from these events.

Chapter 4

Photomultiplier Tube Testing

At the conclusion of the Kamiokande neutrino experiment in 1995 and prior to the formation of the KamLAND collaboration, approximately 1000 twenty inch PMTs were removed from the experiment site and placed into a nearby storage facility at the Kamioka mine site. During the summer of 1999, a simple testing facility was set up at the storage site to determine the state of these PMTs. They were connected to 1500 volts and the dark noise signal was observed. PMTs denoted ‘good’ had dark pulses less than 10 mV. Good PMTs also had a dark current of approximately 0.55 mA. Dead PMTs were observed to have dark currents of 10 mA or greater. This preliminary testing produced 842 PMTs that were considered good and they were shipped to Sendai, Japan for further testing. An additional 50 untested PMTs were already located in Sendai, giving a total of 892 from which to select the Outer Detector PMTs.

The PMTs were comprised of four different types, with each successive model representing an improvement in design. Three types were used in the Kamiokande experiment, labeled ‘A’, ‘B’, and ‘C’. The first two types were developed specifically for that experiment while the ‘C’ type PMTs, which were developed for the upcoming Super-K experiment, were used towards the end of the Kamiokande experiment. The fourth type, denoted ‘SK’, was used only for testing purposes during the design phase of Super-K.

The main difference between the four types is that the ‘A’ and ‘B’ type PMTs have a 13 stage dynode assembly while types ‘C’ and ‘SK’ have an 11 stage dynode assembly. Types ‘C’ and ‘SK’ also show a clear single photoelectron peak response and have an improved timing response. However, since muon events typically produce more than one photoelectron per PMT and because of the presence of Tyvek in the Outer Detector, these differences in PMT technology do not affect the ability of the Outer Detector to act as a veto for the Inner Detector.

4.1 Test Bench Setup

Due to coverage requirements for the Inner Detector, 600 PMTs (mostly ‘B’ types with some ‘A’ types) were taken from the stock for use in the Inner Detector. In order to supply the best PMTs for the Outer Detector, a thorough analysis of the remaining 290 PMTs (containing all four types) was performed to determine their worthiness for installation. This analysis consisted of first verifying the integrity of a PMT by examining it for evidence of broken components and a loss of vacuum. If it was intact and the resistance in the signal and high voltage cables measured $50\ \Omega$ and greater than $5\ \text{M}\Omega$ respectively, it was deemed fit for use.

The tests at the Honda-seiki warehouse facility in Sendai were carried out during December 1999 and June 2000. The test bench setup used was put together for the tests of the Inner Detector PMTs. It consists of six light-tight and magnetically shielded bins which allow testing of six PMTs simultaneously. A nitrogen dye laser with adjustable attenuation filters was used to illuminate the PMTs via fiber optic cables. Three 8” PMTs, labeled Monitor 1, Monitor 2, and Laser, were used to monitor the laser output. All of these signals were then sent to an electronics system that contained attenuation units, amplifiers, and an ADC, as seen in Figure 4.1. Finally, the signals were sent to a PC based multichannel analyzer for data acquisition and analysis.

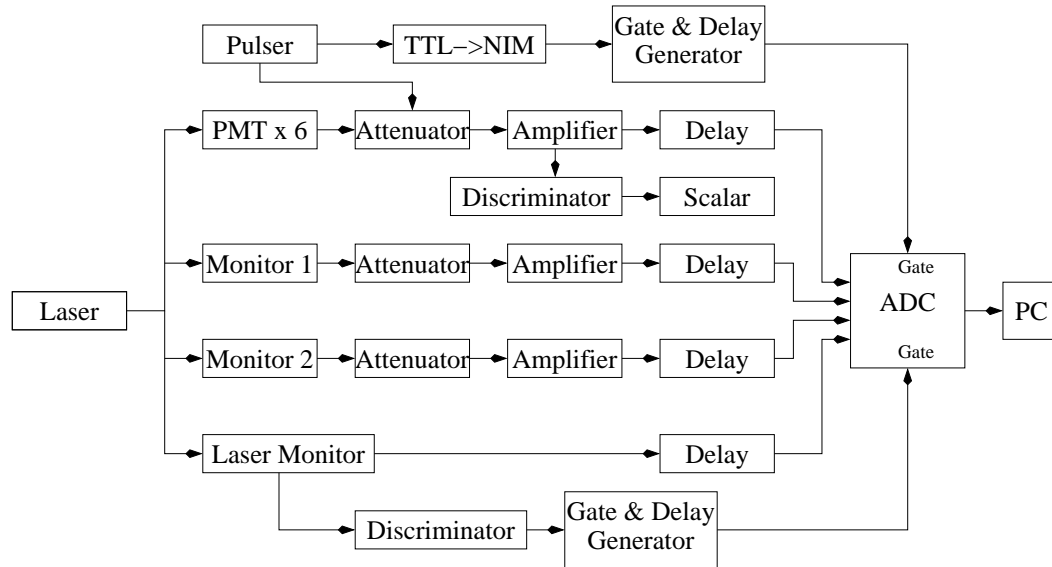


Figure 4.1: Block diagram of electronics for high voltage testing. The pulser is used for the charge/channel calibration while the laser is used for the high voltage testing.

Voltage testing at Sendai started by placing a PMT into one of the six light-tight bins. Hamamatsu has specified the voltage to achieve a gain of 0.6×10^7 for each PMT. Every PMT was tested in 100 V increments from 100 V below to 400 V above this nominal value. An attenuation level of 40 dB on the anode signal was used for measurements at the four lowest voltages and then raised to 52 dB for the last two measurements in order to keep the signal from going offscale on the multichannel analyzer. Because the PMT response to the laser illumination is much larger than any background, it was possible to begin this test within 15 minutes of placing voltage on the PMT. After all six high voltage measurements had been performed (lasting about one hour), a dark current test at the nominal voltage could then proceed, since most background noise had died down. For this test, the laser was turned off and the attenuators were set at 0 dB. The number of pulses counted in ten seconds was used to obtain a noise rate. A PMT was determined to be noisy and rejected if the dark current noise rate was greater than 50 kHz.

Physics Analysis Workshop (PAW) [App95] was used to plot the histograms for the tested PMTs and to obtain Gaussian fits to the peaks. These peak values were recorded on paper and the histogram data were saved to file. When the testing of six PMTs was finished, all associated files are deemed a ‘Set’ and were stored for later analysis.

Figure 4.2 shows a typical laser response spectrum for a PMT (Serial #0245, a type ‘C’ PMT). The channel number of the peak is derived from fitting procedures using PAW for all six PMTs under test and for the three monitor peaks. The program fits the peaks to a Gaussian shape using a range of channel numbers determined by the width at 40% of the height.

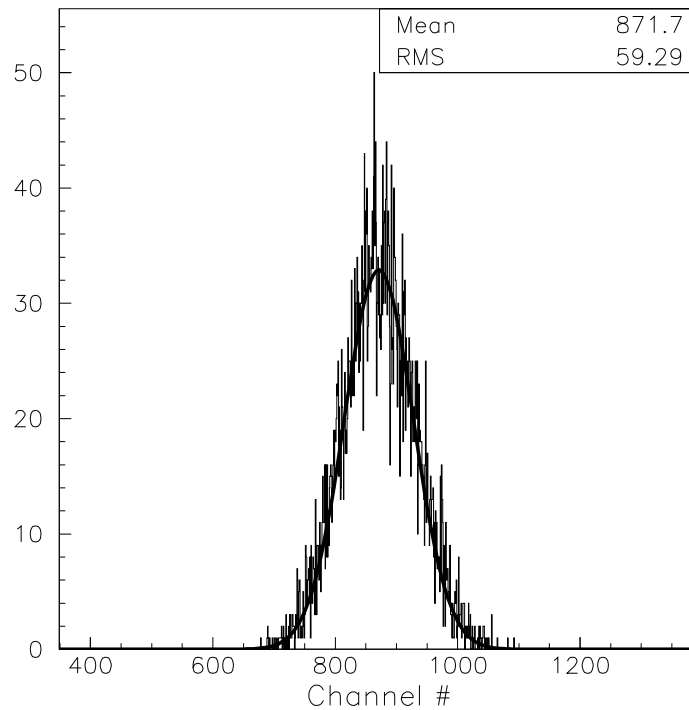


Figure 4.2: Fitted histogram for PMT #0245. Laser response spectrum for type ‘C’ PMT, serial #0245, during Set 25, measurement 1. The channel number of the peak, C_p , is derived from Gaussian fitting procedures using PAW.

4.2 Gain and Gain Response Function for Photomultipliers

For an n -stage photomultiplier, the response function of the gain, G , with respect to the high voltage, V , is given by

$$G = \delta^n = \kappa V^\alpha \quad (4.1)$$

where δ is the average secondary electron emission ratio and κ and α are empirically determined constants. The constant α is given by

$$\alpha = n\alpha_o \quad (4.2)$$

where α_o is a coefficient determined by the dynode material and geometric structure [Ham00]. This form of the response is valid in the operating region of the PMT.

The gain for a PMT at a specific voltage can be calculated by

$$G = \frac{Q_p}{eN} \quad (4.3)$$

where Q_p is the amount of charge collected by the PMTs in Coulombs, e is the charge per photoelectron ($1.6 \times 10^{-19} \text{ C}/e^-$), and N is the number of photoelectrons produced by the photocathode in response to the incident laser photons. The intensity of the laser signal can be reduced until only a single photoelectron is being produced ($N = 1$).

The charge, Q_p , is given by

$$Q_p = \frac{C_p - C_o}{m} \quad (4.4)$$

where C_p is the channel number of the laser pulse peak, C_o is the constant channel offset due to the electronics DC level, and m is the conversion factor from channel number to charge. C_p values are measured for several voltages, spanning a range of 500 V for each PMT, according to the voltage testing procedure.

Values of C_o and m are determined by a calibration process whereby square wave pulses of known amplitude and width were injected into the ADC circuitry (See Figure 4.1).

By measuring the voltage height, V , and the time width, t , of the pulse and knowing the impedance, Z (50Ω), of the circuitry, the value of the input charge was obtained from

$$Q = \frac{Vt}{Z} \quad (4.5)$$

Typical numbers were $V = 860$ mV and $t = 40$ ns. This calibration was performed with several different voltages at the three attenuations (0, 40, and 52 dB) for all six bins' electronics.

A fitted calibration plot is shown in Figure 4.3. A linear fit program [Fas88] was used to calculate the conversion factor, m (pC/ch), and the offset, C_o (ch). Using these data, all the peaks from the voltage test were converted to an amount of charge.

The position test was used to determine whether the angle of incidence of the laser affects the number of photons seen by the PMT. One PMT of each type (A - serial #4014, B - #0022, C - #0265) was placed in a bin in a normal manner and a peak channel measurement taken. On subsequent runs, the PMT was tilted at an angle, Θ , rotated an angle, Φ , or a combination of these, as seen in Table 4.1.

Table 4.1: Position of a PMT during position testing

| <i>Run #</i> | Θ | Φ |
|--------------|----------|--------|
| 1 | 0 | 0 |
| 2 | 0 | 90 |
| 3 | 20 | 90 |
| 4 | 20 | 180 |

Figure 4.4 show the gains for these tests. Within systematic uncertainties, all values were the same, with the conclusion that each PMT saw the same number of photons from the laser independent of the orientation and placement of the phototube.

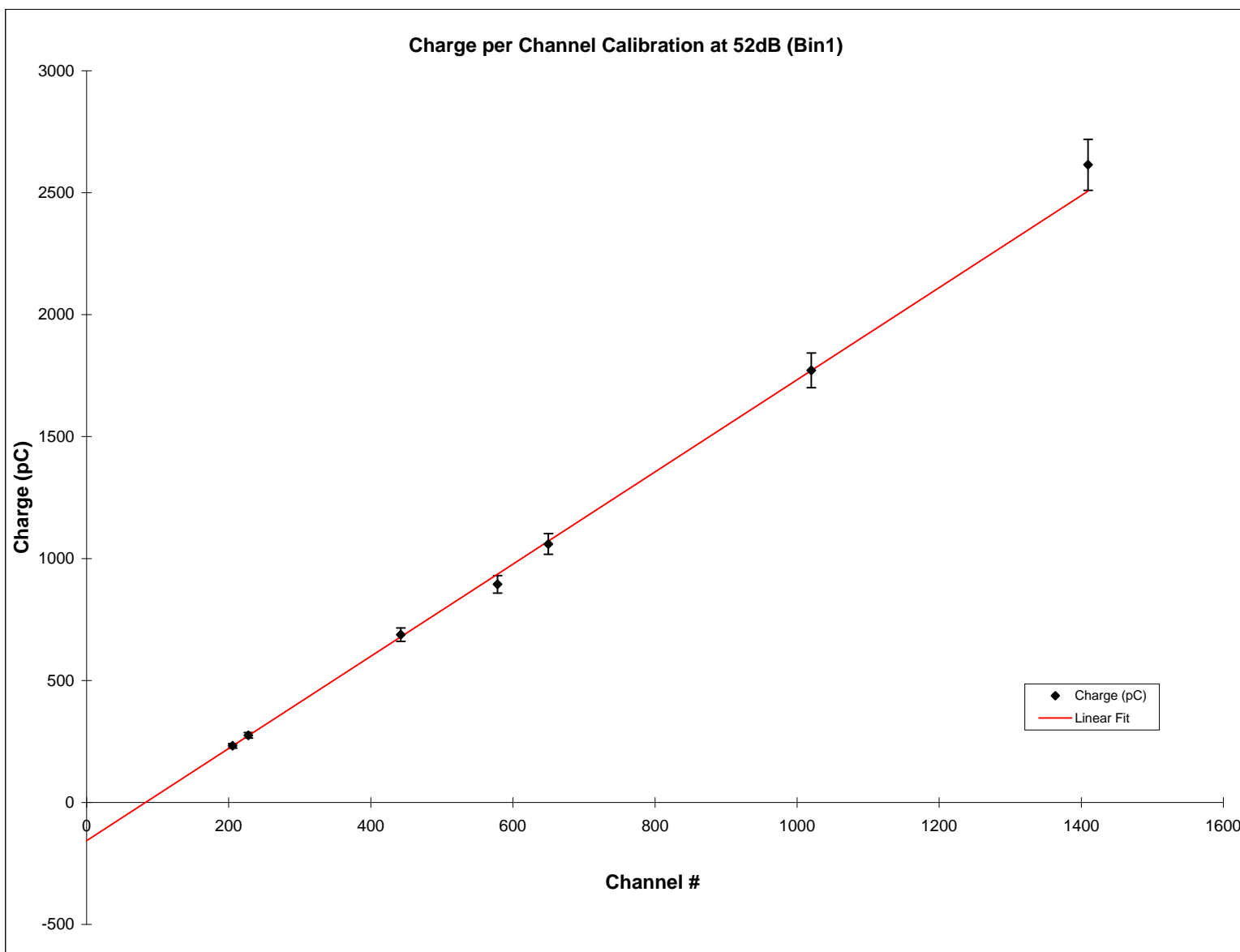


Figure 4.3: Charge per channel calibration for Bin 1 at 52 dB. Varying amounts of charge Q were input into the ADC circuitry. The data were fit to a straight line to yield the slope m (pC/ch) and the channel offset C_o for each bin at each attenuation. With this information, the peaks from the voltage test were converted into the amount of charge, Q_p . The error in the amount of input charge was assumed to be 5%. In this way, the channel number is converted to a corresponding charge produced by the PMT.

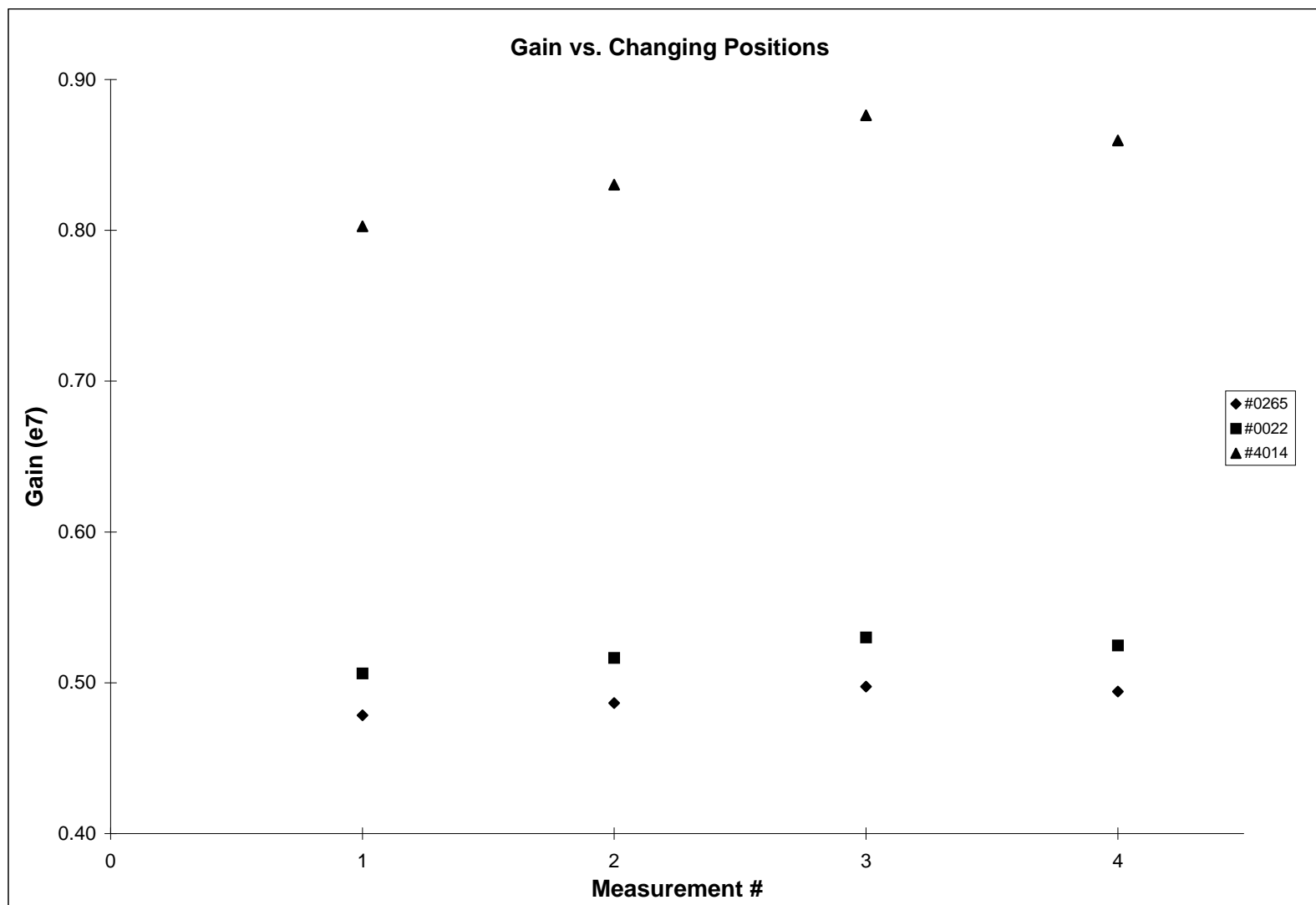


Figure 4.4: Gain values for different positions of three tested PMTs. Gain values for four different positions are shown. Within systematic uncertainties, the values for each PMT tested positions are the same. The result is the conclusion that the number of photons from the laser are independent of the orientation and placement of the PMTs. Serial #0265 is a type ‘C’ PMT, Serial #0022 is a type ‘B’ PMT, and Serial #4014 is a type ‘A’ PMT.

4.3 Analysis of the Single Photoelectron Peaks

For the purpose of the gain calculation in Equation 4.3, the number of converted photoelectrons, N , induced by the laser illumination must be known. Ideally, this value is determined by a comparison with the single photoelectron (SPE) peak. However, of the four types of PMTs used for the Outer Detector, only the ‘C’ and ‘SK’ types are capable of seeing a single photoelectron peak. The 17” Inner Detector PMTs can also detect the SPE peak. A 20” ‘C’ PMT serial #0245 at 2108 V and a 17” PMT serial #0021 at 2262 V were used to determine the responses. SPE spectra for the type ‘C’ and the 17” PMTs are shown in Figure 4.5.

The Inner Detector electronics setup used the laser pulse to gate the ADC. As a result, the noise spectrum cannot be readily obtained by turning off the laser. Instead, different combinations of laser filters were used to reduce the intensity until the number of photoelectrons produced by the photocathode decreased to one. This was verified when the channel number of the SPE peak stopped decreasing (meaning that the minimum amount of charge had been collected) and the number of counts in the peak for a given collection time started decreasing (indicating that not every laser pulse was producing a photoelectron).

The location of the SPE peak was converted into an equivalent amount of charge using the results of the charge/channel calibration. Equation 4.4 yielded the result of 0.88 ± 0.08 pC for PMT #0245 and 1.37 ± 0.07 pC for PMT #0021. It is necessary to compare these results with the voltage testing data obtained for these PMTs so that the number of photoelectrons, N , induced by the laser illumination during the voltage test is known. These two PMTs were tested together in Set 25, with measurement 1 (Set25m1) having the same voltage as in the SPE test. Using the equation,

$$\frac{1}{N} = \frac{Q(\text{SPE})}{Q(\text{Laser})} \quad (4.6)$$

where N represents the number of photoelectrons associated with the laser illumination, PMT #0245 sees $N = 402 \pm 39$ while PMT #0021 sees $N = 367 \pm 21$. The weighted average [Bev92] of these two values is $N = 375 \pm 18$ photoelectrons. Here, it is assumed that the

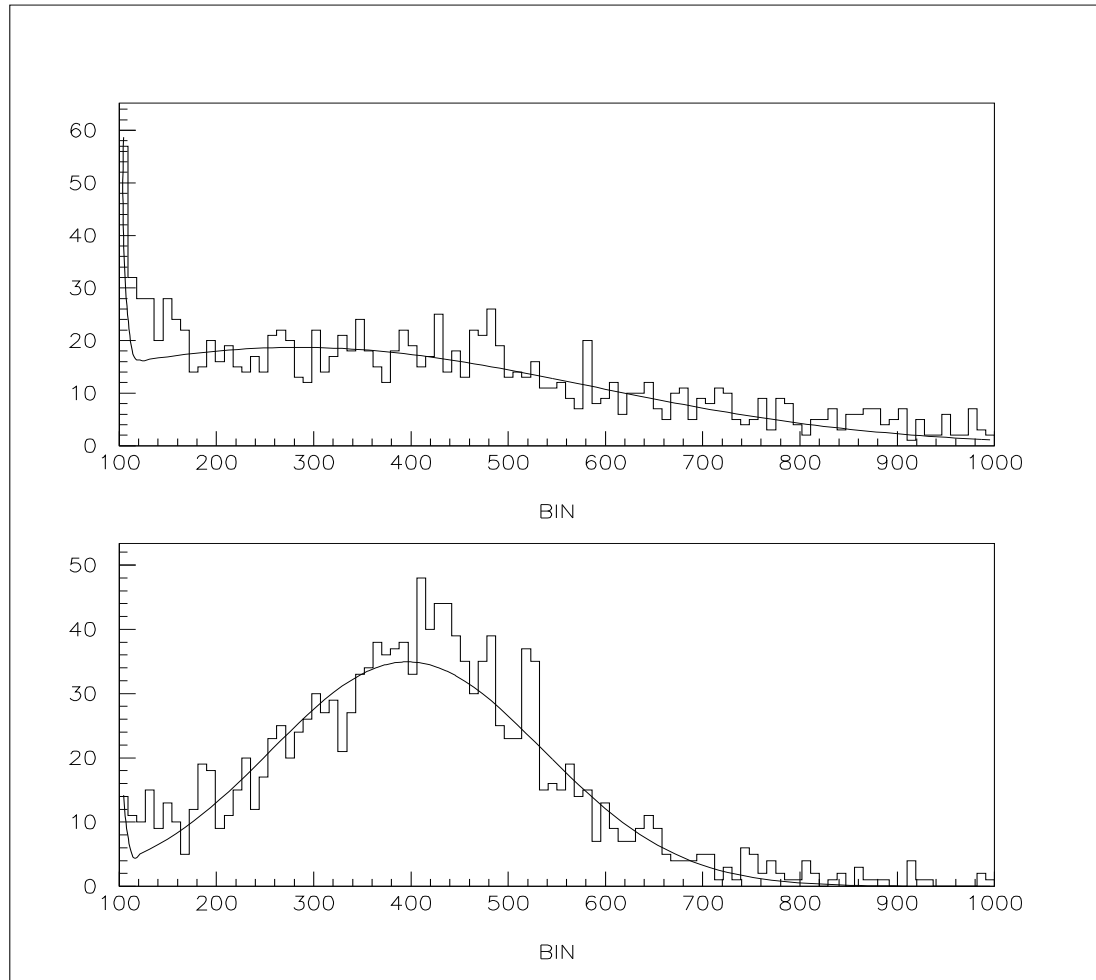


Figure 4.5: SPE spectrums for PMTs #0245 and #0021. The upper spectrum shows the SPE peak for the type ‘C’ Outer Detector PMT (Serial #0245). The peak for this type ‘C’ PMT is evident, but still difficult to determine precisely. The centroid is located in channel 284. The lower spectrum shows the SPE peak for the 17” Inner Detector PMT (Serial #0021). This peak is clean and easy to fit and is centered on channel 396.

laser illuminates both tested PMTs equally and that the photocathode responses are the same.

Since the noise in the type ‘A’ and ‘B’ PMTs is too high to show a single photoelectron response, they cannot be calibrated in the same way. Instead, it must be assumed that the photocathode responses of all PMTs are the same and that this same laser illumination would have yielded an average of $N = 375$ in all of the PMTs. In practice, the amount of laser illumination does change over time and affects the actual number of photoelectrons detected. This was taken into account by normalizing to the monitor:

$$N = \frac{375}{\rho} \quad (4.7)$$

where ρ is defined by

$$\rho = \frac{\text{monitor value of Set25m1}}{\text{monitor value of data point}} \quad (4.8)$$

In this way, the differences in illumination for each measurement set were accounted for.

4.4 Photomultiplier Tube Testing Results

Using Equations 4.3, 4.4, and 4.7, the gain of a PMT can be calculated for a particular high voltage. A typical set of results is shown in Figure 4.6. The data were fitted to Equation 4.1 and values of κ and α were determined for each PMT. Typical numbers are 10^{-20} to 10^{-25} and 7.5 to 10.4 respectively. Using Equation 4.2, the data was compared to the expected value for α_o . For 13 dynode stage systems (types ‘A’ and ‘B’), the average value of $\alpha_o = 0.71$. For the 11 dynode stage systems (types ‘C’ and ‘SK’), the average value of $\alpha_o = 0.75$. These results are in agreement with the Hamamatsu predicted range of $0.7 < \alpha_o < 0.8$ [Ham00].

The voltage required for a specific gain was calculated by

$$V = \left(\frac{G}{\kappa} \right)^{\frac{1}{\alpha}} \quad (4.9)$$

The final table of results (Appendix A) lists for each PMT the serial number, the PMT type, the values of the parameters κ and α , the voltage necessary for $G = 1.0 \times 10^7$, and the

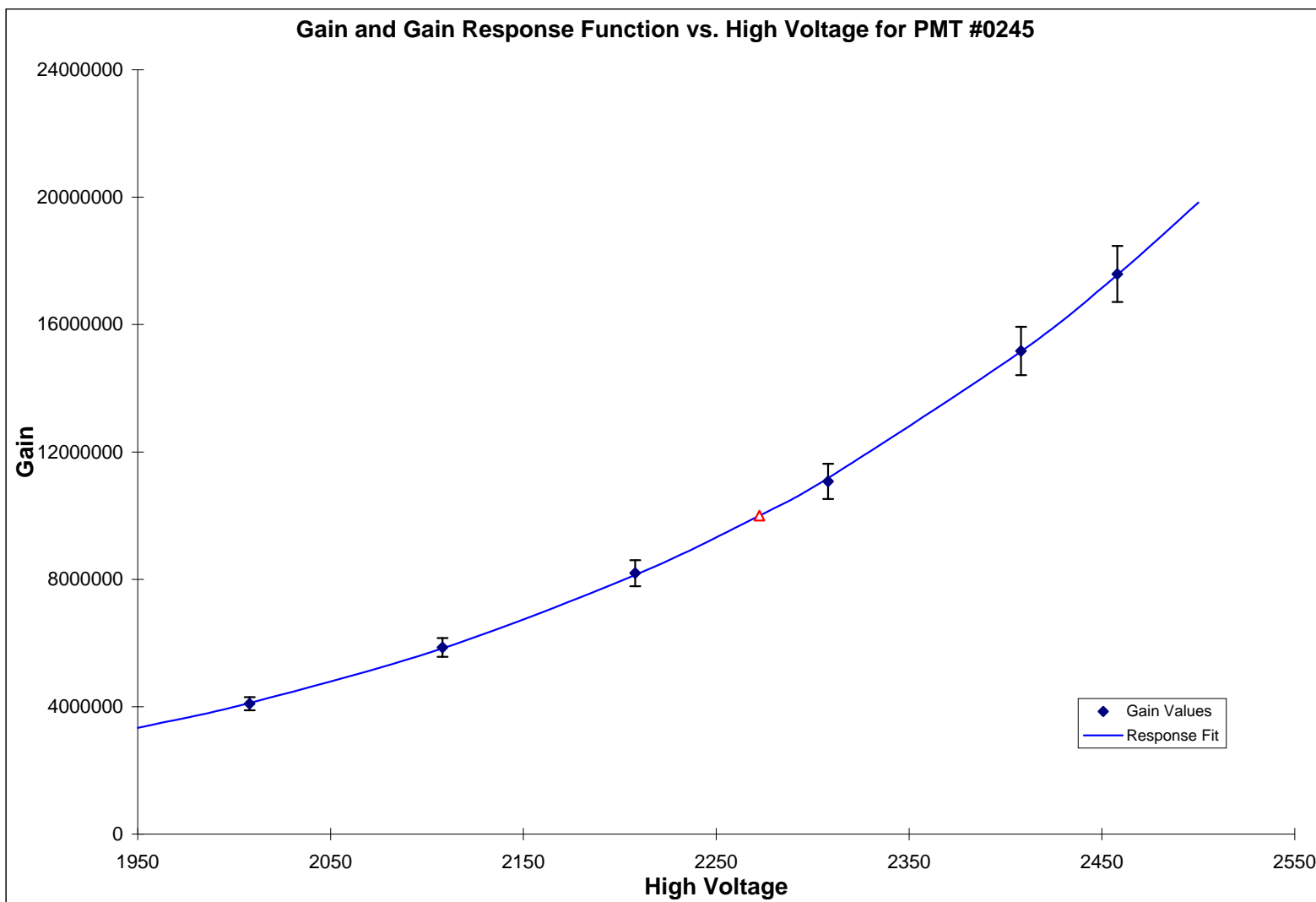


Figure 4.6: Gain versus high voltage plot for PMT #0245 with fit. The gains for six measured voltages are plotted versus voltage, where the gains have an error of 3.8%. These points are then fitted to Equation 4.1. For type ‘C’ PMT (Serial #0245), $\kappa = 4 \times 10^{-23}$ and $\alpha = 9.3$. The \triangle marker represents the point calculated for $G = 1 \times 10^7$ (2250 V).

change in high voltage required for a $\pm 5\%$ change in the gain, the Hamamatsu voltage value for $G = 0.6 \times 10^7$, and the PMT dark current rate. In addition, other relevant information is presented in Appendix B: PMT location, PMT voltage cable labels, and PMT signal cable labels.

The location code for a PMT is of the form R - A - XXX . The first symbol, R , represents the region where the PMT has been installed. The top region is denoted by ‘T’, the side region by ‘S’, and the bottom region by ‘B’. The second symbol, A , labels the PMT row within the region. For both the top and bottom regions, the rows are numbered sequentially starting with the outermost ring of PMTs and proceeding inwards. For the side region, the rows are numbered starting at the top and increasing towards the bottom. The final set of symbols, XXX represents the angle, Φ , of placement. A PMT with tag T -1-207 is located in the top region, in the outermost row, at $\Phi = 207^\circ$. A schematic of the PMT locations can be seen in Figures 4.7 and 4.8.

Figure 4.9 shows the difference in high voltage values between the measured values and those of Hamamatsu for $G = 0.6 \times 10^7$. In general, the tested values were slightly higher, typically of order 20 - 50 volts. This is most likely due to the expected deterioration of the dynodes over time. Large ΔV were taken as evidence of a potential problem and the PMTs were accordingly flagged.

Seventeen PMTs were tested in June, of which six were also tested in December. Based on the results of the doubly tested PMTs, it appears that temperature effects on the laser and electronics had increased the gain values of June tested PMTs. Therefore, the December data was used for the six double tested PMTs. For the remaining PMTs, the difference in voltage at $G = 0.6 \times 10^7$ was normalized to the December test data. Removing the outliers from the previous figure, the adjusted difference in high voltage between the tested values and those of Hamamatsu is shown in Figure 4.10. The average difference in voltage between the December and June values for $G = 0.6 \times 10^7$ was 136 V. Therefore, for the June tested PMTs, it is suggested that the listed voltage required for $G = 1.0 \times 10^7$ be lowered at least 136 V.

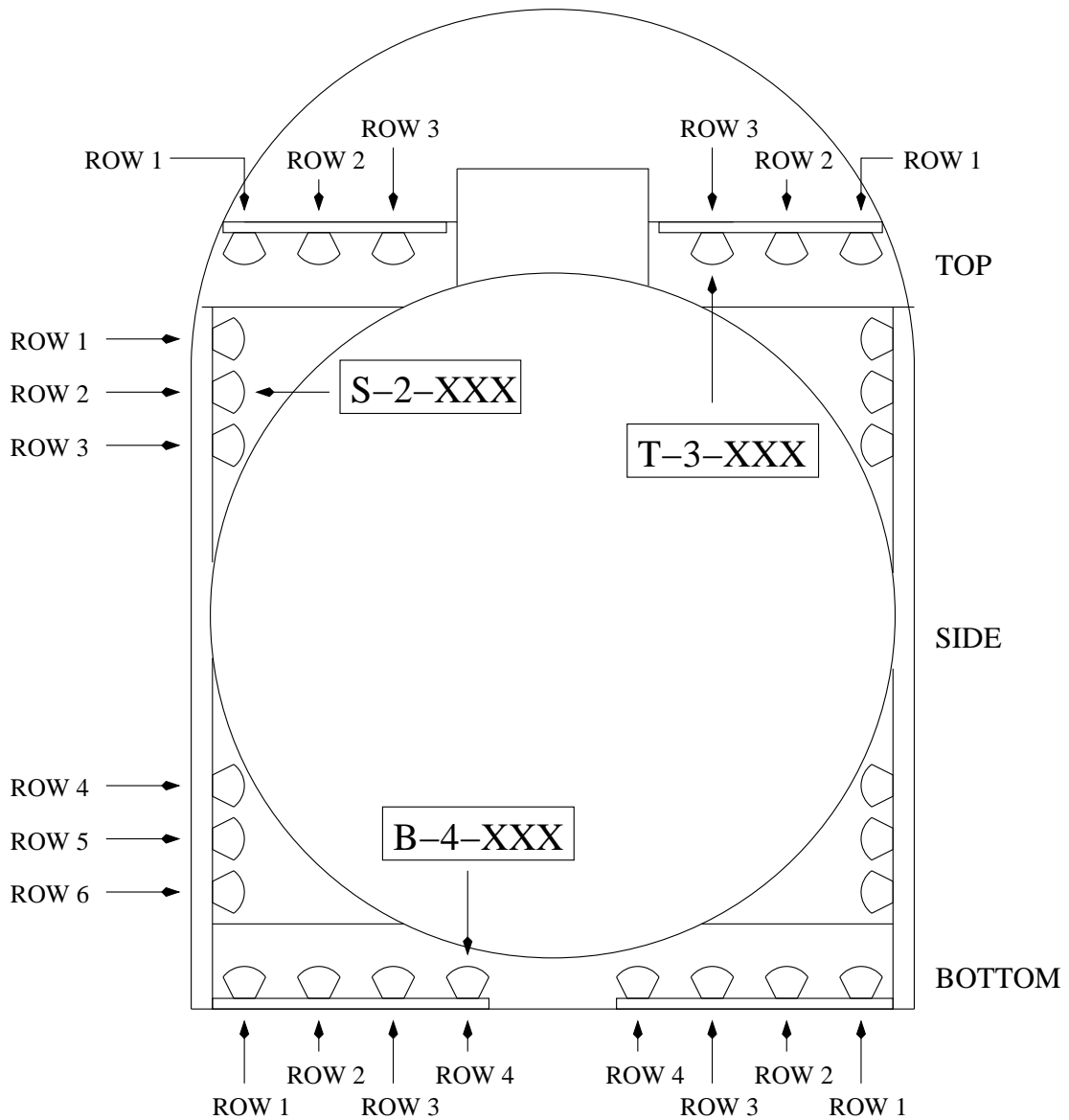


Figure 4.7: PMT location guide 1. A cutaway view of KamLAND shows the locations of the Outer Detector PMTs. The detector is divided into three regions, denoted T (Top), S (Side), and B (Bottom) with each section divided into several rows of PMTs. Each PMT is located with a marker that describes the region, the row, and the angle of placement (Figure 4.8). Thus, tag $T-1-207$ is located in the top region, in the outermost row, at $\Phi = 207^\circ$.

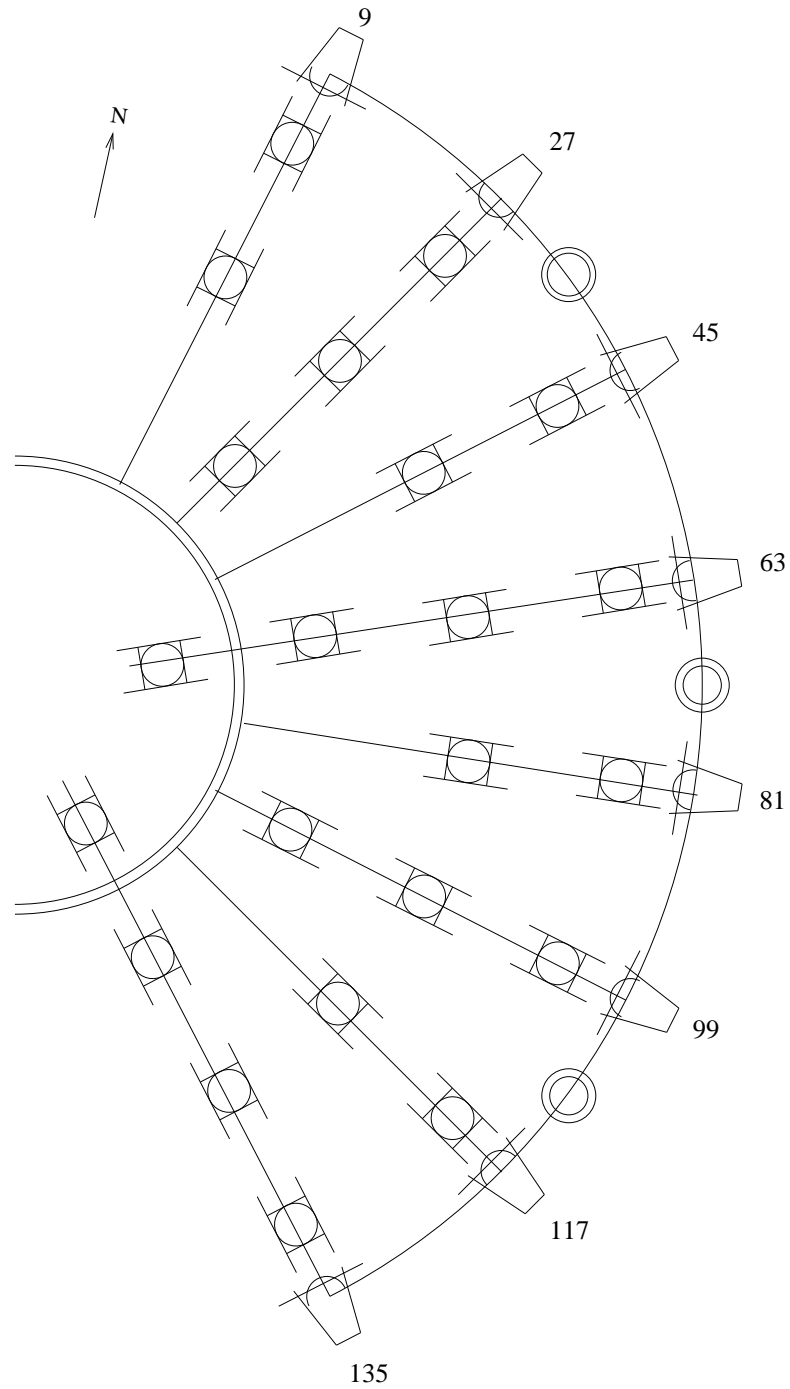


Figure 4.8: PMT location guide 2. This view shows the angular distribution of PMTs in the Outer Detector. Visible is part of the bottom region layout as well as the position of the side PMTs. The top region has the same angular layout as the bottom.

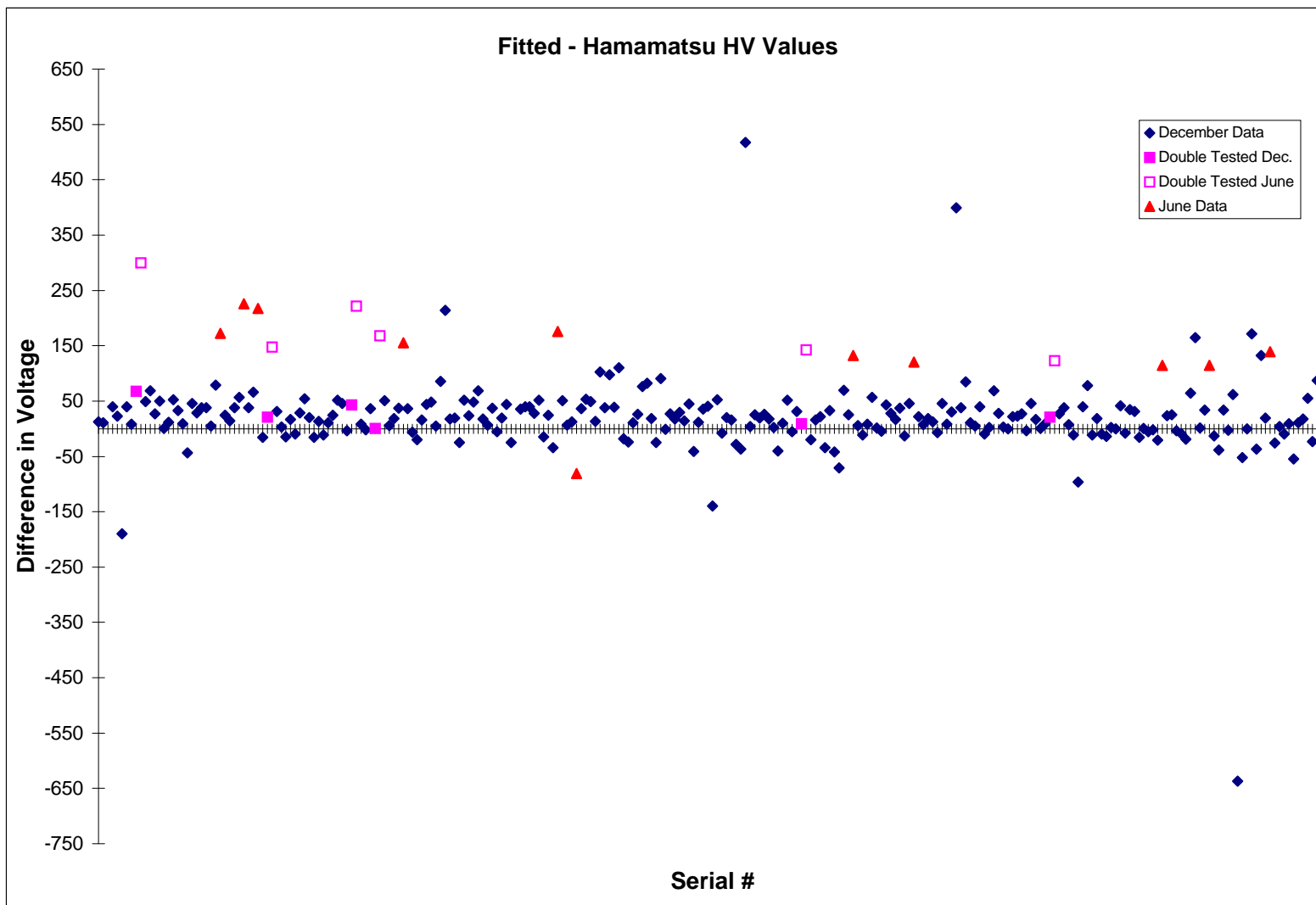


Figure 4.9: Fitted versus Hamamatsu high voltage values at 0.6×10^7 gain. Every tested PMT had its high voltage calculated for $G = 0.6 \times 10^7$. The difference, ΔV , between the tested data and Hamamatsu's values are shown above. The figure contains both December and June tested PMTs and includes the six PMTs that were tested in both months. There is an increase in the gain values for the June test. It is believed that this was caused by temperature effects on the laser and electronics.

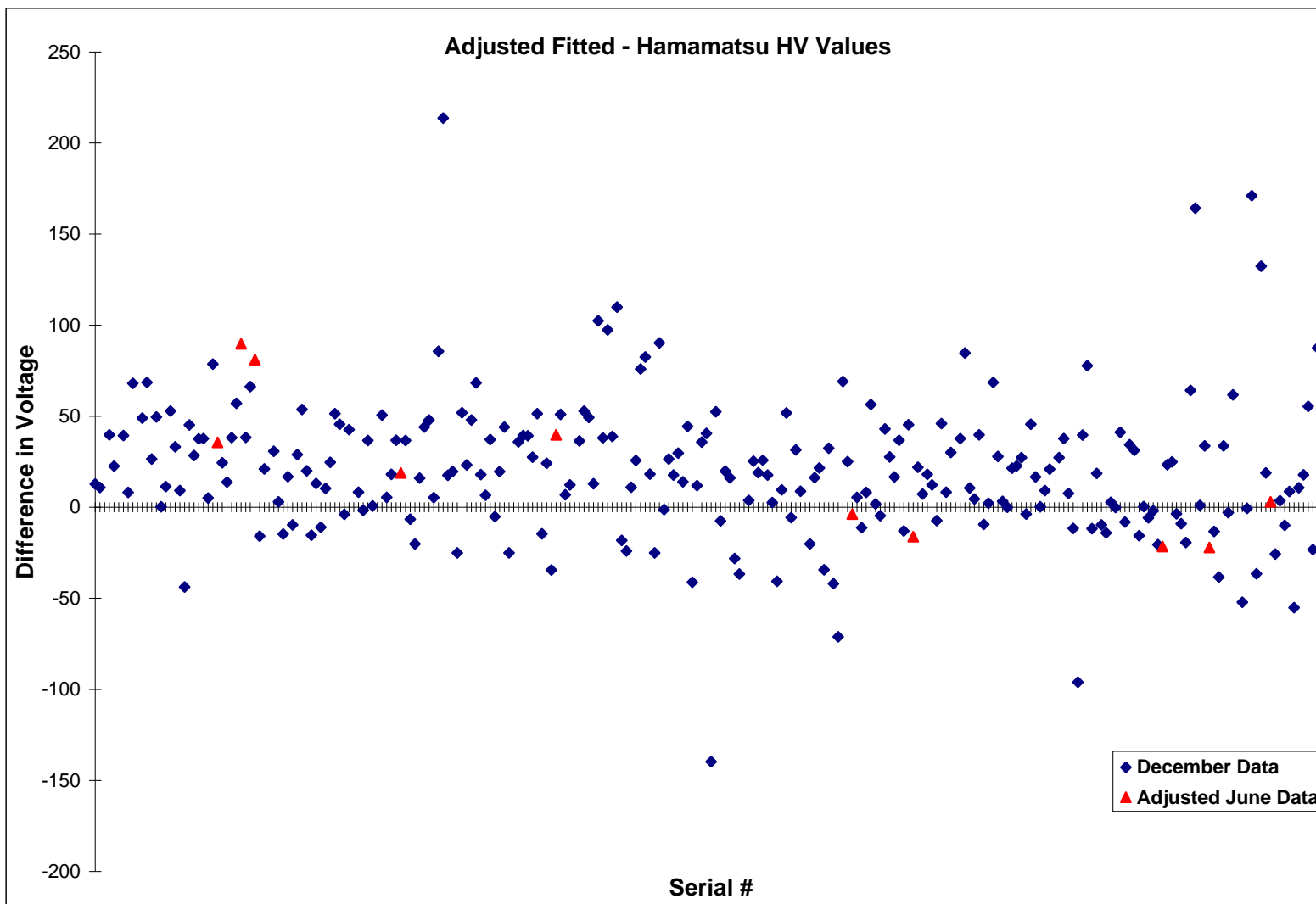


Figure 4.10: Adjusted fitted versus Hamamatsu high voltage values at 0.6×10^7 gain. Because of the increased gain values of June tested PMTs, their difference in voltage, ΔV , were normalized at $G = 0.6 \times 10^7$ to the December test data. For the six double tested PMTs, the December data was used. Removing the outliers from the previous figure, the adjusted difference in high voltage between the tested values and those of Hamamatsu is shown above.

After all the calculations and fitting had been done, there were three additional cases where a PMT was rejected as being unfit for use in KamLAND. Due to factory specified voltage limits, PMTs that had a projected operational voltage greater than 2550 V were rejected. Secondly, PMTs were rejected if the gain response function was irregular. Finally, the dark current rate must be below 50 kHz. In addition, the testing region that includes the expected operating voltage for a gain of 1.0×10^7 was checked. For four PMTs (Serial #0053, #0272, #0757, and #3938), this voltage value lies beyond the testing range. The high voltage that corresponds to $G = 1.0 \times 10^7$ for these four PMTs was determined by extrapolating the gain response function. It should be noted that there is some level of uncertainty in projecting a high voltage since the gain response function will eventually saturate and there will be sensitivity to changes in the local magnetic field.

Of the 278 twenty inch PMTs tested, there were a total of 19 that were rejected (see Table 4.2). Thus, there are 259 PMTs available for use in KamLAND that have a good gain response curve, moderate operational voltage, and low noise. From these 259 PMTs, 225 were selected for installation. The number of each type is as follows: 95 type ‘A’, 60 type ‘B’, 51 type ‘C’, 15 type ‘SK’, and 7 of unspecified type.

Table 4.2: Rejected photomultiplier tubes

| <i>Serial # of PMTs</i> | <i>Reason for Rejection</i> |
|---|---|
| 3194, 3677 | Unable to hold high voltage |
| 3048 | Irregular gain response function |
| 0005, 0022, 0072, 0134, 0715, 4014 | Dark current rate above threshold |
| — — — | Operational high voltage above threshold |
| 0243, 0244, 0250, 0299, 0357, 3330, 3335, 3514, 4740, 5362 | Failed after installation and replaced |

Chapter 5

Construction of the Outer Detector

The construction process started in October 1999 and went through the closing of the Outer Detector hatch in April 2001. Several small projects were needed to solve various problems and meet design parameters as the Outer Detector was being built. The projects included refurbishing the PMTs, obtaining cable, developing a splicing design, and installing the PMTs and Tyvek.

5.1 Refurbishment of the PMTs during Testing

During the testing phase in Sendai, several actions were performed to refurbish the PMTs for eventual re-use. It was noted that many PMTs had dust, grime, grease and remnants of epoxy on the glass in the photocathode region. The PMTs were given a preliminary cleaning by the testers and then a final cleaning by members of the Honda-Seiki company.

Waterproofing the PMT bases was also performed during this time since it was known that approximately 20% of Kamiokande's dead PMTs failed due to water leakage. This leakage is thought to have occurred whenever Kamiokande was emptied and refilled, thereby setting up thermal gradients that caused the original sealant to crack. Although KamLAND should experience very few filling cycles, the condition of the original sealant

and the age of the PMTs was a concern. Using a soft urethane based two part epoxy, the Pyrex/PVC interface at the base was coated and allowed to dry.

The last action taken during the testing phase was to remove the excess lengths of signal and high voltage cables for every PMT. During the breakdown of the Kamiokande experiment, the cables were cut for easy removal of the PMTs and they were left with approximately three feet of cable still attached at the base. It was assumed that during the subsequent handling and storage, these cables were likely to have suffered damage. Therefore, to minimize the possibility of failure in a water environment, both the signal and high voltage cables were cut to a length of approximately one foot to allow for cable splicing.

5.2 Cable Requirements and Splicing Design

The next step in preparing the PMTs for installation was to determine the cable routing and lengths for the cables and to decide how to splice the new cable with the original cables. Although the old signal cables were R-174 and the high voltage cables were RG-58, it was deemed best to use RG-58 cable for the signal and RG-59 for the high voltage, since these are standards today. The ‘RG’ denomination represents quarter inch coaxial cable with a resistance of 50 ohms. For added protection against water leakage, it was decided to buy blocked cable, which impedes the flow of water in the cable if there is a hole or cut in the outer jacket insulation. Blocked cable is made during manufacturing by forcing a liquid under the cable jacket which solidifies on the braid of the wire. This type of cable was used in both the Super-Kamiokande and the Sudbury Neutrino Observatory experiments. It was also necessary for the cables to have a polyethylene jacket, since this material does not promote algae growth when placed in a pure water environment.

Since the cables were connected to the PMTs after they had been installed, it was necessary to have a splicing design that was robust but quick and easy to perform with a high reliability factor. Because of the types of cables being used, it was decided that

the TUNL design would use standard high quality BNC connectors to splice the two sets of cables together. Although blocked cable is slightly thicker due to the extra material, normal BNC connectors can still be attached successfully. The BNC connectors are of the two-part crimp style, which is more reliable for electrical connections compared to the one-part crimp or the solder type of connectors. By crimping the ends with the proper tools, there is no reliance on soldering, which can be inconsistent and subject to failure as a result of mechanical or temperature stresses. In addition, a small amount of rubber silicon sealant, RTV-112, is placed into the BNC connector between the outer crimp jacket and the grounded cable shield to provide an additional water block between the outside and the inner connector.

For the high voltage splice, a standard female connector was crimped onto the PMT cable. The water blocked cable had a standard male connector placed on one end for the splice and an SHV connector crimped on the other end for connection to the high voltage power supply.

Because of the need for the inclusion of a $50\ \Omega$ terminator in the signal cable, the TUNL design incorporated a unique but simple and cost effective way of implementing this feature. Instead of using internal termination female-female barrels (approximate cost of \$26 each), simple female-male-female ‘T’ connectors were modified (cost $< \$3/\text{connector}$) by cutting off the male branch and leaving a straight barrel. A small ‘board type’ $\frac{1}{8}$ watt $50\ \Omega$ resistor was soldered in place across the exposed pin and epoxy was used to enclose the resistor and seal the cut branch. See Figure 5.1 for a diagram of the modified connector. The ends of the signal cables all have a standard male connector.

Finally, epoxy-lined shrink wrap was used to protect the PMT-side cables and another piece of shrink wrap was used to completely seal the splice. A small metal standoff was used on the PMT-side signal cables to provide an increased radius for the outer shrink wrap to seal. With this method, a large part of the cable preparation was able to be done at TUNL, ensuring cost effectiveness without compromising leak protection.

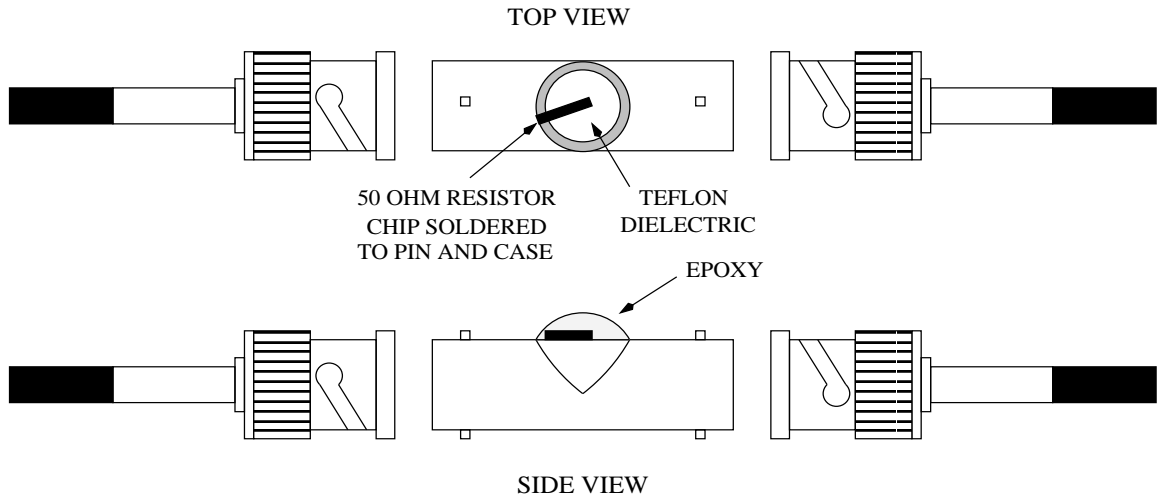


Figure 5.1: A standard ‘T’ connector was modified to produce a $50\ \Omega$ terminated straight barrel.

The splicing method was tested at TUNL using both high pressure air and high pressure water. The BNC plug ends were crimped with RTV-112 sealant onto the ends of regular (not water blocked or treated) RG-58 cable. A few cuts were sliced into the outer jacket of the cable in one area. A Swagelock ‘T’ and fittings were placed around these cuts for the attachment of an air hose or water hose. Approximately 60 psi of Argon gas was forced into the cable through the cuts in the outer jacket. The splice and ‘T’ fittings were immersed in water to look for escaping gas bubbles, which would signify a leak. However, there were no leaks around the Swagelock fittings nor from the BNC ends. The test was then continued for a period of three weeks with 40 psi of water without any leaks. Since these pressures were far greater than what is expected at KamLAND, the TUNL splicing method was proven robust.

This splicing design worked for every type of PMT except the ‘SK’ model, which does not have two separate cables protruding from the PMT base. The ‘SK’ model has a single cable jacket that houses both the high voltage and signal cables. Therefore, a small electronics board, developed by the University of Tennessee for the Inner Detector PMTs,

was used. Because of this complication, the splicing was done at Sendai during the assembly of the PMTs with frames and shielding. To install the small board, the cable was cut about two feet from the PMT. The outer jacket was pulled back so the high voltage and signal cables could be stripped and then soldered onto the board along with the accompanying water blocked cables. Shrink wrap was heated up to the board, at which point RTV-112 was injected into the wrap around the board. Because two cables come out from the other side of the board, the shrink wrap was slit lengthwise a few inches to allow the wrap to contract around both cables and seal to itself. Heating of this side of the shrink wrap locked in the RTV and provided another layer of protection against water leakage.

5.3 Cable Routing Scheme

It is desirable to have the Outer Detector and Inner Detector PMT signals arrive at the electronics at the same time. Due to velocity matching of the two sets of cables, the Outer Detector signal cables had to be 42 m in length while the Inner Detector cables were 40 m. Since these lengths allowed the cables to just reach the dome area, additional extension cables were needed to reach the electronics hut (e-hut) and connect to the electronics. There were no restrictions on the high voltage cable lengths other than the requirement that they reach the high voltage distributors in the hallway outside the dome entrance.

The cables make their way out of the detector cavity and into the dome by way of two cable holes at 130° and 298° . Figure 5.2 shows the locations of the cable holes, the e-hut, the high voltage distributors, and the cable routes of the signal and high voltage cables across the dome.

5.3.1 Signal Cables

The top PMTs were hung on the ceiling beams, which run radially out to the wall. Using these supports, cables were then routed along each beam to the wall where that beam's signal cables were bundled together. From these points, the bundles were routed

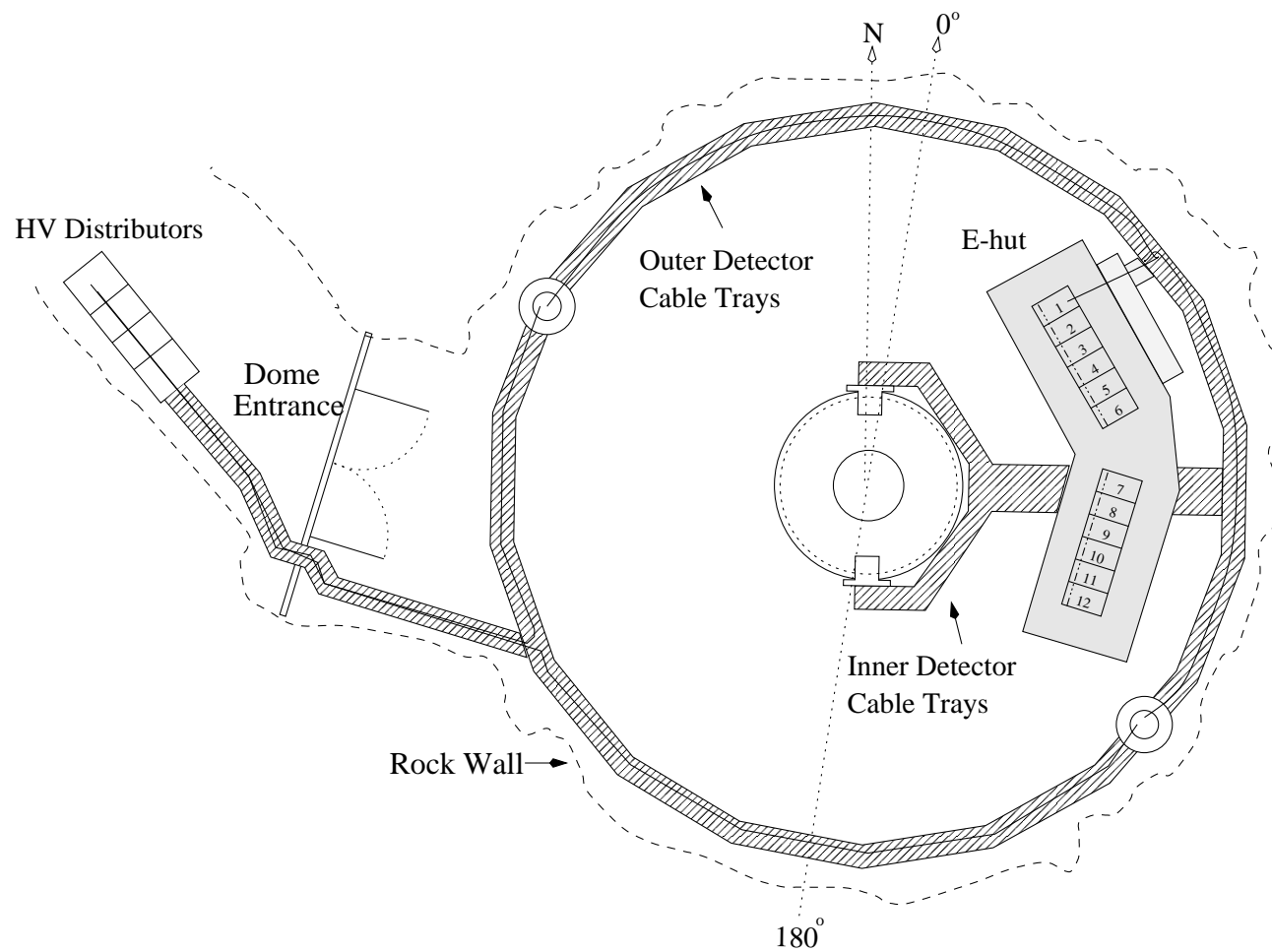


Figure 5.2: Layout of the dome area. The location of the electronics hut, high voltage distributors, and cable holes are shown for the dome area. The Outer Detector signal cables follow the circumference of the dome from the cable hole to crate #6 in the e-hut. The high voltage cables are routed to the south side of the dome entrance, where they then go through the wall to the far distributor.

straight to the nearest cable hole, as seen in Figure 5.3. Supporting frames and beams were used to secure the cables and keep them above the photocathodes and behind the Tyvek to prevent shadowing.

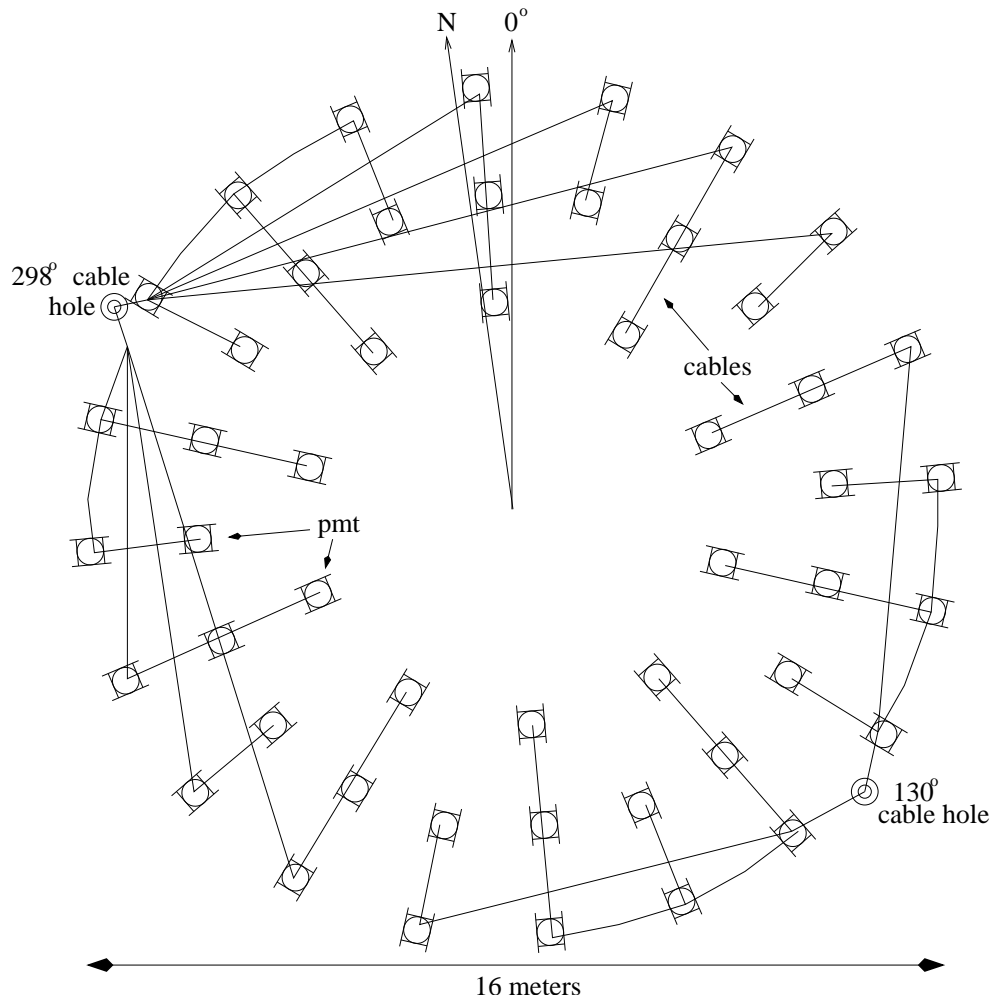


Figure 5.3: Cable routing for top PMTs. Cables travel along each radial beam to the wall, then are routed directly to the nearest cable hole.

For each column of six side PMTs, the signal cables were strung up the column's support structure to the ceiling. From these points, the six bundled cables were routed straight to the nearest cable hole. Like the top PMTs, the cables were secured to the support structures and behind the Tyvek.

The PMTs on the bottom section were the limiting factor in meeting the length requirement since they are the farthest from the cable holes. The routing scheme used the PMT support beams on the floor to secure the cables and keep them below the photocathode. These beams run radially out to the wall, where the cables were then routed around the circumference of the detector cavity to the side PMT supports that are below the cable holes. Each group of cables were secured to this support structure up through the cable hole into the dome. Figure 5.4 shows the routing pattern for each bottom PMT.

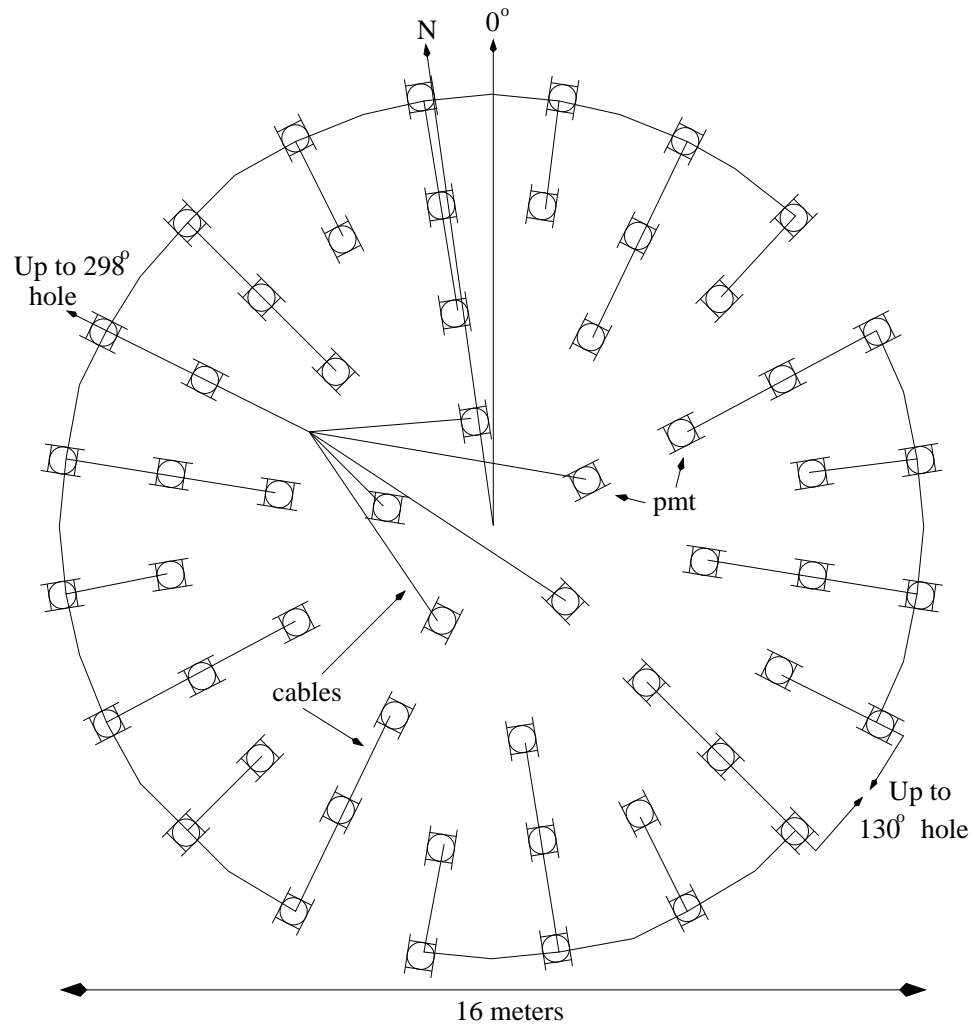


Figure 5.4: Cable routing for bottom PMTs. Cables travel along each radial beam to the wall, then are routed around the circumference to the side PMT supports that lead up to the nearest cable hole.

Signal cables that pass through the 298° hole traveled along the circumference of the dome towards the e-hut as shown in Figure 5.2. Cables from the 130° hole entered the dome directly behind the e-hut where they meet with the other signal cables at the cable entrance of the e-hut.

5.3.2 High Voltage Cables

The high voltage cables followed the same routing as the signal cables for each of the three regions to the dome from the Outer Detector cavity. The high voltage cables entering the dome from the 130° hole enter a cable tray and travel around the circumference to a position near the entrance to the dome at 244°. Cables routed to the 298° hole also enter a cable tray, travel along the circumference of the room to approximately the 270° position, where they were then routed up and over the dome entrance and then back down to the floor at the 244° position. At this point all high voltage cables were in one group and pass through the wall next to the entrance. The high voltage power supply for the Outer Detector is located in the farthest power supply bin from the dome entrance. Therefore, the cables traveled up and over the supply bins and then back down to the individual plugs in the rear of the Outer Detector bin.

To keep the amount of cable to a minimum, cable lengths were split into three groups: bottom PMTs, lower hemisphere PMTs, and the top and upper hemisphere PMTs. Calculations of the lengths based on the aforementioned routing gave the bottom PMTs a maximum length of 70 m, while the lower hemisphere PMTs and the upper and top PMTs had lengths of 61 and 51 m respectively.

5.4 Cable Production

With these requirements, nine spools of cable containing 10,516 m of blocked RG-58 and 25,908 m of blocked RG-59 cable were purchased from South Bay Cable Company and they arrived at TUNL in late May of 2000. Using a long hallway covered with clean plastic

to prevent abrasions on the outer jacket, the cable was unrolled from the spools, measured to the various lengths required, and then cut by TUNL personnel. Each cable was then coiled and placed inside an individual plastic bag for further protection.

Next, the two appropriate BNC connectors were crimped onto the cable ends. The quality of the crimp was tested by using a voltmeter to confirm a closed circuit from pin-to-pin and from ground-to-ground and an open circuit from pin-to-ground. In addition, since it would not be known which cable would be connected to which PMT until splicing, small character labels were placed on each end of the coils. In this manner, the correct PMTs could be connected to the right channels in the electronics crate and high voltage power supply. Finally, the bagged cables were packed into crates and shipped directly to the Kamioka mine site in September 2000. Approximately 200 person-hours were used for this process of cutting and crimping.

5.5 PMT Frames and Shielding

During June 2000 in Sendai, those PMTs that were determined to be reliable and in good standing from the gain testing stage underwent further refurbishment. For the ‘A’, ‘B’, and ‘C’ type PMTs, heat shrink tubing was applied to the existing cables before the BNC connectors were crimped on. The crimps were tested by using a voltmeter and measuring $50\ \Omega$ on the signal cable and $5\ \text{M}\Omega$ on the high voltage cable. For the 13 ‘SK’ type PMTs, the actual splice was performed according to the procedure described in Section 5.2. Because these PMTs were newer and had a better seal around the base, it was desired to use these PMTs near the bottom where the water pressure would be greatest. Therefore, cables of 61 m were spliced to six PMTs that were to be placed on the lowest side level and cables of 70 m were spliced to the rest that would be placed on the bottom.

After the BNC crimping and heat shrinking, a μ -metal shield and wire cage were attached to each PMT. The μ -metal acts to shield the enclosed PMT from external magnetic fields, which can affect the amount of charge collected by the PMT. Finally, the PMT was

attached to a metal frame, which would be used to attach the PMT to the support structure in the Outer Detector. Labels which listed the PMT serial number were attached to the frame to aid in identification after installation. The completely refurbished PMTs were then placed in bags and secured in boxes. Approximately 14 person-weeks of TUNL labor was used to complete these tasks. The PMTs were then shipped from Sendai to the mine site in late July 2000.

5.6 Installation of PMTs and Tyvek

In December 2000, the framed PMTs were unpacked in the mine and epoxy was applied around the base of the PMTs at the boundary of the PVC and the old epoxy to further waterproof them. The 170 PMTs for the top and side levels of the Outer Detector were then provided to workers of the Mitsui Shipbuilding Corporation for installation because installation of these PMTs required maneuvering the framed PMTs on scaffolding and through tight spaces. Japanese insurance regulations did not allow for anyone other than the Mitsui workers to carry the PMTs around on the scaffolding. Bottom level PMTs were set aside until after the scaffolding was removed from the cavity and the bottom region cleaned.

After the installation of the side and top level PMTs, the high voltage and signal cables were strung and secured according to the routing schemes and connected to the PMTs' cables. Because the scaffolding would be removed before the bottom PMTs would be tested, extra cables were strung in the event that they may be needed as replacements at a later date. The PMT serial number, its location within the Outer Detector, and the associated labels for the high voltage and signal cables were recorded. The location code used to describe the PMT position can be found in Section 4.4.

To verify that the installed PMTs were still operable, testing was performed by putting them on high voltage and verifying the presence of a dark current signal. If the test did not show a signal, several additional tests were performed. First, the cable connection

was checked as well as verifying that the cables being measured were actually connected to the PMT being tested. If these checks passed, then the resistance of the PMT-side cables from the PMT were tested. If the PMT did not pass this test, it was determined to be dead and was replaced. If the resistance was satisfactory across the PMT-side cables, then the resistance of the PMT was measured across the whole length of the water blocked cables. At this point, it could be determined if a strung cable was bad and it was subsequently replaced.

Three PMTs were determined to be inoperable from the top and sides during the post-intallation testing and they were replaced. In addition, three high voltage cables needed to be replaced. Retesting was performed on these PMTs until all installed PMTs were shown to be operable.

With all the PMTs testing satisfactorily, the heat shrink tubing was then heated around the cable splice with a heat gun to ensure a watertight seal. Cables for the bottom PMTs were strung and secured down to the last level of side PMTs. There they were temporarily stored in plastic bags and hung off of the structure to keep them from being damaged during the removal of the scaffolding and the subsequent cleaning of the bottom region.

The next step was to install reflective Tyvek on the sphere, on the ceiling, on the walls, and below the top level PMTs. Stainless steel metal clips were used to attach the Tyvek to the radial beams on which the top PMTs were installed and to the radial beams 1.5 m below the top PMTs. On the sphere, there are external ‘ribs’ with evenly spaced holes which were used to secure the Tyvek to the sphere with thin stainless steel wire. For the walls, Tyvek was attached at the top to the outermost circumferential beam with the metal clips and then lowered to the bottom region. To prevent sagging and to keep the Tyvek against the rock wall, the thin wire was attached to bolts in the wall and strung across in front of the Tyvek. Finally, stainless steel staples were used to connect neighboring sheets of Tyvek. The edges of two sheets were folded over and then stapled to give greater stability to the seam. This was done to prevent losing photons through gaps into the area between the

Tyvek and the rock walls and to attain better separation between regions. The installation of PMTs and Tyvek in the top and side regions was completed by late February 2001.

In March 2001, Mitsui workers removed the scaffolding and cleaned the bottom region in preparation for the installation of the bottom PMTs and the bottom Tyvek. In the following month, the 55 bottom PMTs were installed by TUNL personnel. The high voltage and signal cables were removed from the plastic bags and routed to a PMT according to the routing plan. Testing of the bottom PMTs proceeded in the same manner as for the top and side PMTs, with three high voltage cables being replaced. The heat shrink tubing was heated when all the PMTs tested satisfactorily.

A separator layer of Tyvek was installed 1.5 m above the floor by using stainless steel clips to attach the sheets from beams around the circumference of the Outer Detector cavity to a beam near the bottom of the sphere. Tyvek was also laid on the floor and stapled to the Tyvek from the side walls. Edges of neighboring sheets were folded over and stapled together to provide an isolated region. This stage of installation was completed by the end of April 2001.

With installation finished, the Outer Detector was filled with water to a height of approximately one meter to measure the positional stability of the Tyvek and the stability of the water temperature, which is critical for stabilizing the Inner Detector balloon temperature during filling. It was determined that the metal clips and staples were sufficient for securing the Tyvek around the Outer Detector. In addition, the temperature gradient was noted to be very small. During this time, the bottom PMTs were retested since they were totally underwater and it was discovered that five PMTs had failed.

After draining the water, the dead PMTs were replaced. Upon examination, it was discovered that there were small slits in the cable jacket of the dead PMTs at the point where the cables exited the PMT base due to a lack of flexibility of the original epoxy. The slits allowed water to leak into the PMTs causing the failure. To ensure that PMTs with a similar base and cable exit point did not succumb to the same fate, epoxy was applied around the cable exit point to those PMTs that could be reached (the bottom two levels

of the side region and the bottom region). At this point, the access plug was closed and sealed and installation was complete [Mes01].

Chapter 6

Startup

The process of filling the Outer Detector with water coincided with the filling of the Inner Detector with liquid scintillator and buffer oil. This was done to protect and prevent stresses on the balloon due to the different densities of the liquids and to keep temperature gradients in the scintillator to a minimum. Filling of the Inner and Outer Detectors commenced in June 2001 and took three months to complete. On September 15, operational procedures were initiated and a period of four months was used for testing, connecting PMTs to electronics and power supplies, integrating the Outer Detector into the KamLAND data acquisition system, and trouble shooting.

The first objective was to connect each PMT to high voltage and verify the number of operating PMTs. Testing proceeded by setting the high voltage to 1500 V and looking for a dark current signal. By the end of November 2001, all 225 Outer Detector PMTs had been retested and it was determined that 23 PMTs were inoperable. The root of the problems were narrowed down to either the signal or the high voltage cable on the PMT-side with the failure most likely due to water leakage or thermal shock.

Several PMTs tripped around 500 V and this was evidence of a short, most likely due to water leakage. In the rest of the cases where the voltage did not trip but a signal was still not seen, the resistance in the high voltage cable was measured. If it was less than 5 M Ω , then the failure was somewhere along the high voltage path. Otherwise, it was

the signal path that held the cause of failure. It was determined that eight PMTs were inoperable because of a lack of a signal and fifteen PMTs were dead on the high voltage path. Appendix D lists the serial number, location, and the path of failure for these PMTs as well as others that have been deactivated over the span of the experiment.

The signal cables were routed into the e-hut and those PMTs that were still operating were connected to electronics crate #6 in rack 1. The high voltage cables were connected to a LeCroy 1440 power supply system with a computer interface. This interface allows each channel to be set to a specific voltage. Using the results from the PMT testing stage, the high voltages necessary for a gain of $G = 0.5 \times 10^7$ were programmed into the computer. Appendix C lists the serial number, PMT location, electronics board and channel number, and the high voltage board and channel number for each working PMT.

The KamLAND data acquisition system is comprised of the electronics boards where the PMT signal cables are attached in the e-hut. Each crate can hold 20 boards, with each board having 12 individual channels. Every channel is monitored individually by a discriminator, which determines whether an incoming pulse is above a set threshold voltage. If the pulse satisfies the discriminator, the signal is processed through an Analog Transient Waveform Digitizer (ATWD) chip, which captures the waveform. The ATWDs only digitize the waveform when a trigger signal is sent to the electronics board. The time-dependent waveform voltage is converted to charge during the offline analysis.

The data acquisition system uses two different triggering modes: global triggers and forced triggers. During normal data acquisition, a global trigger is used. This trigger system looks for the total number of PMTs to fire in a particular region over 125 nanoseconds, called the NSUM, to be greater than a set value known as the NSUM threshold. When the threshold value is surpassed, the global trigger system sends a signal to the ATWDs. Waveforms that cross the discriminator threshold and occur in coincidence with the trigger signal are then captured and digitized [Ber00].

Forced triggers are used for calibration and for measuring the ATWD pedestals. For this process, a signal is sent from the trigger system which causes the ATWDs to both

capture and digitize whatever waveforms are on the signal line at the time of the trigger signal. The discriminator is bypassed in this mode [Ber00].

Data acquisition of all regions occurs for every global trigger of the Inner and Outer Detectors, corresponding to trigger rates of about 30 Hz and 10 Hz respectively. Because the Outer Detector has four regions, as described in Section 2.3, only one section needs to surpass the global trigger to cause data acquisition.

The threshold settings of the Outer Detector play an important role in determining the efficiency with which muon events are detected. Setting the discriminator and NSUM thresholds too low causes the ATWDs to become swamped by noise, while having thresholds set too high cuts real events. By optimizing these two parameters, all physics events can be captured without the introduction of overwhelming noise.

The discriminator threshold for the Outer Detector PMTs was therefore set at one millivolt, which is approximately the peak height in volts for a pulse associated with the collection of 0.5 photoelectrons in a PMT with a gain of $G = 0.5 \times 10^7$. This threshold eliminates the noise produced by the electronics but is low enough to allow single photoelectron events to pass.

Determination of the optimal NSUM threshold for each of the Outer Detector regions can be done both experimentally and with simulations. By using the data acquisition rate as a guide, the NSUM values were determined through trial and error before KamLAND came online. It is desirable to have a trigger rate that is similar to the expected muon rate through the fiducial volume (0.7 Hz) and favorable to have a rate that is slightly higher. Although this latter strategy introduces more noise, it allows the muon events that produce low amounts of light to be retained.

After the Outer Detector electronics were incorporated into the KamLAND data acquisition system, several short data runs were performed to produce NSUM plots for each region, which could be compared across runs to determine the optimum NSUM settings. The NSUM plot is a spectrum that shows the number of times a set number of PMTs fired

for an event. For each data run, the discriminator level was set at 1.0 mV, whereas the NSUM threshold was varied.

Each data run lasted approximately five minutes, as this allowed enough statistics to be gathered. The NSUM plot for a particular run and region that showed few points and had a low trigger rate meant that the NSUM threshold setting was too high and was restricting the events that were recorded. Likewise, an NSUM plot that had a very large trigger rate and a large peak at low NSUM values represented a setting that was too low. The previous runs were used to continually narrow the range until the optimal NSUM values were determined.

Table 6.1 shows the final NSUM settings and the data rates by region. Data rates for each region are above that of the expected muon flux. The data rate for the bottom region is somewhat large but it was shown that using a higher NSUM value results in a trigger rate lower than 0.7 Hz. These values were then entered into the global trigger system. Official data taking started on January 22, 2002.

Table 6.1: Final NSUM values and data rates for a one millivolt discriminator level.

| <i>Region</i> | <i>NSUM</i> | <i>Rate (Hz)</i> |
|---------------|-------------|------------------|
| Top | 6 | 0.8 |
| Upper | 5 | 0.8 |
| Lower | 6 | 0.8 |
| Bottom | 7 | 1.4 |

Chapter 7

Simulations

In an effort to support the selected NSUM threshold values, model the efficiency for the tagging of through-going muons in the Outer Detector, and determine the spallation induced neutron background in the Inner Detector, various simulations have been performed. Implementation of the full tracking of the Čerenkov light with a detailed model of the Outer Detector geometry was performed through the use of the FORTRAN based GEANT code, version 3.21 [App94]. The results were analyzed using PAW.

7.1 GEANT Inclusions

The geometry of the Outer Detector was modeled from the actual construction blueprints. Included in the geometry are the size and location of the PMTs, the Inner Detector sphere, the support structures, and the location of the Tyvek. The materials that comprise the various components are also described in detail.

The volume of the simulated detector is comprised of two sections. The volume that contains the upper, lower, and bottom Outer Detector regions is that of a right cylinder with a radius of 9.70 m and a height 18.50 m. Above this is placed a truncated cone with an upper radius of 8.97 m and a height of 1.50 m. This volume comprises the top region and conforms to the actual shape to first order.

The reflectivity coefficient for Tyvek in air is approximately 90% although the value was unknown for Tyvek submerged under water. Through a series of tests at Duke University using a 633 nm Helium-Neon laser, this coefficient was determined to be $72 \pm 9\%$. Further studies on the optical input parameters validated the selections made for the PMTs and water and gave a consistent value for the Tyvek reflectivity at about 80% [Roh01].

The ability to modify the code to address different scenarios was also incorporated. These scenarios included varying the photocathode efficiency for single photons, deactivating PMTs to account for turned off PMTs, to measure changes in the tagging efficiency, and allowing for the input of either a muon or neutron spectrum.

Several studies of the muon flux were performed during the Kamiokande experiment and combined to construct a reliable muon spectrum unique to the KamLAND detector cavity. The muon spectrum predicts the muons to be traveling downward with an angular distribution up to 90 degrees from the vertical axis. The probability of muons arriving at KamLAND from the direction of the center of the earth is taken to be zero. The energy range of the muons used in the simulations had a lower value of 1.5 GeV, which allows for through-going muons only. The upper limit was set at 1500 GeV, since the probability of higher energy muons traveling through KamLAND is negligible.

A new approach developed by Wang et al. [Wan01] uses the Monte Carlo simulation package FLUKA to generate neutron energy and angular distribution spectra from cosmic ray muons and fit them to empirical formulae. These expressions were used to produce a neutron spectrum for use in the neutron background simulation.

7.2 Single Photon Conversion Probability

The GEANT code stops tracking particles and Čerenkov photons when they are either absorbed or when they exit the detector. If a photon is absorbed by a PMT, the PMT will register a ‘hit’ if the photon is converted into a photoelectron. For events where two or more photons are absorbed by a PMT, the probability of a hit is equal 100%.

However, the probability of a hit due to a single photon depends on the efficiency of the photocathode to convert the photon to a photoelectron. This efficiency is not known for the Outer Detector PMTs, since they do not have a well defined single photoelectron peak.

In order to study the effect of the photocathode efficiency, the code was modified so that the probability of a single photon causing a PMT hit could be varied. The effect of the single photon conversion was expected to be small since most of the simulated muons create tens of thousands of photons per event. The exception would be those muons that skim the Outer Detector volume and produce relatively few photons.

To determine the extent of this effect, single photon conversion probabilities of 1% and 99% were used to provide an upper and lower limit. Each simulation contained 5000 events and included the full complement of PMTs. The same muons were generated for both runs for easy comparison of the effect. The photon spectrum produced by these muons is the same but the photoelectron spectrum is slightly altered due to the different probabilities, as seen in Figure 7.1.

Of the 5000 simulated muon events, there were 113 events in each dataset that did not produce any photons, meaning that these events did not enter the Outer Detector and can be labeled as ‘rock’ events. For the 1% case, there were eight events that produced photons but no photoelectrons, while there were only two such events for the 99% case. The number of photons produced by these ten events were less than 7.0×10^3 , which corresponds to less than 2% of the mean number of photons produced per event for all those events that produced photons. Although these ten events entered the Outer Detector, they had short track lengths and did not trigger any PMTs. Therefore, these events are labeled as ‘skimmers’.

The current operating NSUM threshold values of 6-5-6-7 (as described in Chapter 6) are applied to the data to determine the total number of simulated muon events that go undetected in the Outer Detector. This number is given by those events that do not exceed the NSUM threshold in any of the four regions. The total number of undetected events is comprised of skimmer, rock, and ‘below threshold’ events, which are those that hit at least

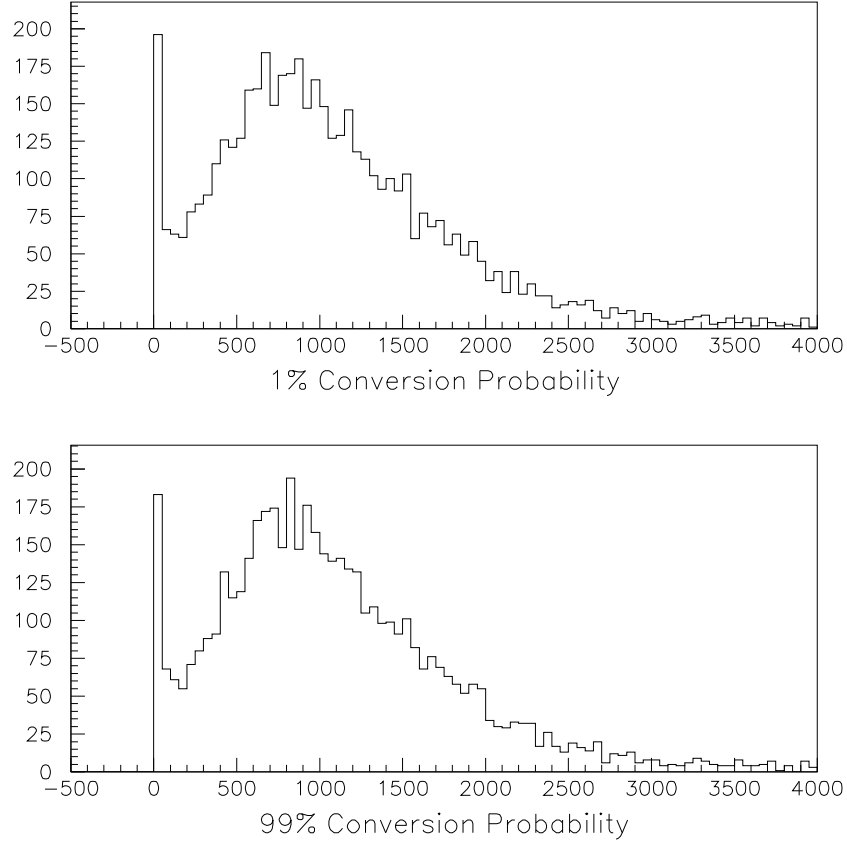


Figure 7.1: Photoelectron spectrum for different photocathode conversion probabilities. The plots show the number of photoelectrons produced per muon event. The top plot is for a single photon conversion probability of 1% while the bottom plot is for a probability of 99%. 100 muon events not plotted produced more than 4000 photoelectrons and were excluded to show variations at low numbers.

one PMT in at least one region but did not exceed the NSUM threshold in any region. Using Poisson statistics for the error, a total of 157 ± 13 events are undetected for the 1% case while 123 ± 11 events are missed for the 99% case. Table 7.1 separates the three event types for each simulation.

The overall Outer Detector efficiency is determined by the equation

$$\text{Efficiency} = \frac{\# \text{ simulated events} - \# \text{ total undetected}}{\# \text{ simulated events} - \# \text{ rock events}} \quad (7.1)$$

where the total undetected is the sum of the rock, skimmer, and below threshold events.

Table 7.1: Breakdown of undetected events in the Outer Detector for 1% and 99% single photon conversion probabilities for 5000 events.

| <i>Event Type</i> | <i>1% Case</i> | <i>99% Case</i> |
|--------------------|----------------|-----------------|
| Rock | 113 | 113 |
| Skimmer | 8 | 2 |
| Below Threshold | 36 | 8 |
| TOTAL | 157 | 123 |

Since the rock events never enter the Outer Detector, they can not be detected and are not used to determine the efficiency. Using Equation 7.1, the overall efficiency for the 1% case is $99.1 \pm 0.3\%$, while the 99% case has an efficiency of $99.8 \pm 0.3\%$. These results show that the detector efficiency is not greatly affected by the single photon conversion probability since most muon events produce more than one photoelectron per PMT. Because this effect is negligible, subsequent simulations will use a single photon conversion probability of 50%.

7.3 NSUM Verification

Although the NSUM threshold values were experimentally determined, it is important to show that the simulations confirm these thresholds as the optimal settings. A 5000 event simulation was performed using a single photon conversion probability of 50% and the full complement of PMTs. The dataset was used to compare the effect of several different NSUM thresholds on the overall efficiency of the Outer Detector.

7.3.1 NSUM Plot Features

During the experimental process of determining the optimal thresholds, several settings were tested. For the low NSUM thresholds, data rates were very high because noise and other non-muon events were triggering the system. Meanwhile, the higher values had

data rates below the expected muon flux. This meant possible physics events were not being captured.

The reason for the variability in the KamLAND data rates over different NSUM thresholds is due to low photoelectron events arising from radioactive decay, electronic noise, and the dark noise of the PMTs. These events will typically cause a coincident signal to be registered in a few PMTs. Therefore, changing the NSUM settings near this noise threshold affects the data rate as well as the shape of the resulting NSUM plots.

However, because the simulations only include muons and secondary particles produced by muon interactions with the detector materials, there are no low signal background events. Since the muon events typically produce large numbers of photoelectrons, the likelihood of an event with a low NSUM is small, as seen in Figure 7.2. The spike at $\text{NSUM} = 0$ is due to the 115 rock and skimmer events which did not hit any PMTs.

The events can also be separated into corresponding NSUM plots for each of the four Outer Detector regions. Figure 7.3 shows the four plots without threshold cuts. Because the track of an event may not enter a particular region, that event would register in the $\text{NSUM} = 0$ column in that region's histogram. All such events are excluded to better show variations in the plots of Figure 7.3.

Because the incoming muons shower down into the detector, the top and bottom regions show the expected result of few events at NSUM values less than ten PMTs and a well defined peak at a value greater than any considered NSUM threshold. As seen in Figure 2.4, the sphere and chimney do not significantly block the Čerenkov light in these regions and the Tyvek separator helps redirect this light into multiple PMTs.

The plots of the upper and lower regions have interesting shapes, due to a larger number of events at lower NSUM values. The main reason the low light events occur is due to the presence of the Inner Detector sphere relative to the position of the Outer Detector PMTs (see Figure 2.4). Shadowing occurs, which causes events to be localized. This lowers the NSUM peak and introduces a 'smearing out' at lower values.

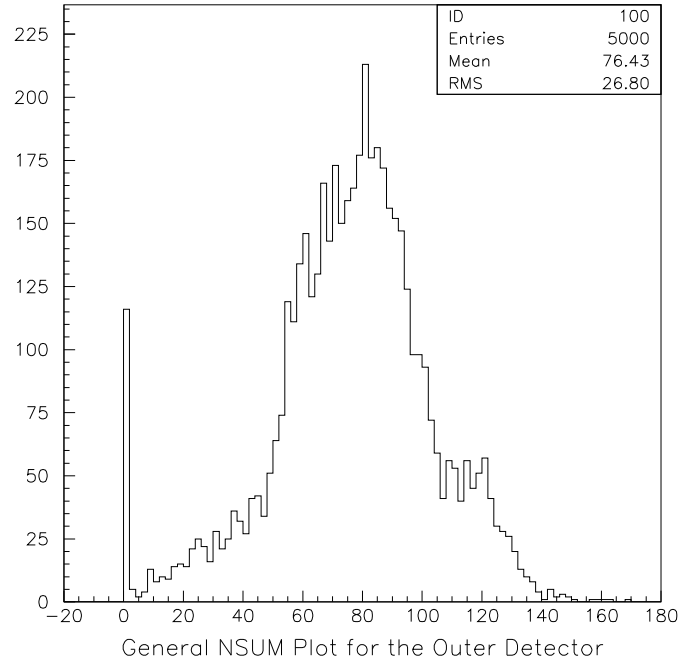


Figure 7.2: NSUM plot for the Outer Detector. The Outer Detector is shown as one region, where the number of events is plotted versus the number of hit PMTs. There are no threshold cuts in this plot. The 115 event spike at NSUM = 0 is due to the 113 rock events and 2 skimmer events that did not illuminate any PMTs.

In addition, the upper region plot shows another peak at very low NSUM values that the other three regions do not share. This phenomenon occurs because the lack of a Tyvek separator between the upper and lower regions allows small amounts of light to leak into the upper region from events that start in the lower region.

To understand this feature, it is necessary to look at the axial (z axis) starting points for the simulated muon events. In Figure 7.4, the number of PMTs that fire for each Outer Detector region is plotted versus the location of the starting point on the z axis for each event. The two Tyvek separators are located at ± 850 cm and $z = 0$ cm is the central plane through the KamLAND detector which separates the upper from the lower region.

In the top region, all triggered events are those that originate in the axial range between 850 and 1000 cm. Since the muon spectrum produces downward directed muons

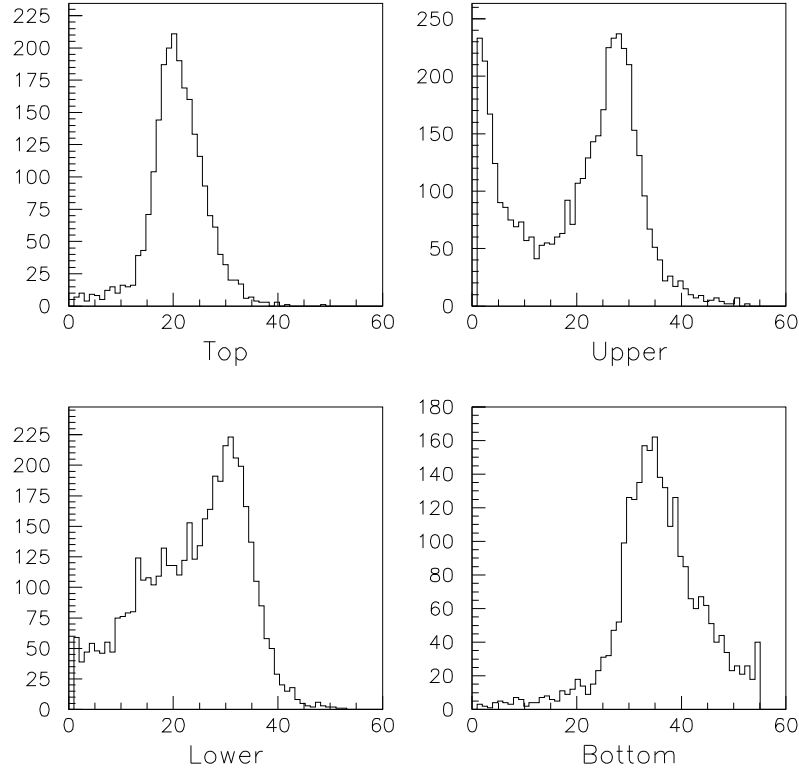


Figure 7.3: The NSUM plots for the four regions of the Outer Detector for 50% photocathode conversion probability. There are no threshold cuts and the events that did not hit any PMTs in a region are excluded.

and the Tyvek effectively seals the top from the upper region, any events that originate below 850 cm will not trigger the top PMTs. For the lower region, any event originating below -850 cm cannot trigger its PMTs because of the lower Tyvek separator. The bottom region can be triggered by an event that originates in any of the four regions and whose track enters into the bottom region.

The upper region can see events that originated in the upper half of the detector ($z > 0$ cm) as well as 1022 events that originated in the lower region. Figure 7.5 shows a histogram of the number of PMTs that fire for these 1022 events. From this plot, it is evident that these events are the cause of the low NSUM peak in the upper region.

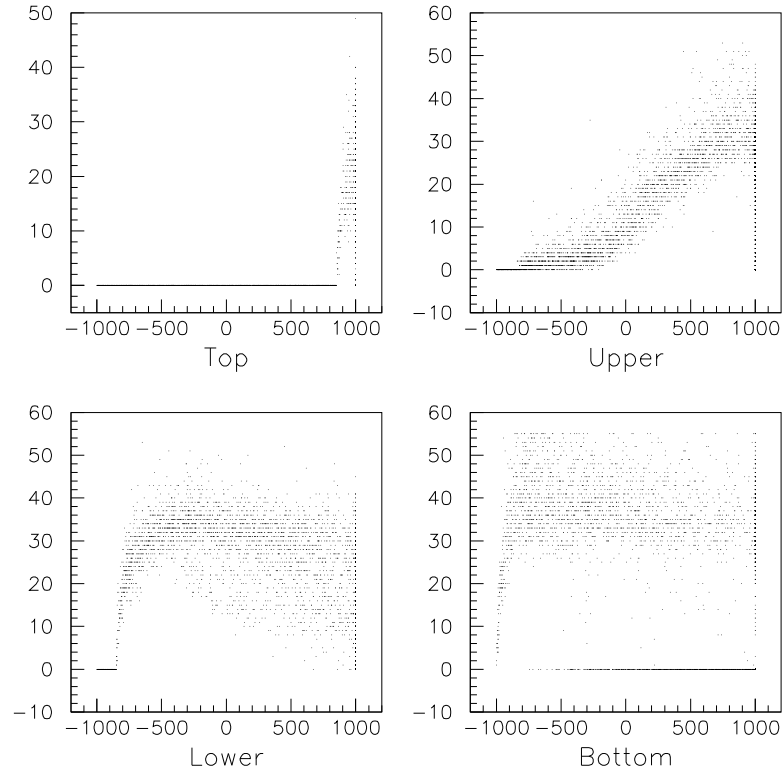


Figure 7.4: Starting points on the vertical axis for events in the four Outer Detector regions. The number of PMTs that fire in each region is plotted versus the z axis starting point of each event. ± 850 cm are the locations of the Tyvek separator. 0 cm is the central plane through the KamLAND detector separating the upper and lower regions.

Although the simulated muon events travel in the downward direction, some events have inclinations close to the horizontal. Figure 7.6 shows the sine of the angle of inclination for the 1022 events that originate in the lower region and register as events in the upper region.

The plot is preferentially peaked towards $\sin \theta = 1$, which when combined with the 41° angle of the Čerenkov light cone and the lack of a Tyvek separator at $z = 0$ cm, it becomes possible for light to leak into the upper region. There is also the likelihood of Čerenkov light reflecting off of the lower Tyvek separator and hitting PMTs in the upper

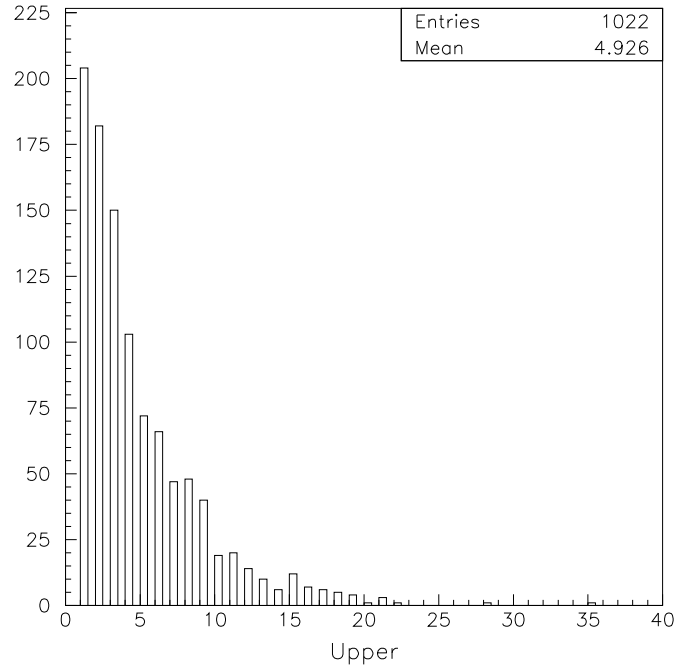


Figure 7.5: The NSUM plot of events originating in the lower region ($z < 0$ cm) and causing hits in the upper region. These events are the cause for the low NSUM spike in the upper region.

region as evidenced by those events with low values of $\sin \theta$. Removing the $z < 0$ cm events from the upper region results in the familiar NSUM shape, as shown in Figure 7.7.

7.3.2 Analysis of Different NSUM Thresholds

Using PAW, various cuts can be made on the same dataset to analyze the different NSUM thresholds. Although the number of below threshold events will vary with NSUM threshold, the number of rock and skimmer events will not be affected. For the dataset with a single photon conversion probability of 50%, there were 113 rock events and 2 skimmer events.

The first step is to analyze the number of below threshold events in each region. For each NSUM threshold combination, the missed events that remained after the NSUM

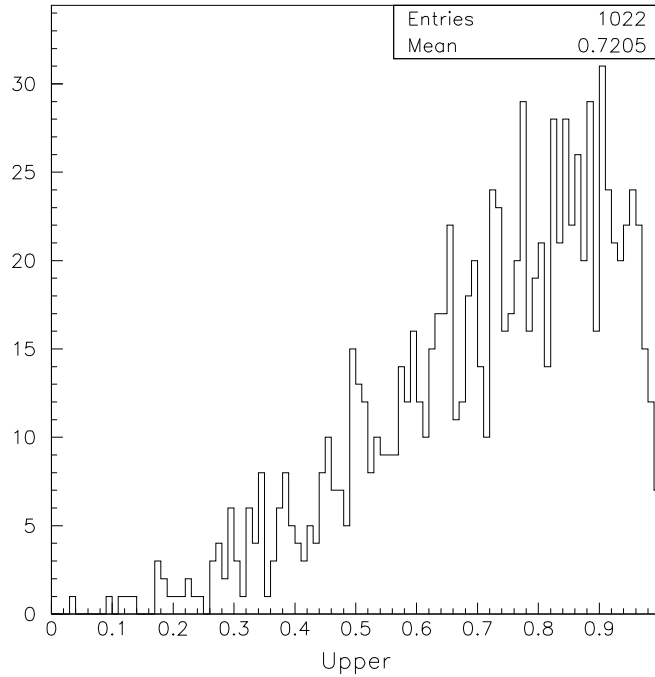


Figure 7.6: Angles of inclination for $z < 0$ cm events in upper region. Some events originating in the lower region have large inclination angles that when combined with the Čerenkov light cone, allow for light leakage into the upper region. Lower angle muon tracks produce Čerenkov light that can reflect off the lower Tyvek separator and also leak into the upper region.

cuts were found only in the top or bottom regions. Thus, the missed events only traveled through one region and did not trigger enough PMTs to be detected.

The sum of the events missed in the individual regions and the skimmers comprise the total number of missed Outer Detector events. Table 7.2 gives the number of missed events in the top and bottom regions in the Outer Detector and the corresponding efficiency for each of the NSUM threshold combinations. The efficiency is calculated according to Equation 7.1.

The simulation results confirm that any of the analyzed NSUM thresholds are valid selections for enabling the Outer Detector to meet the requirement of tagging $> 99\%$ of the through-going cosmic ray muons. However, since the simulations do not take into account

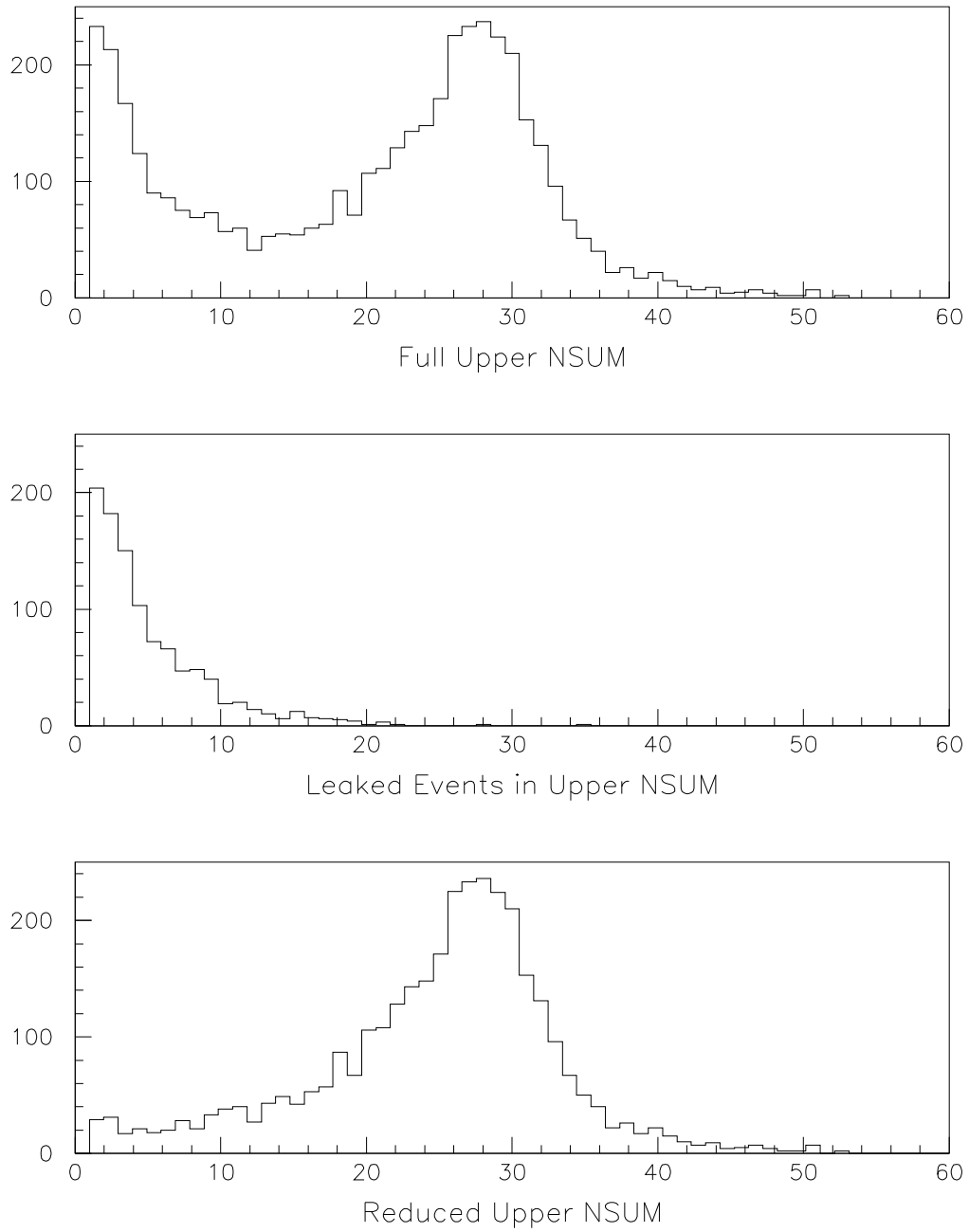


Figure 7.7: Events that originated in the lower region ($z < 0$ cm) and leaked light into the upper region have been subtracted out from the upper NSUM plot, producing the reduced upper NSUM plot.

Table 7.2: Efficiencies for various NSUM threshold settings. Results are for a 50% probability for single photon conversion. The two skimmer events are included in the *Total Missed* column. The bold faced row is the current NSUM threshold setting in the Outer Detector. The error for each efficiency value is $\pm 0.3\%$.

| <i>NSUM Threshold Values</i> | <i>Missed Events</i> | | <i>Total Missed</i> | <i>Efficiency</i> |
|------------------------------|----------------------|---------------|---------------------|-------------------|
| | <i>Top</i> | <i>Bottom</i> | | |
| 4-4-4-4 | 6 | 2 | 10 | 99.8% |
| 5-5-5-5 | 8 | 5 | 15 | 99.7% |
| 6-6-6-6 | 10 | 9 | 21 | 99.6% |
| 6-5-6-7 | 10 | 12 | 24 | 99.5% |
| 7-7-7-7 | 11 | 12 | 25 | 99.5% |
| 8-8-8-8 | 15 | 14 | 31 | 99.4% |

the low photon noise events, these results must be integrated with the experimental results. Therefore, the current NSUM thresholds of 6-5-6-7 are valid selections and will be used in the rest of the simulation analysis.

It is important to determine the origin of the below threshold events and their tracks through the region so that the reason for the event being undetected can be understood. Specific details like pathlength, the number of photons and photoelectrons produced, and the number of triggered PMTs can be found in Table 7.3 for each of these events.

The ten missed events in the top region each have a starting z position of 1000 cm. Seven have starting radial positions between 875 and 897 cm, meaning that these events will immediately enter the top region. These muons have large polar angles and are directed radially outward as they shower down, such that they quickly exit the top region through the side wall. The entrance and exit points of these muons are such that their paths lie behind the PMTs and the few photons produced must bounce several times in order to be detected. These events are shown in the table with actual values for their pathlengths.

The other three events have radial positions greater than 897 cm and are several centimeters away from the edge of the detector volume. In addition, these muons are

Table 7.3: Data for under threshold events. Listed are the 22 events that are below the NSUM threshold of 6-5-6-7. Events are ordered by the number of PMTs triggered, then by pathlength.

| <i>Event #</i> | <i>No. Hit PMTs</i> | <i>Pathlength (cm)</i> | <i>No. Photons Produced</i> | <i>No. PEs Produced</i> |
|----------------|---------------------|------------------------|-----------------------------|-------------------------|
| Top 1 | 5 | unknown | 10206 | 11 |
| Top 2 | 5 | 35.89 | 15819 | 11 |
| Top 3 | 4 | unknown | 4070 | 7 |
| Top 4 | 4 | 33.41 | 17871 | 8 |
| Top 5 | 2 | unknown | 2412 | 3 |
| Top 6 | 2 | 14.63 | 6179 | 2 |
| Top 7 | 2 | 14.96 | 6582 | 3 |
| Top 8 | 2 | 8.32 | 3013 | 2 |
| Top 9 | 1 | 14.51 | 5510 | 1 |
| Top 10 | 1 | 16.98 | 7788 | 3 |
| Bottom 1 | 6 | 17.82 | 6223 | 12 |
| Bottom 2 | 6 | 12.07 | 4074 | 8 |
| Bottom 3 | 6 | 5.69 | 1890 | 9 |
| Bottom 4 | 5 | 24.52 | 7999 | 13 |
| Bottom 5 | 5 | 11.15 | 4090 | 6 |
| Bottom 6 | 5 | 7.55 | 4563 | 5 |
| Bottom 7 | 5 | 5.09 | 2777 | 9 |
| Bottom 8 | 4 | 18.20 | 6101 | 12 |
| Bottom 9 | 4 | 9.74 | 3260 | 4 |
| Bottom 10 | 4 | 9.25 | 3087 | 7 |
| Bottom 11 | 2 | 4.08 | 1311 | 3 |
| Bottom 12 | 1 | 2.80 | 1252 | 2 |

initially directed radially outward, such that they would never enter the detector. However, these muons produce photons, indicating that they have scattered in the rock and into the top region. Because of this scattering, the entrance and exit points are now unknown. Therefore, the pathlengths are also unknown and are labeled as such in Table 7.3.

The 12 events in the bottom region enter from the wall and exit through the floor of the detector, with the starting z positions all within 17 cm of the floor. Therefore, the tracks of these muons are below the PMTs and any photons produced must bounce several times to be detected. Because the pathlengths of all 22 events are very short, the number of photons produced are relatively small compared to the average muon, causing the number of triggered PMTs per event to be below the NSUM threshold value.

Finally, in order to lend credence to the simulations, it is necessary to compare the simulation NSUM plots with NSUM plots obtained from KamLAND data. To make the comparison, the KamLAND plot is made by using only muon-like events from Run #677. This is achieved by using those light producing events that are triggered by the Inner Detector and produce a large amount of charge ($> 2 \times 10^6$ front-end-electronics voltage units). The NSUM plots for each region are plotted together in Figure 7.8.

The NSUM plots show the same general features, although there are some differences. Foremost, the peaks for the number of ‘hit’ PMTs for the KamLAND data are lower than the simulation data. This is because during Run #677, the Outer Detector had 46 PMTs that had been deactivated, while the simulations have the full complement of PMTs. In the top region, Run #677 shows a large number of events at low NSUM values. It is believed that the Tyvek separating the upper and top regions has been compromised, allowing light to leak into the top region from below while the simulation has complete separation. In the upper region however, the KamLAND data lacks the low NSUM peak which in the simulation occurs because of light leakage between the upper and lower regions. This difference can be explained by the method in which the KamLAND data selected muons for study. By taking muons that only pass through the Inner Detector, a bias towards muons

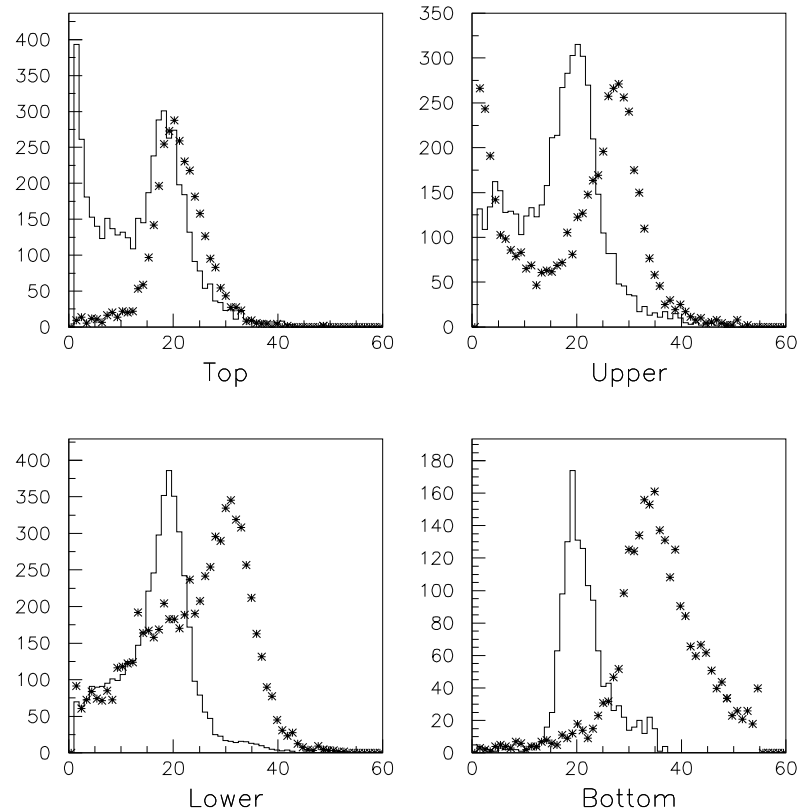


Figure 7.8: Comparison of normalized NSUM calculations with data for the four Outer Detector regions. The simulation NSUM data are denoted by * and actual NSUM data (Run #677) are denoted by the solid line. The simulation contains no deactivated PMTs, while Run #677 had 46 PMTs deactivated. As a result, the peaks do not coincide (see Figure 7.9).

that are not susceptible to shadowing is introduced and therefore, low NSUM events are largely eliminated.

7.3.3 Efficiencies for Various Outer Detector Scenarios

As noted in Chapter 6, several PMTs failed upon startup, and several more have been deactivated over the course of the experiment, as described in Chapter 8. Therefore,

it is necessary to repeat the above analysis and determine how the muon-tagging efficiency changes as PMTs are deactivated.

The code was modified such that any number of PMTs could be deactivated. Using the single photon conversion probability of 50% and the NSUM thresholds of 6-5-6-7, several scenarios with increasing numbers of PMTs deactivated were simulated. Four cases symmetrically removed approximately half of the PMTs in one section while keeping the other three regions activated. A fifth case combined the removed PMTs from the first four cases. The next scenario removed all the PMTs located in the first and third rings in every region. One scenario removed the same 46 PMTs as were deactivated during KamLAND data Run #677. One simulation with 15 active PMTs in each region was also performed. The various muon-tagging efficiencies are found in Table 7.4.

Table 7.4: Efficiencies for various scenarios of inactive PMTs. Results are for a 50% probability for single photon conversion and NSUM thresholds of 6-5-6-7. For each simulation, the number of PMTs deactivated is shown along with the resulting efficiency at tagging through-going muons.

| <i>Scenario Description</i> | <i># PMTs Deactivated</i> | <i>Muon-Tagging Efficiency</i> |
|---------------------------------|-------------------------------|------------------------------------|
| Half Top | 20 | $99.1 \pm 0.3\%$ |
| Half Bottom | 25 | $99.2 \pm 0.3\%$ |
| Half Upper | 30 | $99.5 \pm 0.3\%$ |
| Half Lower | 30 | $99.6 \pm 0.3\%$ |
| Sum of Above | 105 | $98.9 \pm 0.3\%$ |
| 1st & 3rd Ring | 140 | $98.3 \pm 0.4\%$ |
| Run # 677 | 46 | $99.0 \pm 0.3\%$ |
| 15 active/region | 165 | $95.1 \pm 0.4\%$ |

Although the first six scenarios had PMTs removed in a symmetric sequence, this would be an unlikely occurrence in reality. A more random distribution of inactive PMTs may decrease the tagging efficiency due to localized areas of inactive PMT coverage. However, in the simulation cases, enough of the Čerenkov photons produced by the muons are

detected by the remaining PMTs such that the efficiency does not decline very fast. These simulations indicate that the muon-tagging ability of the KamLAND Outer Detector is not greatly affected until more than half of the PMTs are deactivated.

For a better comparison of the NSUM plots, the same 46 PMTs that were deactivated in Run #677 were removed from the simulation. The NSUM plots in Figure 7.9 are produced in the same manner as Figure 7.8. The NSUM peaks now line up much better. The widths of the distributions for the lower and bottom regions are not fully understood and may also be affected by light leaks between the regions. But subject to the differences described in Section 7.3.2, the general consistency validates the ability of the simulations to reproduce KamLAND data.

Finally, using similar proportions of inactive PMTs per region as in Run #677, a simulation was performed with a distribution of 126 PMTs removed. Therefore, the top region has 15 inactive PMTs, the upper region has 26, the lower region has 35, and the bottom region has 50. These inactive PMTs are randomly distributed throughout each region. Because the bottom region only has five active PMTs, an NSUM threshold of seven effectively prevents this region from tagging any muons. Therefore, it becomes necessary to determine the effect of a change in the NSUM thresholds on the muon-tagging efficiency when the number of deactivated PMTs in a region approaches the threshold. The results for the simulation with 126 deactivated PMTs are found in Table 7.5. The conclusion drawn is that when the number of deactivated PMTs becomes large, it is possible to raise the muon-tagging efficiency by lowering the NSUM threshold values.

7.4 Neutron Background Study

As explained in Section 3.3, background events that are produced by muons traversing the detector are eliminated by virtue of spatial and time cuts around the muon path. With a muon-tagging rate in the Outer Detector of $> 99\%$, these neutron events can be rejected. However, neutrons from untagged muons cannot be detected and constitute a serious

Table 7.5: Muon-tagging efficiencies for 126 PMTs deactivated (top region = 15 inactive PMTs, upper = 26, lower = 35, and bottom = 50). The total number of missed events (rock, skimmer, and under threshold events) and the efficiencies of various NSUM threshold values are shown, including the current values of 6-5-6-7 for reference. There are 95 rock events in this simulation.

| <i>NSUM Threshold Values</i> | <i>Total Missed</i> | <i>Efficiency</i> |
|------------------------------|---------------------|-------------------|
| 6-5-6-7 | 382 | $94.1 \pm 0.5\%$ |
| 5-5-5-5 | 340 | $95.0 \pm 0.4\%$ |
| 4-4-4-4 | 284 | $96.1 \pm 0.4\%$ |
| 4-4-4-3 | 209 | $97.7 \pm 0.3\%$ |
| 4-4-3-3 | 208 | $97.7 \pm 0.3\%$ |
| 3-3-3-3 | 205 | $97.8 \pm 0.3\%$ |

background. Simulations are therefore an important tool in determining the background caused by these neutrons.

7.4.1 Inclusions for Neutron Studies

The GEANT3 code used in the muon simulations was modified to determine the number of neutron events that could mimic, or fake a neutrino event. Using empirical formulas for the neutron energy and angular distribution as described by Wang et al. [Wan01], a weighted data sample was calculated. The code was then able to select a neutron energy and polar angle according to the probability of the expected muon-induced neutron spectrum.

The Inner Detector region was simulated to first order as a sphere of buffer oil without PMTs and was included as a sensitive region for GEANT to monitor. Because the search for neutron events takes place only in the Inner Detector, the generation of Čerenkov light was turned off to save computation time and file space. Additional modifications allowed for the scattering energy recoils to be summed and the distance from the recoil vertices to the neutron capture calculated.

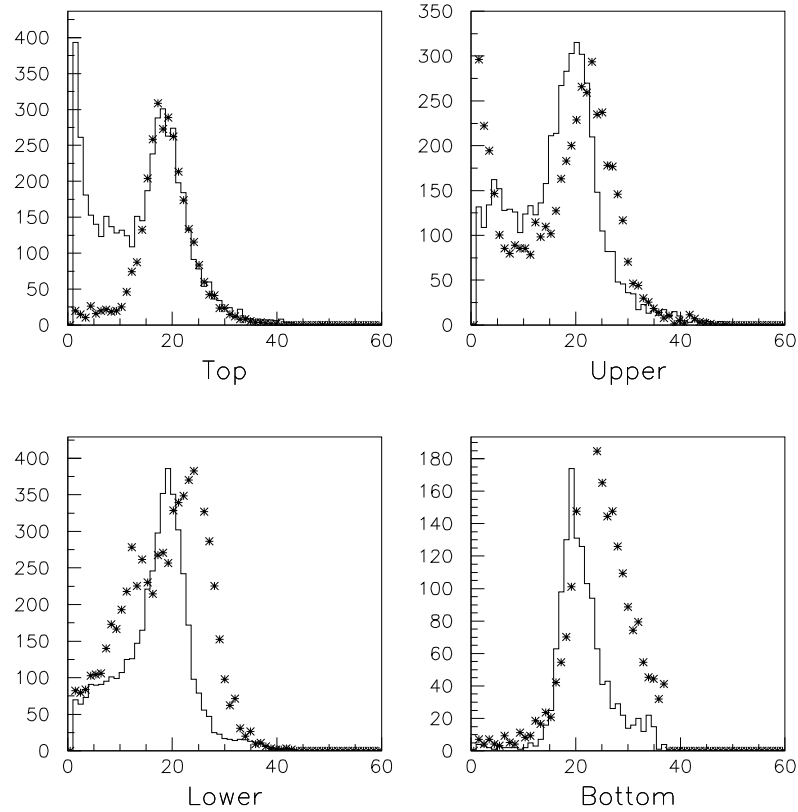


Figure 7.9: Comparison of normalized NSUM plots with deactivated PMTs for the four Outer Detector regions. The simulation NSUM plots for the four regions of the Outer Detector (denoted by $*$) are overlaid with the actual NSUM plots for data run #677 (solid line). This simulation removed the same 46 PMTs that were deactivated in Run #677. See text for further discussion.

The neutron transportation codes, FLUKA and GHEISHA, were invoked by GEANT to handle the hadronic interactions. However, these codes have a lower limit on the neutron energy of 10 keV, below which they become unreliable. Therefore, GEANT provides a capture vertex when the neutron reaches this limit. At energies below 10 keV, the only interactions that a neutron will have are elastic scattering and capture, primarily on hydrogen. To determine the actual capture vertex, neutron diffusion must be considered.

It can be argued that the scintillator is very similar to water in regards to its neutron moderation ability. Table 7.6 shows the density and molecular makeup for both materials. The density is similar, the number of hydrogen atoms is comparable, and the carbon and oxygen atoms are very similar in mass and scattering potential. Thus, to first order, the migration length of neutrons in water can be used to infer the mean distance a neutron will travel in the scintillator.

Table 7.6: Comparisons of various properties of water and KamLAND scintillator. The density of the KamLAND scintillator is slightly lower while the number of hydrogen atoms per carbon is similar to the number per oxygen in water. The scattering cross sections are given for O = oxygen and C = carbon.

| <i>Material</i> | <i>Molecular Makeup</i> | <i>Density (g/cm³)</i> | <i>σ_{sc} (barns)</i> |
|-----------------|-------------------------|-----------------------------------|---|
| Water | H ₂ O | 1.00 | O: 3.761 |
| Scintillator | CH _{1.97} | 0.78 | C: 4.746 |

Fission neutrons in water have a migration length, M of 6.4 cm [Byr95]. Since the mean square distance is given by

$$\langle r^2 \rangle = 6M^2 \quad (7.2)$$

the mean distance a neutron will travel is approximately 16 cm. Because fission neutrons have energies in the MeV range, this number conservatively overestimates the distance a 10 keV neutron will migrate in the scintillator from the GEANT determined capture vertex. This extra distance is accounted for when examining the data for fake events.

7.4.2 Data Cuts

There are three cuts that were made on the data in order to produce a listing of fake events. First, only neutrons that make it into the fiducial volume were considered, since this is also the only volume where the search for the neutrinos is undertaken. This

volume is defined as a sphere of scintillator with radius $R \leq 550$ cm, centered in the Inner Detector. Secondly, the location of the recoils must be within a distance $D = 160$ cm of the diffusion adjusted capture vertex in order to pass the spatial cut for a neutrino event. As discussed in Section 7.4.1, neutrons would not typically be expected to diffuse this far in a real neutrino event. This was the conservative value used in the actual KamLAND analysis and was therefore adopted in these simulations. Finally, after accounting for quenching, the sum of recoil energies must be in the range $2.6 < E_{e^+} < 8.0$ MeV in order to mimic a positron produced by a reactor anti-neutrino, where E_{e^+} is the equivalent positron energy. Events with E_{e^+} as low as 0.5 MeV are recorded as they provide a background for a possible study of geo-neutrinos.

The quenching factor is the relative suppression of light that is emitted by highly ionizing particles when compared to an electron depositing the same amount of energy. This factor is dependent upon both the scintillator material and the particle properties of charge and mass. The energy of the particle also determines the amount of quenching, with less energetic particles having higher quench factors.

Quench factors for gamma rays, protons, and alpha particles have been measured for the KamLAND buffer oil/scintillator mix with a series of experiments by other members of the collaboration using sources with known decay products and energy. Based on their results, Table 7.7 lists the values of the quench factors used in this neutron simulation to calculate E_{e^+} of the scattering recoils. The factors listed are associated with the lowest tested energy and thus, the largest quench values. These factors are then used for all energies. Therefore, the simulation results are conservative and overquench for more energetic particles.

7.4.3 Neutron Simulation Results

Fifty sets of 5000 randomly generated primary neutrons, for a total of 250,000 neutrons, were injected into the detector cavity from random starting vertices on the walls

Table 7.7: Quench factors used in the neutron background simulation. Factors are determined from tests performed on KamLAND scintillator. The largest quench factor for each particle type was used to provide a conservative estimate for the neutron background.

| <i>Particle Type</i> | <i>Quench Factor</i> |
|----------------------|----------------------|
| Electron | 1 |
| Gamma | 0.95 |
| Proton | 4 |
| Alpha | 13 |

and ceiling. Neutrons were tracked until they either exited the detector or were captured. Those events which entered the fiducial volume were tagged for closer analysis.

Figure 7.10 is a typical plot that shows the distance of the stopped neutrons from the center of the Inner Detector. As the distance a neutron travels increases, the number of neutrons that survive decline exponentially. Thus, in general, the distance the average neutron will travel is small relative to the distance between its origination and the fiducial volume. This can be seen in the region with a distance less than 900 cm, which is the Inner Detector. However, because the Outer Detector is not spherically shaped, the distance to the starting points from the center of the Inner Detector varies between 987 and 1393 cm, as shown in Figure 7.11. This causes a flattening of the exponential rise curve between distances of 987 and 1300 cm as most neutrons are captured in this region. At larger distances, there is less detector volume and the number of neutron captures decreases until the corners of the detector cavity are reached.

Due to inelastic hadronic scattering, a primary event can produce several neutrons that get tracked by GEANT. Through this process, the 250,000 primary events increased in number to approximately 390,000 total neutrons that were tracked in the detector volume. Of these, only 263 neutrons from 143 events were tagged as captures in the fiducial volume. These tagged neutrons were then analyzed to determine E_{e^+} of the recoils associated with each neutron, where a recoil is considered associated with a capture if it satisfied the spatial

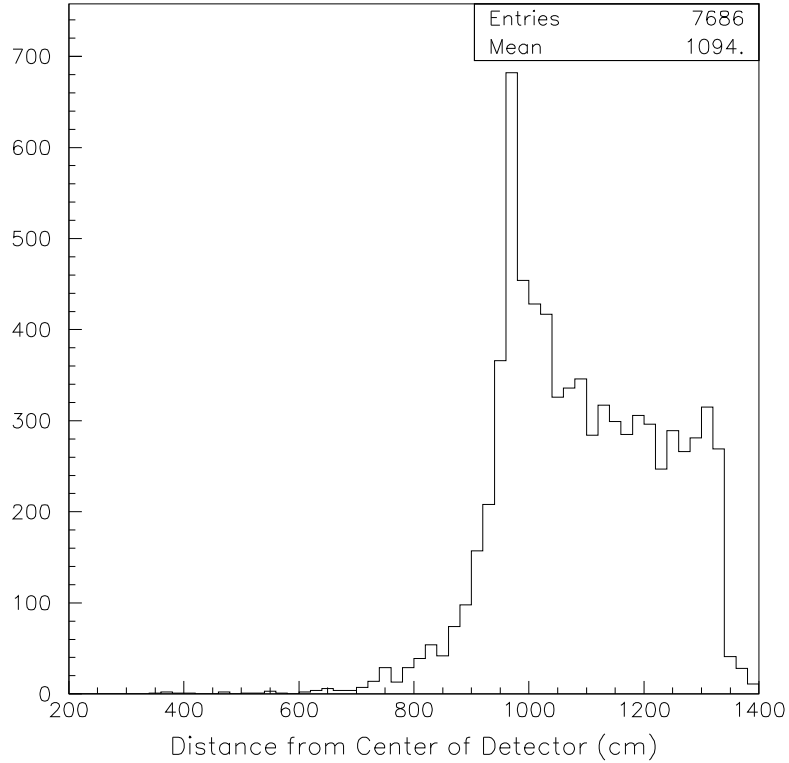


Figure 7.10: A typical plot of the distance from the center of the Inner Detector for each neutron that is captured in the detector cavity. 900 cm is the radius of the Inner Detector; 550 cm is the radius of the fiducial volume. Because the detector cavity is not spherical, the distance from the center of the Inner Detector to the edge of the Outer Detector varies from 987 to 1393 cm, as seen in Figure 7.11.

cut. It must be noted that it is possible for a recoil to be associated with more than one capture.

The analysis procedure for determining candidate neutrino events in KamLAND relies upon a vertex fitter that locates the origin of the positron. However, the fitter cannot distinguish multiple recoils that occur within 125 ns and will return a best fit vertex for an equivalent positron with the sum of the total energy of the recoils. This vertex must be less than 160 cm from the diffusion adjusted neutron capture vertex to pass the spatial cut for neutrino events. In order to emulate the KamLAND analysis, simulation events with

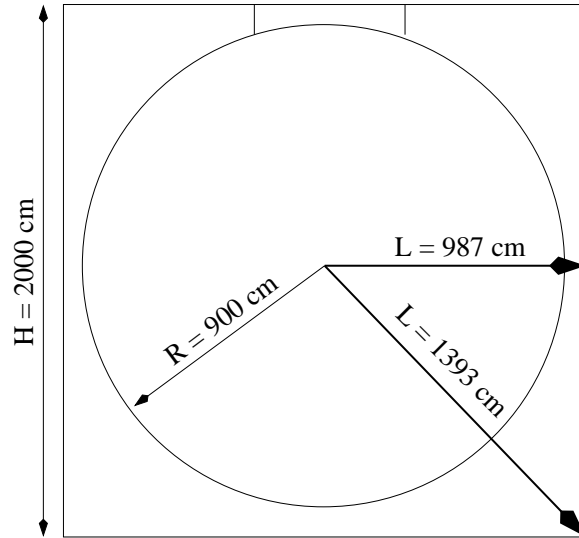


Figure 7.11: Distances to the center of the Inner Detector from various points. The shortest distance from the rock wall to the center of the Inner Detector is 987 cm, while the longest distance is from the corners of the Outer Detector at 1393 cm. This causes the flattened distribution of stopping distances in Figure 7.10.

multiple recoils are assumed to have the best fit vertex between the recoil vertices and close to the location of the recoil with the highest energy deposition.

Events with One Capture

There were 71 events with only one neutron capture in the fiducial volume. Table 7.8 shows the scattering process and recoil energy calculation for a typical single capture event. E_{e^+} was calculated for each scattering step and summed. For all but two events, the recoils occurred in close proximity to each other and within 160 cm of the capture. The KamLAND fitter would therefore fit these recoils to a vertex within the spatial cut and associate this vertex to the capture. For the other two events, the neutrons had a few interactions at distances greater than 160 cm, but since most of the energy was still deposited within the limit, the fitter would still place the equivalent positron vertex within the spatial cut.

Table 7.8: Typical scattering process for an event with one neutron in the fiducial volume. For each elastic scattering event, the initial neutron energy, the proton recoil energy, and the final neutron energy are listed. In addition, the distance from the recoil vertex to the GEANT determined capture vertex is also shown for each scattering event. The equivalent positron energy is calculated using the quench factor for protons: $E_{e^+} = \frac{10.49}{4} = 2.62$ MeV.

| <i>Scatter #</i> | <i>Initial Neutron Energy (MeV)</i> | <i>Recoil Energy (MeV)</i> | <i>Final Neutron Energy (MeV)</i> | <i>Distance (cm)</i> |
|------------------|-------------------------------------|----------------------------|-----------------------------------|----------------------|
| 1 | 10.49 | 9.85 | 0.64 | 4.1 |
| 2 | 0.64 | 0.47 | 0.17 | 2.5 |
| 3 | 0.17 | 0.04 | 0.13 | 1.7 |
| 4 | 0.13 | 0.04 | 0.09 | 1.4 |
| 5 | 0.09 | 0.09 | 0.00 | 0.0 |

Since these 71 events passed the spatial cuts, it was a simple process to determine fake neutrino events by comparing E_{e^+} to the positron energy data cut. There were five events that were in the $2.6 < E_{e^+} < 8.0$ MeV range and eight with $0.5 < E_{e^+} < 8.0$ MeV. Table 7.9 lists the distance from the furthest scatter to the GEANT determined capture vertex and the total energy of the recoils.

Events with Multiple Captures

The remaining 72 events contained 192 captures with varying levels of complexity. Most of these events started with one neutron entering the fiducial volume, only to inelastically scatter and produce two or more neutrons. In other cases, the inelastic scattering occurred outside the fiducial volume and multiple neutrons proceeded to scatter in towards the center of the detector. Multiple capture events in KamLAND would either be associated with the E_{e^+} or be isolated, depending on the fitted equivalent positron vertex relative to the capture position.

In 17 events, there was at least one neutron capture that was greater than 160 cm away from the other captures in the same event. These separate neutrons were very energetic

Table 7.9: Distance between neutron capture and proton recoils for fake events. For each of the seven fake events, the distance from the furthest proton recoil to the GEANT determined capture vertex is listed along with the total recoil energy. Note that this distance does not include the neutron diffusion length.

| <i>Recoil Energy</i> (MeV) | <i>Distance</i> (cm) |
|-------------------------------|-------------------------|
| 0.96 | 18.00 |
| 0.99 | 11.70 |
| 1.15 | 8.77 |
| 2.60 | 45.11 |
| 2.61 | 31.05 |
| 2.62 | 4.12 |
| 3.94 | 58.61 |
| 7.27 | 33.10 |

compared to the others and therefore deposited most of the event's energy near a single capture vertex. Although this yields a poor value for the equivalent positron vertex by the fitter, it would associate the entire E_{e^+} with this capture and effectively isolate the other captures with a null positron signal. In each case, E_{e^+} for these events was always much greater than 8 MeV, thereby rejecting all 17 events.

In the remaining multiple capture events, the neutrons were captured within 160 cm of each other and from the recoils. Although the vertex fitter may result in a poor fit, the value will still satisfy the spatial cut. For these types of events in KamLAND, the E_{e^+} is associated with the neutron that captures first within the time cut necessary for the coincidence. For purposes of the simulation, it was enough to choose one neutron and isolate the others. Next, the positron energy data cut was applied and it was determined that two events had an equivalent positron energy in the $2.6 < E_{e^+} < 8.0$ MeV range and four with $0.5 < E_{e^+} < 8.0$ MeV.

7.4.4 Estimated Neutron Background in KamLAND

For the reactor neutrino data cuts and using Poisson statistics for the error, there were 7 ± 3 fake events for 250,000 events giving a production rate of $R_f = 3 \pm 1 \times 10^{-5}$. There are twelve fakes when the E_{e^+} range is lowered to 0.5 MeV, an energy range that could include contributions from geo-neutrinos. Figure 7.12 shows a histogram of the energies of the twelve fake events.

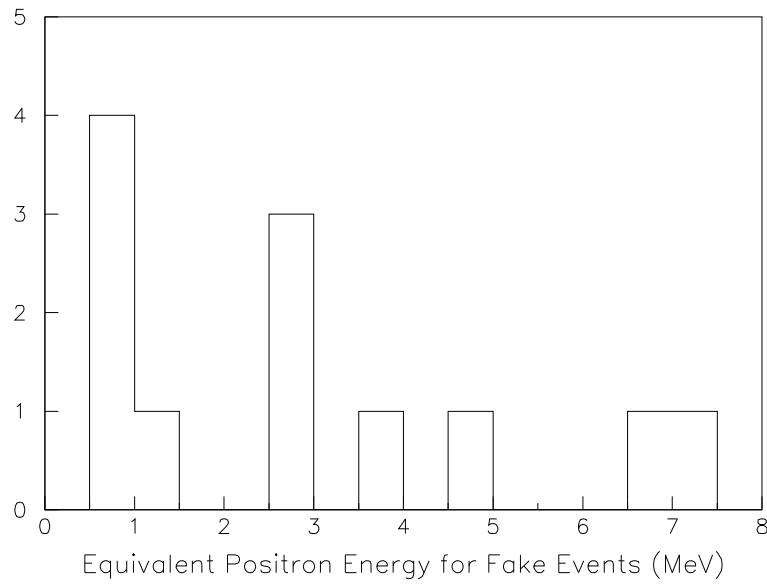


Figure 7.12: Histogram of E_{e^+} for fake events. Five events with energies below 2.6 MeV are not valid for the reactor neutrino phase of KamLAND. They are relevant, however, for the study of geo-neutrinos.

In general, N_n is the number of neutron background events that is produced by through-going muons, and is given by the equation

$$N_n = R_\mu(1 - \Upsilon)R_{\mu \rightarrow n}\chi\xi\Lambda R_f \quad (7.3)$$

where R_μ is defined as the muon flux rate (in Hz) through the region of interest. Υ is defined as the tagging efficiency for the through-going muons, $R_{\mu \rightarrow n}$ is the number of neutrons that are produced per muon per gcm^{-2} , χ is the effective thickness of the region in gcm^{-2} , ξ is

the fraction of neutrons that are directed in towards the detector volume, and Λ is the survival factor due to attenuation.

Because the tagging efficiency of muons in the Inner Detector is considered 100%, the neutron background stems from two situations: (1) that which is produced from muons that travel only through the rock annulus, denoted N_{nr} , and (2) that which comes from the untagged muons traversing through the Outer Detector, labeled N_{nOD} . The total background is the sum of these two cases. The tagging efficiency for the first case is $\Upsilon_r = 0\%$ while the efficiency for the Outer Detector with all PMTs active is $\Upsilon_{OD} = 99.51\%$.

R_μ and χ were determined by simulation using the KamLAND muon spectrum described in Section 7.1. A one meter rock annulus surrounding the detector was added to the detector geometry so that the muon flux through the different regions of the detector and the average pathlength through these regions could be calculated. The effective thickness, χ is obtained by multiplying the average pathlength by the density for each region. The results are shown in Table 7.10.

Table 7.10: Simulated muon flux rates, average pathlengths, densities and effective pathlengths. The muon flux and average pathlength values are determined from simulation for each region of the detector. Muons that pass through the Inner and Outer detector regions also go through the rock annulus. *Rock Wall Only* represents the pathlength of muons that pass through the rock only while *Rock→Water* is the pathlength in rock for those muons that pass through the rock and enter the KamLAND volume. *Rock Average* is the average pathlength through the rock regardless of which volume the muon traverses.

| <i>Region</i> | <i>Material Composition</i> | <i>Pathlength (cm)</i> | <i>Density (g/cm³)</i> | χ (g/cm ²) | <i>Muon Flux (Hz)</i> |
|----------------|---------------------------------|----------------------------|---------------------------------------|--------------------------------|---------------------------|
| Inner Detector | Scintillator | 842.9 | 0.78 | 657.5 | 0.22 |
| Inner Detector | Oil | 757.9 | 0.78 | 591.2 | 0.47 |
| Outer Detector | Water | 654.7 | 1.00 | 654.7 | 0.81 |
| Rock Wall Only | Rock | 466.7 | 2.70 | 1260.1 | 0.16 |
| Rock→Water | Rock | 337.9 | 2.70 | 912.3 | 0.98 |
| Rock Average | Rock | 359.7 | 2.70 | 971.2 | 0.98 |

Simulations on neutron production from muons by Wang et al. found the neutron yield as a function of muon energy to be

$$R_{\mu \rightarrow n} = 4.14 \times E_{\mu}^{0.74} \times 10^{-6} \quad \text{neutrons}/\mu \text{ per gcm}^{-2} \quad (7.4)$$

where E_{μ} is the mean muon energy at the detector [Wan01]. The mean muon energy for KamLAND was estimated using the normalized local muon spectrum described in [Cas73]. For the range of muon energies between 1.5 and 1500 GeV, $E_{\mu} \approx 216$ GeV. Inserting this value into Equation 7.4 gives $R_{\mu \rightarrow n} = 2.21 \times 10^{-4}$ n/ μ per gcm $^{-2}$.

Attenuation in the rock is not taken into account in the neutron simulation because the neutrons were injected into the Outer Detector from the surface of the wall. Assuming that neutrons are produced uniformly throughout the rock, the survival factor, Λ_{rock} , can be calculated by accounting for the variation in attenuation length with respect to neutron energy and population, as shown in Equation 7.5.

$$\Lambda_{rock} = \frac{\int_0^{2\text{GeV}} \int_0^{1\text{m}} N_n(E) \exp\left(\frac{-\ell}{\lambda(E)}\right) dE d\ell}{\int_0^{2\text{GeV}} \int_0^{1\text{m}} dE d\ell} \quad (7.5)$$

where $N_n(E)$ is the energy dependent neutron spectrum, ℓ is the distance into the rock, and $\lambda(E)$ is the energy dependent attenuation length for neutrons in rock.

By using the neutron spectrum described by Wang et al. [Wan01] and the plot of attenuation length versus neutron energy found in Hagiwara et al. [Hag02], the fraction that survive attenuation in the rock and reach the edge of the Outer Detector is found to be $\Lambda_{rock} \approx 19\%$. These calculations also show that 90% of the neutrons come from the first 50 cm of the surrounding rock, thereby justifying the consideration of neutron production to a one meter annulus only. Attenuation in the water is already accounted for by the neutron simulation and therefore, $\Lambda_{water} = 1$ when calculating N_{nOD} .

If it is assumed that roughly half of the neutrons travel in towards the detector, making $\xi = 0.5$ and the error of R_f dominates, the number of fake events for the case of rock only muons is $N_{nr} = (1.2 \pm 0.4) \times 10^{-7}$ Hz, where χ_{nr} is taken to be the *Rock Wall Only* effective pathlength of 1260.1 gcm $^{-2}$. For muons that enter the Outer Detector, the effective pathlength χ_{OD} is the sum of the *Rock* \rightarrow *Water* and *Outer Detector*

effective pathlengths multiplied by their respective survival factors. Again, taking $\xi = 0.5$, the number of fake events caused by untagged muons that enter the Outer Detector is $N_{nOD} = (1.1 \pm 0.3) \times 10^{-8}$ Hz.

Adding these numbers and converting the result to the total number of fake events over 145.1 days gives a background of 1.3 ± 0.4 neutrons, comparable to the value of 0.5 neutrons cited in the first paper of the KamLAND experiment [Egu03]. The simulation confirms that for an Outer Detector muon-tagging efficiency of 99.5%, the background due to spallation neutrons is indeed small and does not affect KamLAND's results.

The effectiveness of the Outer Detector becomes questionable when $N_{nOD} \approx N_{nr}$ because the neutron background starts to become dominated by neutrons produced by untagged muons. Setting $N_{nOD} = 1.2 \times 10^{-7}$ Hz and solving for the efficiency Υ_{OD} , the minimum Outer Detector efficiency is determined to be $94.8 \pm 0.1\%$. Based on the muon-tagging efficiencies in Table 7.4, dropping to only fifteen active PMTs per region will still have an efficiency greater than this minimum value. In addition, changing the NSUM thresholds to lower values as the number of deactivated PMTs increases (such as seen in Table 7.5) will allow the Outer Detector to maintain a muon-tagging efficiency greater than the minimum. Removing the Outer Detector from operation would result in 29 ± 9 neutrons over the 145.1 day period. Therefore, it is important to keep the Outer Detector in operation as long as it is able to actively veto through-going muons.

Chapter 8

Current Operational Status

KamLAND is still operational and has entered into its second year of data taking. The operational parameters of the Outer Detector, as described in Chapter 6, have not changed since startup. However, the number of PMTs that have been deactivated or have failed has increased from 23 at startup to a total of 73 as of June 30, 2003.

Because the Outer Detector PMTs are several years old and had not been stored in optimum conditions since the end of the Kamiokande experiment, it was expected that there would be some attrition over the lifetime of the experiment. The Outer Detector was designed to prevent the muon-tagging efficiency from falling to an unacceptable level by installing extra PMTs and using the reflective Tyvek.

PMTs are deactivated for two reasons: outright failure or high noise rates. Failures are characterized by the PMTs not being able to hold high voltage or carry a signal. This is most likely caused by a short in the electronics at the base of the PMT due to water leakage. Because there is much confidence in the splicing technique and in the water blocked cable that was used to make the PMTs functionable, the likely cause of these shorts comes from the original epoxy and PMT cables.

The original PMT cables were cut as short as possible and covered with heat shrink tubing in an effort to minimize the potential hazard of pinholes. However, due to the position of the cables with respect to the base, it was not always possible to cover the entire

cable with the heat shrink. During the preliminary water filling of the Outer Detector, there was also evidence that the epoxy was not properly sealing at the point where the cables enter the base for some of the PMTs. At the same time, it was noticed that cracks had developed in the sheathing of several cables due to abrasion between the pliable cable and the rigid structure at the point where they enter the base. Since installation was complete and the scaffolding had been removed, it was impossible to identify suspect PMTs except those that could be easily reached from the floor of the Outer Detector. The only solution was to apply epoxy to the affected areas.

PMTs that become noisy tend to disrupt the trigger rate for the particular region in which they are located. In some cases, the PMTs are labeled as ‘flashers’, implying that the PMT emits photons that trigger nearby PMTs. Recent analysis indicates that this scenario is not likely to be correct. For other situations, the dark noise rate of a PMT gradually increases until it is triggering constantly. It is generally thought that these actions are caused by a degradation of the photocathode due to age or other internal damage, such as small water leaks that are not sufficient enough to cause outright failure. In a few cases, external causes such as light leaks or the operation of fluorescent lights in the dome area have caused high trigger rates and the needless deactivation of PMTs.

At the conclusion of the filling of the Outer Detector with water in November 2001, 23 PMTs had failed outright. As stated in Chapter 6, failure along the signal path was found in eight of these and the rest had a failure in the high voltage path. Since startup, an additional 50 PMTs have been deactivated because of noise. Figure 8.1 shows the timeline for when these PMTs were deactivated. The simulation process described in Section 7.3.3 was repeated with these 73 PMTs removed to determine the muon tagging efficiency. The result, $98.8 \pm 0.3\%$, shows that the loss of these PMTs does not affect the ability of the Outer Detector to act as a veto. Table 8.1 lists the number and the reason for deactivation for each type of PMT, while Table 8.2 lists the number of deactivated PMTs for each region as of June 30, 2003.

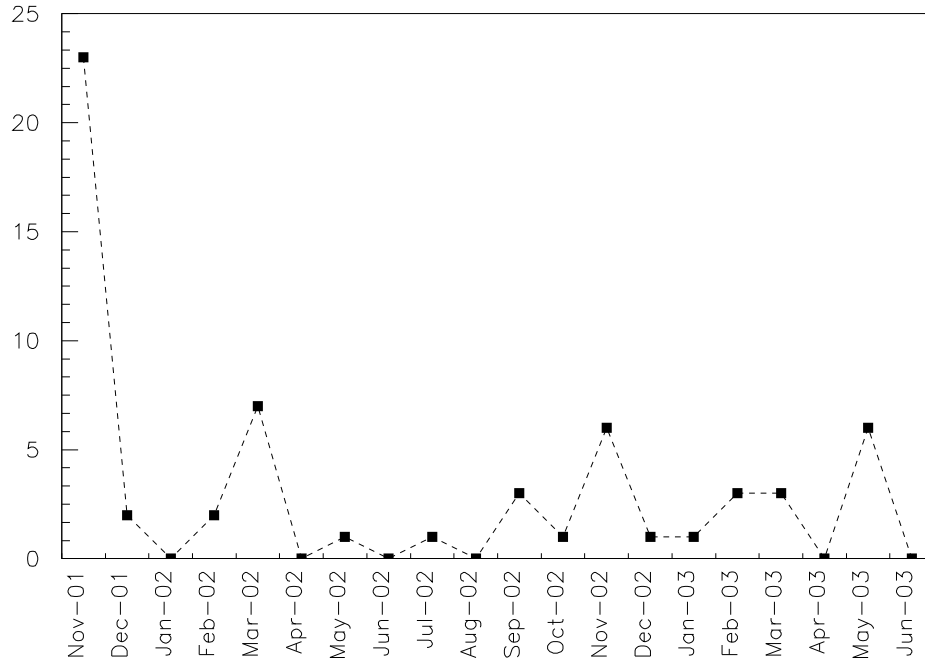


Figure 8.1: Histogram of deactivated PMTs over time. PMTs that were deactivated in November 2001 are those that failed during water filling of the Outer Detector. Thirteen PMTs are not shown due to unknown date of deactivation.

It is useful to determine the projected lifetime of the Outer Detector due to the deactivation of PMTs. Using Appendix D, the average rate of PMT loss in the Outer Detector was determined to be approximately 2.0 PMTs/month. At this rate, half of the Outer Detector PMTs are projected to have been deactivated 39 months after startup. Since KamLAND is slated to operate for three years in the reactor anti-neutrino phase and the simulations in Section 7.3.3 show that a significant decline in muon-tagging efficiency does not begin until after a 50% reduction in active PMTs, the deactivation of PMTs at this rate will not affect the ability of the Outer Detector to act as a veto.

As can be seen from Appendix D, deactivation of the Outer Detector PMTs has occurred in small groupings. This has often occurred during times of high trigger rates in the Outer Detector. Currently, the only way to find the culprit is to deactivate several

Table 8.1: Deactivated PMTs by type and reason as of June 30, 2003. PMTs that have are listed in the ‘outright failure’ row were deactivated in November 2001. Testing will need to be done to determine the reason. In addition, there are four PMTs of unknown type that have been deactivated.

| <i>Reason Deactivated</i> | <i># Deactivated</i> | | | | |
|-------------------------------|----------------------|----------|----------|-----------|------------|
| | <i>A</i> | <i>B</i> | <i>C</i> | <i>SK</i> | <i>Unk</i> |
| Outright Failure | 15 | 5 | 2 | 0 | 1 |
| Noisy/Flasher | 15 | 7 | 20 | 5 | 3 |
| Total | 30 | 12 | 22 | 5 | 4 |

Table 8.2: The number of deactivated PMTs by region as of June 30, 2003.

| <i>Region</i> | <i># Deactivated</i> |
|---------------|----------------------|
| Top | 9 |
| Upper | 15 |
| Lower | 20 |
| Bottom | 29 |

suspect PMTs. It has been noted that some of these deactivated PMTs may actually have been working properly and were not turned back on.

Using the ATWD waveforms, studies are underway to identify the deactivated PMTs and to search for the signature of a degenerating PMT. In this way, any wrongly deactivated PMTs can be restored to working order and a set of guidelines established to select the correct PMT for deactivation during periods of high trigger rates. It may also possible that some of the noisy/flasher PMTs can be brought back online, pending the results of these studies.

Chapter 9

Conclusions

On January 22, 2002, KamLAND officially began an experiment to measure the flux of anti-neutrinos produced by nuclear power reactors located in Japan. The first results were published based on 145.1 days of livetime data, showing a distinct difference between the number detected and the expected theoretical value for no oscillations. The ratio of observed versus expected was $0.611 \pm 0.085(\text{stat}) \pm 0.041(\text{syst})$ for anti-neutrino energies > 3.4 MeV. This result is inconsistent with the non-oscillation theory and excludes all but the Large Mixing Angle solution to the solar neutrino problem.

The Outer Detector played an integral part in the background suppression and it was important that its operating parameters were optimized. Before data taking commenced, several steps were taken to meet this goal. The twenty inch PMTs from the Kamiokande experiment were tested to determine their characteristics and their suitability to be used in KamLAND. Tyvek was used to segment the Outer Detector for better tracking of cosmic ray muons and to increase the collection of light. These efforts allow the muon detection efficiency to be as high as possible, even with the deactivation of PMTs.

During the startup period, trigger conditions were determined experimentally such that all muon-like events would be discriminated. Simulations were then used to verify that these settings produce a muon-tagging efficiency for the Outer Detector that exceeds 99%. Additional simulations have shown that the deactivation of PMTs in the Outer Detector

does not significantly affect its muon-tagging efficiency until more than half of the PMTs have been lost. It is projected that if the current deactivation rate of 2.0 PMTs per month holds, this will not happen until after the reactor anti-neutrino phase of the project has been completed. Since the efficiency declines as the number of deactivated PMTs increases, an eventual lowering of the NSUM threshold values may have to be considered to keep the tagging efficiency as high as possible.

In addition, simulations were performed to provide a check on the cited neutron background of less than 0.5 neutrons over the time period of 145.1 days. The final calculation using the simulation data produced a total neutron background of 1.3 ± 0.4 for this same time period. Thus, this background is shown to be small and does not affect KamLAND's results. The effectiveness of the Outer Detector in reducing the neutron background becomes critical when the muon-tagging efficiency approaches $94.8 \pm 0.1\%$. However, the Outer Detector should still be utilized since the neutron background increases to 29 ± 9 over 145.1 days if it is removed from operation.

Finally, continuing research is developing ways to determine the characteristics of a degenerating PMT based on studies of KamLAND data. These studies will enable the deactivation of the problem PMT only and not others that are operating properly. In addition, this data will allow the restoration of PMTs that are in working condition and previously deactivated.

Appendix A

PMT Test Results

86

Table A.1: Photomultiplier test results

| <i>Serial #</i> | <i>PMT Type</i> | κ | α | <i>HV at $G = 1 \times 10^7$</i> | \pm <i>HV for $\pm 5\%$ Gain</i> | <i>Ham. HV at $G = 0.6 \times 10^7$</i> | <i>Dark Current Rate (kHz)</i> | <i>Comments</i> |
|-----------------|-----------------|------------------------|----------|---|---|--|--------------------------------|--|
| 0006 | C | 2.32×10^{-20} | 8.1 | 1917 | 12 | 1787 | 7.3 | |
| 0019 | B | 1.65×10^{-18} | 7.6 | 1741 | 12 | 1618 | 7.0 | |
| 0021 | 17" | 5.94×10^{-12} | 5.4 | 2338 | 22 | 1942 | 7.0 | 17" ID tube |
| 0023 | B | 2.65×10^{-19} | 7.9 | 1691 | 11 | 1546 | 7.7 | |
| 0047 | B | 5.58×10^{-19} | 7.7 | 1992 | 13 | 1841 | 6.9 | |
| 0051 | B | 4.14×10^{-17} | 7.1 | 2045 | 15 | 2092 | 41.2 | 190V below Hamamatsu value |
| 0052 | B | 1.18×10^{-19} | 7.8 | 2211 | 15 | 2031 | 5.1 | |
| 0053 | C | 1.79×10^{-19} | 7.7 | 2135 | 14 | 1990 | 1.6 | only tested up to $G = 0.64 \times 10^7$ |
| 0056 | B | 1.20×10^{-18} | 7.4 | 2340 | 16 | 2116 | 8.0 | |

continued on next page

| <i>continued from previous page</i> | | | | | | | | |
|-------------------------------------|-----------------|------------------------|----------|---|------------------------------|--|--------------------------------|---|
| <i>Serial #</i> | <i>PMT Type</i> | κ | α | <i>HV at $G = 1 \times 10^7$</i> | $\pm 5\%$ <i>HV for Gain</i> | <i>Ham. HV at $G = 0.6 \times 10^7$</i> | <i>Dark Current Rate (kHz)</i> | <i>Comments</i> |
| 0058 | B | 1.31×10^{-18} | 7.5 | 2091 | 14 | 1904 | 5.5 | |
| 0059 | B | 2.33×10^{-19} | 7.7 | 2115 | 14 | 1911 | 5.2 | |
| 0063 | B | 4.75×10^{-20} | 8.0 | 1948 | 12 | 1801 | 5.6 | |
| 0064 | B | 5.44×10^{-19} | 7.6 | 2076 | 14 | 1892 | 10.0 | |
| 0067 | B | 3.70×10^{-18} | 7.3 | 2237 | 16 | 2085 | 0.6 | |
| 0069 | B | 3.98×10^{-19} | 7.6 | 2244 | 15 | 2086 | 6.5 | |
| 0071 | B | 4.43×10^{-19} | 7.6 | 2161 | 15 | 1968 | 5.3 | |
| 0076 | B | 8.43×10^{-19} | 7.6 | 1973 | 13 | 1812 | 5.8 | |
| 0083 | B | 6.36×10^{-19} | 7.6 | 2016 | 14 | 1876 | 7.3 | |
| 0084 | C | 5.75×10^{-20} | 8.0 | 1861 | 12 | 1790 | 2.5 | only tested up to $G = 0.84 \times 10^7$, 84V below Hamamatsu value |
| 0090 | B | 5.55×10^{-21} | 8.3 | 1952 | 12 | 1790 | 9.3 | |
| 0096 | B | 4.50×10^{-19} | 7.5 | 2317 | 16 | 2137 | 14.4 | |
| 0112 | B | 3.04×10^{-19} | 7.9 | 1747 | 11 | 1600 | 0.6 | |
| 0114 | B | 3.57×10^{-19} | 7.8 | 1791 | 12 | 1640 | 12.4 | |
| 0121 | B | 8.14×10^{-20} | 7.9 | 1942 | 13 | 1816 | 10.5 | |
| 0124 | B | 2.89×10^{-19} | 7.8 | 1834 | 12 | 1639 | 14.6 | |
| 0125 | UNK | 1.42×10^{-19} | 7.9 | 1864 | 12 | 1575 | 9.8 | hv may be lower (june tested) |
| 0127 | B | 1.33×10^{-18} | 7.5 | 2103 | 14 | 1940 | 7.2 | |
| 0128 | B | 8.76×10^{-19} | 7.7 | 1838 | 12 | 1706 | 7.2 | no signal on first test |
| 0131 | B | 8.38×10^{-20} | 8.0 | 1754 | 11 | 1608 | 18.5 | |
| 0133 | B | 5.22×10^{-20} | 8.1 | 1797 | 11 | 1630 | 7.3 | |
| 0137 | B | 1.49×10^{-20} | 8.3 | 1759 | 11 | 1615 | 8.6 | |
| 0164 | C | 1.16×10^{-20} | 8.1 | 2039 | 13 | 1849 | 6.0 | |
| <i>continued on next page</i> | | | | | | | | |

| <i>continued from previous page</i> | | | | | | | | |
|-------------------------------------|-----------------|------------------------|----------|---|------------------------------|--|--------------------------------|---|
| <i>Serial #</i> | <i>PMT Type</i> | κ | α | <i>HV at $G = 1 \times 10^7$</i> | $\pm 5\%$ <i>HV for Gain</i> | <i>Ham. HV at $G = 0.6 \times 10^7$</i> | <i>Dark Current Rate (kHz)</i> | <i>Comments</i> |
| 0165 | UNK | 9.72×10^{-21} | 8.1 | 2238 | 14 | 1883 | 9.6 | hv may be lower (june tested), 217V above Hamamatsu value |
| 0167 | C | 1.12×10^{-19} | 7.9 | 1892 | 12 | 1790 | 6.1 | |
| 0172 | C | 6.57×10^{-22} | 8.7 | 1709 | 10 | 1591 | 6.1 | |
| 0174 | C | 9.50×10^{-22} | 8.6 | 1871 | 11 | 1732 | 5.7 | new hv cable (old cable:MJJ) |
| 0175 | C | 3.01×10^{-21} | 8.4 | 1976 | 12 | 1856 | 10.9 | |
| 0180 | C | 2.89×10^{-20} | 8.0 | 2141 | 14 | 2023 | 6.3 | |
| 0185 | C | 1.11×10^{-21} | 8.5 | 1929 | 12 | 1800 | 18.4 | |
| 0188 | C | 1.34×10^{-20} | 8.0 | 2223 | 14 | 2096 | 6.5 | |
| 0189 | C | 1.25×10^{-19} | 8.0 | 1783 | 11 | 1643 | 4.8 | |
| 0193 | B | 1.61×10^{-18} | 7.4 | 2292 | 16 | 2085 | 19.6 | |
| 0210 | C | 1.56×10^{-21} | 8.4 | 2017 | 12 | 1878 | 9.3 | |
| 0213 | C | 7.90×10^{-19} | 7.5 | 2307 | 16 | 2170 | 6.4 | |
| 0214 | C | 1.73×10^{-21} | 8.4 | 1970 | 12 | 1841 | 7.8 | |
| 0226 | C | 1.12×10^{-18} | 7.5 | 2026 | 14 | 1904 | 12.0 | |
| 0233 | C | 1.01×10^{-20} | 8.3 | 1793 | 11 | 1676 | 7.1 | |
| 0238 | C | 3.46×10^{-20} | 8.3 | 1556 | 10 | 1438 | 12.6 | |
| 0240 | C | 2.75×10^{-20} | 8.1 | 1946 | 12 | 1775 | 10.1 | no hv on first test |
| 0241 | C | 3.13×10^{-19} | 7.7 | 2122 | 14 | 1940 | 11.7 | |
| 0243 | C | 8.41×10^{-20} | 8.1 | 1594 | 10 | 1501 | 4.9 | new hv cable (old cable:JJM), failed after installation replaced by #4595 |
| 0244 | A | 7.97×10^{-23} | 8.9 | 1938 | 11 | 1787 | 4.5 | failed after installation replaced by #3936 |
| 0245 | C | 8.24×10^{-18} | 7.2 | 2272 | 16 | 2108 | 4.8 | |

continued on next page

| <i>continued from previous page</i> | | | | | | | | |
|-------------------------------------|-----------------|------------------------|----------|---|---|--|--------------------------------|--|
| <i>Serial #</i> | <i>PMT Type</i> | κ | α | <i>HV at $G = 1 \times 10^7$</i> | \pm <i>HV for $\pm 5\%$ Gain</i> | <i>Ham. HV at $G = 0.6 \times 10^7$</i> | <i>Dark Current Rate (kHz)</i> | <i>Comments</i> |
| 0246 | C | 1.18×10^{-19} | 7.9 | 1929 | 12 | 1810 | 5.3 | |
| 0247 | C | 6.18×10^{-19} | 7.7 | 1919 | 13 | 1759 | 6.3 | signal cable frayed at PMT base |
| 0248 | A | 6.47×10^{-23} | 8.8 | 2047 | 12 | 1931 | 12.8 | |
| 0249 | C | 3.06×10^{-19} | 7.7 | 2018 | 13 | 1838 | 7.9 | |
| 0250 | C | 7.16×10^{-20} | 8.0 | 1798 | 11 | 1682 | 4.9 | failed after installation replaced by #3108 |
| 0254 | C | 6.60×10^{-21} | 8.3 | 1854 | 11 | 1725 | 11.0 | |
| 0255 | C | 5.97×10^{-21} | 8.2 | 2063 | 13 | 1902 | 7.7 | |
| 0256 | UNK | 1.22×10^{-20} | 8.1 | 2121 | 13 | 1836 | 20.1 | hv may be lower (june tested) |
| 0257 | C | 3.36×10^{-21} | 8.4 | 1897 | 12 | 1748 | 4.8 | |
| 0259 | C | 1.96×10^{-20} | 8.1 | 1957 | 12 | 1844 | 6.2 | |
| 0260 | C | 2.70×10^{-20} | 8.0 | 2177 | 14 | 2062 | 24.4 | |
| 0261 | C | 1.22×10^{-20} | 8.3 | 1745 | 11 | 1625 | 7.8 | |
| 0265 | C | 7.47×10^{-21} | 8.2 | 1945 | 12 | 1784 | 30.1 | |
| 0267 | C | 2.22×10^{-20} | 8.0 | 2120 | 14 | 1941 | 13.5 | |
| 0270 | C | 1.41×10^{-20} | 8.2 | 1923 | 12 | 1801 | 6.0 | |
| 0271 | C | 7.35×10^{-21} | 8.1 | 2149 | 13 | 1933 | 7.0 | |
| 0272 | C | 1.48×10^{-23} | 9.1 | 1921 | 11 | 1602 | 3.0 | only tested up to $G = 0.55 \times 10^7$, 214V above Hamamatsu value |
| 0273 | C | 1.18×10^{-21} | 8.7 | 1664 | 10 | 1551 | 6.4 | |
| 0274 | C | 1.74×10^{-21} | 8.5 | 1807 | 11 | 1682 | 6.9 | |
| 0275 | C | 1.31×10^{-19} | 7.8 | 2122 | 14 | 2012 | 10.8 | |
| 0276 | C | 9.78×10^{-20} | 7.8 | 2093 | 14 | 1909 | 3.0 | |
| 0283 | C | 3.06×10^{-20} | 7.9 | 2305 | 15 | 2137 | 7.0 | |
| 0287 | C | 5.34×10^{-20} | 8.0 | 1999 | 13 | 1827 | 5.4 | |

continued on next page

| <i>continued from previous page</i> | | | | | | | | |
|-------------------------------------|-----------------|------------------------|----------|---|------------------------------|--|--------------------------------|--|
| <i>Serial #</i> | <i>PMT Type</i> | κ | α | <i>HV at $G = 1 \times 10^7$</i> | $\pm 5\%$ <i>HV for Gain</i> | <i>Ham. HV at $G = 0.6 \times 10^7$</i> | <i>Dark Current Rate (kHz)</i> | <i>Comments</i> |
| 0289 | C | 2.68×10^{-20} | 8.0 | 2091 | 13 | 1893 | 6.3 | |
| 0290 | C | 6.33×10^{-22} | 8.6 | 1973 | 12 | 1841 | 8.5 | |
| 0292 | C | 1.41×10^{-19} | 7.8 | 1988 | 13 | 1856 | 7.5 | |
| 0293 | C | 3.46×10^{-20} | 7.9 | 2305 | 15 | 2123 | 5.4 | |
| 0294 | C | 1.54×10^{-21} | 8.4 | 1959 | 12 | 1849 | 5.8 | new hv cable (old cable:MD) |
| 0295 | C | 2.08×10^{-20} | 8.0 | 2129 | 14 | 1978 | 5.0 | |
| 0299 | C | 3.37×10^{-21} | 8.3 | 2038 | 13 | 1872 | 5.3 | failed after installation replaced by #3335 |
| 0304 | C | 1.06×10^{-20} | 8.1 | 2138 | 13 | 2032 | 5.9 | |
| 0314 | B | 1.79×10^{-19} | 7.9 | 1869 | 12 | | 7.9 | |
| 0357 | C | 1.08×10^{-26} | 10.3 | 1564 | 8 | 1453 | 6.9 | failed after installation replaced by #0701 |
| 0372 | C | 1.01×10^{-24} | 9.7 | 1531 | 8 | 1413 | 8.2 | |
| 0373 | C | 1.58×10^{-25} | 10.0 | 1557 | 8 | 1440 | 7.8 | no signal on first test |
| 0374 | C | 8.05×10^{-27} | 10.3 | 1646 | 8 | 1539 | 16.4 | |
| 0377 | C | 1.78×10^{-25} | 9.9 | 1623 | 8 | 1490 | 7.1 | |
| 0701 | B | 9.85×10^{-20} | 7.7 | 2484 | 17 | 2338 | 8.3 | only tested up to $G = 0.91 \times 10^7$ replaces #0357 |
| 0707 | B | 2.16×10^{-19} | 7.9 | 1847 | 12 | 1707 | 12.8 | |
| 0757 | C | 2.65×10^{-20} | 7.9 | 2375 | 15 | 2260 | 2.7 | only tested up to $G = 0.7 \times 10^7$ |
| 2034 | UNK | 1.92×10^{-21} | 8.2 | 2516 | 16 | 2187 | 9.6 | hv may be lower (june tested) |
| 2037 | A | 1.50×10^{-24} | 9.5 | 1713 | 9 | 1573 | 5.5 | |
| 2041 | A | 6.31×10^{-24} | 9.2 | 1854 | 10 | 1747 | 6.1 | |
| 3039 | B | 3.39×10^{-23} | 8.8 | 2288 | 13 | 2146 | 0.7 | |
| 3051 | A | 6.42×10^{-24} | 9.2 | 1898 | 11 | 1759 | 10.4 | replaces #3330 |

continued on next page

| <i>continued from previous page</i> | | | | | | | | |
|-------------------------------------|-----------------|------------------------|----------|-------------------------------------|--|--|--|-------------------------|
| <i>Serial #</i> | <i>PMT Type</i> | κ | α | <i>HV at</i> $G = 1 \times 10^7$ | \pm <i>HV for</i> $\pm 5\%$ <i>Gain</i> | <i>Ham. HV at</i> $G = 0.6 \times 10^7$ | <i>Dark Current</i> <i>Rate (kHz)</i> | <i>Comments</i> |
| 3058 | B | 4.40×10^{-22} | 8.5 | 2121 | 13 | 1945 | 28.5 | |
| 3089 | B | 3.72×10^{-23} | 9.1 | 1785 | 10 | 1638 | 4.3 | |
| 3091 | B | 2.38×10^{-23} | 9.2 | 1688 | 9 | 1584 | 12.5 | |
| 3099 | B | 8.56×10^{-24} | 9.1 | 1935 | 11 | 1728 | 25.8 | |
| 3108 | B | 8.80×10^{-23} | 8.8 | 2051 | 12 | 1897 | 45.2 | replaces #0250 |
| 3115 | A | 1.91×10^{-22} | 8.7 | 2072 | 12 | 1856 | 3.8 | |
| 3138 | A | 2.68×10^{-22} | 8.7 | 1950 | 11 | 1800 | 4.8 | |
| 3139 | A | 8.35×10^{-21} | 8.0 | 2329 | 15 | 2076 | 4.0 | no signal on first test |
| 3144 | A | 1.18×10^{-21} | 8.3 | 2287 | 14 | 2169 | 7.9 | |
| 3146 | A | 2.16×10^{-20} | 8.0 | 2168 | 14 | 2058 | 34.2 | |
| 3151 | A | 1.27×10^{-23} | 9.2 | 1741 | 10 | 1636 | 4.3 | |
| 3174 | A | 1.63×10^{-22} | 8.8 | 1800 | 10 | 1673 | 4.5 | |
| 3181 | A | 3.58×10^{-27} | 10.2 | 1917 | 10 | 1747 | 25.8 | |
| 3188 | A | 6.70×10^{-25} | 9.5 | 1940 | 10 | 1756 | 4.2 | |
| 3192 | A | 7.14×10^{-22} | 8.4 | 2192 | 13 | 2045 | 3.5 | |
| 3205 | A | 1.46×10^{-20} | 8.0 | 2202 | 14 | 2091 | 4.7 | |
| 3211 | A | 1.60×10^{-22} | 8.7 | 2022 | 12 | 1817 | 6.9 | |
| 3226 | A | 1.49×10^{-18} | 7.7 | 1748 | 12 | 1636 | 7.2 | |
| 3240 | A | 2.19×10^{-26} | 10.1 | 1702 | 9 | 1592 | 4.0 | |
| 3255 | A | 1.15×10^{-20} | 8.3 | 1803 | 11 | 1677 | 6.4 | |
| 3259 | A | 3.42×10^{-27} | 10.4 | 1654 | 8 | 1545 | 4.5 | |
| 3267 | A | 2.85×10^{-25} | 9.8 | 1642 | 9 | 1545 | 4.2 | |
| 3270 | A | 1.33×10^{-23} | 9.2 | 1785 | 10 | 1644 | 6.2 | |
| 3273 | A | 6.87×10^{-23} | 8.8 | 2018 | 12 | 1946 | 4.6 | |
| 3292 | A | 7.67×10^{-23} | 8.9 | 1935 | 11 | 1815 | 3.8 | |

continued on next page

| <i>continued from previous page</i> | | | | | | | | |
|-------------------------------------|-----------------|------------------------|----------|---|------------------------------|--|--------------------------------|--|
| <i>Serial #</i> | <i>PMT Type</i> | κ | α | <i>HV at $G = 1 \times 10^7$</i> | $\pm 5\%$ <i>HV for Gain</i> | <i>Ham. HV at $G = 0.6 \times 10^7$</i> | <i>Dark Current Rate (kHz)</i> | <i>Comments</i> |
| 3294 | A | 1.68×10^{-23} | 9.0 | 1988 | 11 | 1843 | 5.7 | |
| 3297 | A | 3.35×10^{-25} | 9.7 | 1751 | 9 | 1621 | 4.6 | |
| 3308 | A | 1.74×10^{-24} | 9.5 | 1752 | 9 | 1800 | 16.7 | 140V below Hamamatsu value |
| 3312 | A | 1.27×10^{-23} | 9.1 | 1946 | 11 | 1787 | 18.6 | |
| 3314 | A | 2.66×10^{-22} | 8.6 | 2043 | 12 | 1933 | 2.5 | |
| 3316 | A | 1.85×10^{-22} | 8.6 | 2138 | 13 | 1995 | 5.3 | |
| 3321 | A | 2.44×10^{-17} | 7.1 | 2095 | 15 | 1934 | 6.7 | |
| 3330 | A | 1.08×10^{-23} | 9.2 | 1859 | 10 | 1786 | 7.0 | failed after installation replaced by #3051 |
| 3334 | A | 1.21×10^{-21} | 8.4 | 2042 | 12 | 1959 | 6.5 | |
| 3335 | A | 4.51×10^{-22} | 8.4 | 2355 | 14 | 1699 | 5.0 | 517V above Hamamatsu value, replaces #0299, failed after installation, replaced by #4649 |
| 3361 | A | 5.54×10^{-27} | 10.3 | 1710 | 9 | 1623 | 6.0 | |
| 3363 | A | 1.42×10^{-25} | 9.9 | 1682 | 9 | 1572 | 3.7 | |
| 3387 | A | 2.44×10^{-25} | 9.8 | 1738 | 9 | 1630 | 8.1 | |
| 3400 | A | 1.67×10^{-24} | 9.5 | 1721 | 9 | 1605 | 6.9 | |
| 3424 | A | 2.69×10^{-26} | 10.1 | 1723 | 9 | 1620 | 6.5 | |
| 3427 | A | 5.06×10^{-28} | 10.4 | 2001 | 10 | 1902 | 8.5 | |
| 3428 | A | 2.88×10^{-24} | 9.4 | 1730 | 9 | 1679 | 13.0 | |
| 3429 | A | 5.65×10^{-26} | 10.0 | 1726 | 9 | 1630 | 8.8 | |
| 3431 | A | 4.43×10^{-25} | 9.6 | 1868 | 10 | 1719 | 8.0 | |
| 3432 | A | 2.81×10^{-25} | 9.6 | 1890 | 10 | 1798 | 42.2 | |
| 3462 | A | 4.70×10^{-24} | 9.2 | 1917 | 11 | 1782 | 4.8 | |
| 3466 | A | 1.98×10^{-24} | 9.4 | 1787 | 10 | 1684 | 4.3 | |

continued on next page

| <i>continued from previous page</i> | | | | | | | | |
|-------------------------------------|-----------------|------------------------|----------|---|---|--|--------------------------------|--|
| <i>Serial #</i> | <i>PMT Type</i> | κ | α | <i>HV at $G = 1 \times 10^7$</i> | \pm <i>HV for $\pm 5\%$ Gain</i> | <i>Ham. HV at $G = 0.6 \times 10^7$</i> | <i>Dark Current Rate (kHz)</i> | <i>Comments</i> |
| 3492 | A | 5.73×10^{-23} | 8.8 | 2054 | 12 | 1959 | 4.5 | |
| 3514 | A | 6.16×10^{-24} | 9.2 | 1962 | 11 | 1839 | 42.9 | failed after installation replaced by #5362 |
| 3516 | A | 4.81×10^{-22} | 8.5 | 2062 | 12 | 1921 | 3.9 | |
| 3519 | A | 6.31×10^{-25} | 9.6 | 1816 | 10 | 1756 | 7.8 | hv not crimped originally |
| 3537 | A | 2.63×10^{-24} | 9.3 | 1883 | 10 | 1750 | 4.4 | |
| 3540 | B | 4.57×10^{-23} | 9.0 | 1774 | 10 | 1718 | 12.0 | |
| 3558 | A | 4.30×10^{-26} | 9.9 | 1886 | 10 | 1862 | 6.0 | 71V below Hamamatsu value |
| 3562 | A | 2.48×10^{-24} | 9.3 | 1887 | 10 | 1718 | 4.6 | |
| 3579 | A | 6.83×10^{-24} | 9.2 | 1926 | 11 | 1797 | 15.5 | |
| 3633 | UNK | 8.38×10^{-23} | 8.8 | 2049 | 12 | 1801 | 15.6 | hv may be lower (june tested) replaces #5362 |
| 3637 | A | 1.22×10^{-25} | 9.9 | 1639 | 8 | 1551 | 7.1 | |
| 3641 | B | 1.25×10^{-23} | 9.2 | 1748 | 10 | 1665 | 14.8 | |
| 3653 | A | 3.14×10^{-17} | 7.2 | 1927 | 14 | 1786 | 4.7 | |
| 3685 | A | 8.85×10^{-24} | 9.1 | 1929 | 11 | 1768 | 12.8 | |
| 3688 | A | 7.23×10^{-24} | 9.2 | 1817 | 10 | 1718 | 5.7 | |
| 3692 | A | 1.95×10^{-25} | 9.8 | 1680 | 9 | 1600 | 9.8 | |
| 3693 | A | 4.76×10^{-24} | 9.3 | 1895 | 10 | 1750 | 7.2 | |
| 3721 | A | 5.94×10^{-26} | 9.9 | 1844 | 10 | 1723 | 6.9 | |
| 3745 | A | 1.34×10^{-22} | 8.7 | 2020 | 12 | 1889 | 31.8 | |
| 3755 | A | 3.69×10^{-24} | 9.2 | 1970 | 11 | 1827 | 4.5 | |
| 3793 | A | 6.26×10^{-21} | 8.3 | 1846 | 11 | 1749 | 4.6 | |
| 3799 | A | 1.10×10^{-27} | 10.4 | 1856 | 9 | 1722 | 22.7 | |
| 3808 | UNK | 5.18×10^{-25} | 9.6 | 1867 | 10 | 1650 | 5.9 | hv may be lower (june tested) |

continued on next page

| <i>continued from previous page</i> | | | | | | | | |
|-------------------------------------|-----------------|------------------------|----------|---|---|--|--------------------------------|---|
| <i>Serial #</i> | <i>PMT Type</i> | κ | α | <i>HV at $G = 1 \times 10^7$</i> | \pm <i>HV for $\pm 5\%$ Gain</i> | <i>Ham. HV at $G = 0.6 \times 10^7$</i> | <i>Dark Current Rate (kHz)</i> | <i>Comments</i> |
| 3843 | A | 1.94×10^{-25} | 9.7 | 1798 | 9 | 1684 | 10.1 | |
| 3855 | A | 8.87×10^{-27} | 10.3 | 1664 | 8 | 1576 | 4.1 | |
| 3863 | A | 3.17×10^{-27} | 10.4 | 1607 | 8 | 1512 | 26.2 | |
| 3872 | A | 7.11×10^{-27} | 10.3 | 1606 | 8 | 1516 | 7.4 | |
| 3886 | A | 8.18×10^{-26} | 9.8 | 1920 | 10 | 1830 | 15.6 | |
| 3929 | A | 9.13×10^{-25} | 9.4 | 1981 | 11 | 1830 | 15.5 | |
| 3936 | A | 4.12×10^{-24} | 9.4 | 1697 | 9 | 1599 | 43.6 | replaces #0244 |
| 3937 | A | 7.46×10^{-27} | 10.2 | 1745 | 9 | 1630 | 16.7 | |
| 3938 | A | 8.28×10^{-29} | 10.6 | 2087 | 10 | 1589 | 0.2 | only tested up to $G = 0.58 \times 10^7$, graph turns over, replaces #4740, 400V above Hamamatsu value |
| 3952 | A | 2.83×10^{-23} | 8.9 | 2066 | 12 | 1913 | 5.5 | |
| 3966 | A | 3.44×10^{-25} | 9.7 | 1780 | 9 | 1604 | 0.0 | |
| 3978 | A | 6.64×10^{-24} | 9.4 | 1644 | 9 | 1546 | 8.1 | hv not crimped originally |
| 3984 | A | 3.64×10^{-27} | 10.2 | 1869 | 9 | 1773 | 9.9 | |
| 3988 | A | 2.44×10^{-28} | 10.7 | 1713 | 8 | 1593 | 8.3 | |
| 3995 | A | 1.59×10^{-27} | 10.4 | 1762 | 9 | 1687 | 5.5 | |
| 4001 | A | 1.26×10^{-23} | 9.2 | 1844 | 10 | 1742 | 12.3 | |
| 4035 | A | 2.73×10^{-22} | 8.5 | 2203 | 13 | 2007 | 8.3 | |
| 4053 | A | 3.04×10^{-25} | 9.8 | 1621 | 8 | 1511 | 10.1 | |
| 4055 | A | 6.73×10^{-24} | 9.5 | 1514 | 8 | 1431 | 15.3 | |
| 4061 | A | 8.88×10^{-25} | 9.5 | 1882 | 10 | 1783 | 33.5 | |
| 4089 | A | 2.55×10^{-21} | 8.4 | 1916 | 12 | 1782 | 3.6 | |
| 4111 | B | 1.77×10^{-25} | 9.7 | 1949 | 10 | 1826 | 6.9 | |
| 4138 | A | 3.58×10^{-26} | 10.1 | 1581 | 8 | 1476 | 11.5 | |

continued on next page

| <i>continued from previous page</i> | | | | | | | | |
|-------------------------------------|-----------------|------------------------|----------|---|---|--|--------------------------------|---------------------------|
| <i>Serial #</i> | <i>PMT Type</i> | κ | α | <i>HV at $G = 1 \times 10^7$</i> | \pm <i>HV for $\pm 5\%$ Gain</i> | <i>Ham. HV at $G = 0.6 \times 10^7$</i> | <i>Dark Current Rate (kHz)</i> | <i>Comments</i> |
| 4154 | A | 1.34×10^{-25} | 9.9 | 1661 | 9 | 1581 | 7.5 | |
| 4188 | A | 1.13×10^{-24} | 9.2 | 2333 | 13 | 2161 | 10.5 | |
| 4231 | A | 4.89×10^{-26} | 10.0 | 1673 | 9 | 1573 | 5.6 | |
| 4234 | A | 1.78×10^{-23} | 9.2 | 1672 | 9 | 1582 | 9.0 | |
| 4267 | A | 1.11×10^{-25} | 9.9 | 1688 | 9 | 1594 | 10.3 | |
| 4290 | A | 1.23×10^{-21} | 8.7 | 1615 | 9 | 1502 | 7.1 | |
| 4293 | A | 1.69×10^{-24} | 9.5 | 1731 | 9 | 1613 | 5.9 | |
| 4305 | A | 1.88×10^{-24} | 9.4 | 1797 | 10 | 1665 | 6.7 | |
| 4310 | A | 1.17×10^{-22} | 8.7 | 2133 | 13 | 2004 | 4.5 | |
| 4312 | A | 8.45×10^{-23} | 8.9 | 1909 | 11 | 1814 | 6.8 | |
| 4333 | A | 1.02×10^{-26} | 10.1 | 1866 | 9 | 1870 | 12.5 | 96V below Hamamatsu value |
| 4399 | A | 1.43×10^{-23} | 9.2 | 1790 | 10 | 1653 | 10.6 | |
| 4405 | A | 1.52×10^{-25} | 9.7 | 1955 | 10 | 1777 | 4.1 | |
| 4415 | A | 1.26×10^{-24} | 9.6 | 1711 | 9 | 1634 | 6.5 | hv not crimped originally |
| 4424 | A | 2.41×10^{-23} | 9.1 | 1814 | 10 | 1696 | 5.7 | |
| 4428 | A | 4.09×10^{-23} | 9.0 | 1808 | 10 | 1718 | 7.9 | |
| 4445 | A | 1.14×10^{-24} | 9.6 | 1683 | 9 | 1610 | 5.9 | no hv on first test |
| 4451 | A | 2.26×10^{-25} | 9.5 | 2117 | 11 | 2004 | 7.1 | |
| 4453 | A | 9.88×10^{-25} | 9.7 | 1604 | 8 | 1522 | 18.2 | |
| 4466 | A | 8.13×10^{-23} | 8.7 | 2232 | 13 | 2063 | 4.9 | |
| 4496 | A | 4.31×10^{-26} | 9.9 | 1814 | 9 | 1731 | 43.0 | |
| 4521 | A | 4.02×10^{-24} | 9.4 | 1758 | 10 | 1630 | 13.2 | |
| 4531 | A | 6.36×10^{-23} | 9.0 | 1725 | 10 | 1599 | 6.6 | |
| 4545 | A | 2.68×10^{-23} | 9.0 | 1904 | 11 | 1815 | 5.8 | |
| 4548 | A | 4.76×10^{-25} | 9.7 | 1715 | 9 | 1626 | 6.6 | |

continued on next page

| <i>continued from previous page</i> | | | | | | | | |
|-------------------------------------|-----------------|------------------------|----------|---|---|--|--------------------------------|--|
| <i>Serial #</i> | <i>PMT Type</i> | κ | α | <i>HV at $G = 1 \times 10^7$</i> | \pm <i>HV for $\pm 5\%$ Gain</i> | <i>Ham. HV at $G = 0.6 \times 10^7$</i> | <i>Dark Current Rate (kHz)</i> | <i>Comments</i> |
| 4568 | B | 3.04×10^{-27} | 10.5 | 1548 | 8 | 1480 | 7.1 | |
| 4573 | B | 1.27×10^{-27} | 10.7 | 1483 | 7 | 1416 | 11.2 | |
| 4578 | A | 2.70×10^{-24} | 9.4 | 1836 | 10 | 1759 | 13.1 | |
| 4586 | UNK | 2.21×10^{-25} | 9.8 | 1683 | 9 | 1483 | 10.0 | hv may be lower (june tested) |
| 4591 | B | 5.97×10^{-26} | 10.1 | 1585 | 8 | 1483 | 5.7 | |
| 4595 | B | 7.16×10^{-27} | 10.4 | 1524 | 7 | 1426 | 48.5 | replaces #0243 |
| 4610 | B | 1.81×10^{-22} | 8.8 | 1841 | 11 | 1741 | 9.9 | |
| 4618 | B | 6.19×10^{-30} | 11.1 | 1838 | 8 | 1764 | 10.9 | |
| 4628 | B | 5.31×10^{-26} | 10.0 | 1732 | 9 | 1665 | 5.5 | |
| 4636 | A | 3.67×10^{-24} | 9.4 | 1727 | 9 | 1571 | 5.2 | |
| 4637 | B | 2.10×10^{-26} | 10.2 | 1594 | 8 | 1352 | 6.4 | |
| 4640 | B | 2.52×10^{-28} | 10.9 | 1542 | 7 | 1470 | 9.6 | |
| 4644 | B | 2.66×10^{-25} | 9.7 | 1743 | 9 | 1620 | 7.0 | no signal on first test |
| 4649 | UNK | 9.28×10^{-26} | 10.0 | 1650 | 8 | 1453 | 9.2 | hv may be lower (june tested), replaces #3335 |
| 4652 | B | 2.74×10^{-28} | 10.8 | 1559 | 7 | 1500 | 20.0 | |
| 4679 | B | 1.32×10^{-22} | 8.9 | 1804 | 10 | 1741 | 10.9 | |
| 4735 | A | 2.66×10^{-24} | 9.5 | 1593 | 9 | 1476 | 6.9 | |
| 4740 | B | 2.58×10^{-25} | 9.7 | 1787 | 9 | 1698 | 9.4 | failed after installation replaced by #3938 |
| 4765 | A | 1.21×10^{-22} | 8.8 | 1979 | 12 | 1805 | 4.2 | |
| 4780 | A | 7.87×10^{-26} | 10.1 | 1485 | 8 | 2049 | 6.6 | 637V below Hamamatsu value |
| 4789 | B | 5.91×10^{-22} | 8.6 | 1869 | 11 | 1814 | 6.3 | |
| 4791 | B | 9.69×10^{-24} | 9.3 | 1702 | 9 | 1612 | 9.6 | |
| 4807 | B | 1.16×10^{-22} | 8.6 | 2338 | 14 | 2032 | 4.6 | |

continued on next page

| <i>continued from previous page</i> | | | | | | | | |
|-------------------------------------|-----------------|------------------------|----------|---|------------------------------|--|--------------------------------|--|
| <i>Serial #</i> | <i>PMT Type</i> | κ | α | <i>HV at $G = 1 \times 10^7$</i> | $\pm 5\%$ <i>HV for Gain</i> | <i>Ham. HV at $G = 0.6 \times 10^7$</i> | <i>Dark Current Rate (kHz)</i> | <i>Comments</i> |
| 4808 | B | 1.55×10^{-23} | 9.2 | 1802 | 10 | 1741 | 11.6 | |
| 4814 | A | 1.42×10^{-21} | 8.2 | 2534 | 16 | 2248 | 10.1 | only tested up to $G = 0.88 \times 10^7$ |
| 4815 | A | 2.79×10^{-23} | 9.0 | 1941 | 11 | 1815 | 5.4 | |
| 4816 | UNK | 2.02×10^{-21} | 8.2 | 2290 | 14 | 2013 | 8.0 | hv may be lower (june tested) |
| 4820 | B | 3.37×10^{-24} | 9.3 | 1825 | 10 | 1754 | 5.8 | no hv on first test |
| 4827 | A | 6.76×10^{-22} | 8.6 | 1911 | 11 | 1797 | 15.2 | |
| 4829 | B | 1.18×10^{-26} | 10.3 | 1601 | 8 | 1533 | 6.0 | |
| 4833 | B | 8.46×10^{-25} | 9.6 | 1737 | 9 | 1638 | 5.0 | |
| 4842 | B | 4.62×10^{-24} | 9.4 | 1634 | 9 | 1603 | 12.8 | |
| 4845 | B | 1.20×10^{-27} | 10.4 | 1771 | 9 | 1676 | 19.1 | |
| 4849 | B | 5.40×10^{-25} | 9.5 | 1905 | 10 | 1788 | 0.9 | |
| 4858 | A | 7.47×10^{-22} | 8.4 | 2312 | 14 | 2120 | 5.2 | |
| 4866 | B | 7.64×10^{-27} | 10.2 | 1717 | 9 | 1657 | 6.2 | |
| 4867 | B | 1.66×10^{-24} | 9.3 | 2036 | 11 | 1840 | 4.8 | |
| 4868 | A | 2.12×10^{-27} | 10.3 | 1838 | 9 | 1705 | 8.3 | |
| 4869 | B | 2.44×10^{-27} | 10.3 | 1822 | 9 | 1708 | 6.6 | |
| 5168 | SK | 6.57×10^{-20} | 7.9 | 1985 | 13 | | 38.0 | |
| 5258 | SK | 7.11×10^{-23} | 8.9 | 1958 | 11 | | 14.1 | hv may be lower (june tested) |
| 5326 | SK | 1.91×10^{-20} | 8.2 | 1862 | 12 | | 11.3 | |
| 5362 | SK | 1.59×10^{-19} | 7.8 | 1977 | 13 | | 113.6 | replaces #3514, failed after installation, replaced by #3633 |
| 5372 | SK | 5.97×10^{-20} | 8.0 | 1834 | 12 | | 15.2 | |
| 5374 | SK | 2.40×10^{-21} | 8.4 | 1940 | 12 | | 65.2 | hv may be lower (june tested) |
| 5412 | SK | 5.00×10^{-20} | 8.0 | 1887 | 12 | | 45.0 | no signal on first test |
| 5574 | SK | 8.83×10^{-21} | 8.3 | 1832 | 11 | | 28.9 | |

continued on next page

| <i>continued from previous page</i> | | | | | | | | |
|-------------------------------------|-----------------|------------------------|----------|---|---|--|--------------------------------|-----------------|
| <i>Serial #</i> | <i>PMT Type</i> | κ | α | <i>HV at $G = 1 \times 10^7$</i> | \pm <i>HV for $\pm 5\%$ Gain</i> | <i>Ham. HV at $G = 0.6 \times 10^7$</i> | <i>Dark Current Rate (kHz)</i> | <i>Comments</i> |
| 6839 | SK | 1.69×10^{-20} | 8.1 | 2085 | 13 | | 6.5 | |
| 6860 | SK | 5.31×10^{-27} | 8.0 | 2005 | 13 | | 6.1 | |
| 6862 | SK | 1.09×10^{-20} | 8.2 | 1995 | 12 | | 6.9 | |
| 6864 | SK | 2.91×10^{-20} | 8.1 | 1920 | 12 | | 13.3 | |
| 6865 | SK | 1.18×10^{-27} | 8.2 | 1933 | 12 | | 12.7 | |
| 6873 | SK | 1.74×10^{-21} | 8.4 | 1937 | 12 | | 63.0 | |
| 7078 | SK | 2.13×10^{-20} | 7.9 | 2273 | 15 | | 6.6 | |

Appendix B

PMT Positions

III

Table B.1: Installed PMT locations

| <i>Position</i> | <i>Serial #</i> | <i>PMT Type</i> | <i>Signal Label</i> | <i>HV Label</i> | <i>HV for G = 1×10^7</i> | <i>Dark Current Rate (kHz)</i> | <i>Comments</i> |
|-------------------------------|-----------------|-----------------|---------------------|-----------------|--|--------------------------------|--------------------------------------|
| T-1-13 | 3205 | A | AI | RQ | 2202 | 4.7 | |
| T-1-31 | 4578 | A | AE | RR | 1836 | 13.1 | |
| T-1-49 | 0133 | B | AD | QD | 1797 | 7.3 | |
| T-1-67 | 4640 | B | AC | QE | 1542 | 9.6 | |
| T-1-85 | 4827 | A | CH | RT | 1911 | 15.2 | |
| T-1-103 | 0175 | C | GP | QM | 1976 | 10.9 | |
| T-1-121 | 0125 | UNK | GR | QN | 1864 | 9.8 | actual hv may be lower (june tested) |
| T-1-139 | 0248 | A | IG | QT | 2047 | 12.8 | |
| T-1-157 | 0023 | B | GW | QQ | 1691 | 7.7 | |
| <i>continued on next page</i> | | | | | | | |

| <i>continued from previous page</i> | | | | | | | |
|-------------------------------------|-----------------|-----------------|---------------------|-----------------|--|--------------------------------|--|
| <i>Position</i> | <i>Serial #</i> | <i>PMT Type</i> | <i>Signal Label</i> | <i>HV Label</i> | <i>HV for G = 1 × 10⁷</i> | <i>Dark Current Rate (kHz)</i> | <i>Comments</i> |
| T-1-175 | 0272 | C | IJ | UA | 1921 | 3.0 | only tested up to $G = 0.55 \times 10^7$ 214V above Hamamatsu value |
| T-1-193 | 4035 | A | GG | UC | 2203 | 8.3 | |
| T-1-211 | 2041 | A | GS | UI | 1854 | 6.1 | |
| T-1-229 | 4637 | B | AB | RN | 1594 | 6.4 | |
| T-1-247 | 3516 | A | EG | SA | 2062 | 3.9 | |
| T-1-265 | 4866 | B | EP | SD | 1717 | 6.2 | |
| T-1-283 | 3312 | A | EL | RY | 1946 | 18.6 | |
| T-1-301 | 3937 | A | BL | RV | 1745 | 16.7 | |
| T-1-319 | 3091 | B | BJ | QA | 1688 | 12.5 | |
| T-1-337 | 3966 | A | BF | SE | 1780 | 0.0 | |
| T-1-355 | 4833 | B | BG | RJ | 1737 | 5.0 | |
| T-2-13 | 0377 | C | AH | QI | 1623 | 7.1 | |
| T-2-31 | 3872 | A | AG | RO | 1606 | 7.4 | |
| T-2-49 | 3139 | A | AA | QG | 2329 | 4.0 | no signal on first test 00/12/15 |
| T-2-67 | 4636 | A | AB | QJ | 1727 | 5.2 | |
| T-2-85 | 4815 | A | CG | RS | 1941 | 5.4 | |
| T-2-103 | 4290 | A | GQ | UB | 1615 | 7.1 | |
| T-2-121 | 0292 | C | GX | QO | 1988 | 7.5 | |
| T-2-139 | 0121 | B | IH | QS | 1942 | 10.5 | |
| T-2-157 | 0193 | B | GV | QP | 2292 | 19.6 | |
| T-2-175 | 3693 | A | GI | TK | 1895 | 7.2 | |
| T-2-193 | 3039 | B | GF | TM | 2288 | 0.7 | |
| T-2-211 | 3363 | A | GT | QW | 1682 | 3.7 | |
| T-2-229 | 3988 | A | AT | RM | 1713 | 8.3 | |

continued on next page

| <i>continued from previous page</i> | | | | | | | |
|-------------------------------------|-----------------|-----------------|---------------------|-----------------|--|--------------------------------|--------------------------------------|
| <i>Position</i> | <i>Serial #</i> | <i>PMT Type</i> | <i>Signal Label</i> | <i>HV Label</i> | <i>HV for G = 1 × 10⁷</i> | <i>Dark Current Rate (kHz)</i> | <i>Comments</i> |
| T-2-247 | 3808 | UNK | EH | SB | 1867 | 5.9 | actual hv may be lower (june tested) |
| T-2-265 | 4807 | B | EM | SC | 2338 | 4.6 | |
| T-2-283 | 3361 | A | EO | RW | 1710 | 6.0 | |
| T-2-301 | 3641 | B | BK | RU | 1748 | 14.8 | |
| T-2-319 | 3099 | B | BI | QB | 1935 | 25.8 | |
| T-2-337 | 4628 | B | BH | TB | 1732 | 5.5 | |
| T-2-355 | 3688 | A | FV | RK | 1817 | 5.7 | |
| T-3-31 | 0090 | B | AF | RP | 1952 | 9.3 | |
| T-3-67 | 0226 | C | GK | QH | 2026 | 12.0 | |
| T-3-103 | 4573 | B | IK | UG | 1483 | 11.2 | |
| T-3-139 | 0059 | B | II | TZ | 2115 | 5.2 | |
| T-3-175 | 3466 | A | GH | TJ | 1787 | 4.3 | |
| T-3-211 | 2037 | A | GU | QV | 1713 | 5.5 | |
| T-3-247 | 3429 | A | EI | RZ | 1726 | 8.8 | |
| T-3-283 | 4610 | B | BM | RX | 1841 | 9.9 | |
| T-3-319 | 4001 | A | BE | QC | 1844 | 12.3 | |
| T-3-355 | 0210 | C | GC | RI | 2017 | 9.3 | |
| S-1-9 | 0293 | C | FJ | RE | 2305 | 5.4 | |
| S-1-27 | 0240 | C | FM | RA | 1946 | 10.1 | no hv on first test 00/12/15 |
| S-1-45 | 4820 | B | GJ | TI | 1825 | 5.8 | no hv on first test 00/12/15 |
| S-1-63 | 3297 | A | IC | TG | 1751 | 4.6 | |
| S-1-81 | 3151 | A | IM | TE | 1741 | 4.3 | |
| S-1-99 | 3428 | A | EA | SX | 1730 | 13.0 | |
| S-1-117 | 4428 | A | DT | SS | 1808 | 7.9 | |
| S-1-135 | 0114 | B | DN | SV | 1791 | 12.4 | |
| <i>continued on next page</i> | | | | | | | |

| <i>continued from previous page</i> | | | | | | | |
|-------------------------------------|-----------------|-----------------|---------------------|-----------------|--|--------------------------------|----------------------------------|
| <i>Position</i> | <i>Serial #</i> | <i>PMT Type</i> | <i>Signal Label</i> | <i>HV Label</i> | <i>HV for G = 1 × 10⁷</i> | <i>Dark Current Rate (kHz)</i> | <i>Comments</i> |
| S-1-153 | 0128 | B | DB | TU | 1838 | 7.2 | no signal on first test 00/12/15 |
| S-1-171 | 4618 | B | DD | SR | 1838 | 10.9 | |
| S-1-189 | 3334 | A | AU | TQ | 2042 | 6.5 | |
| S-1-207 | 4869 | B | BB | TP | 1822 | 6.6 | |
| S-1-225 | 3745 | A | FH | UF | 2020 | 31.8 | |
| S-1-243 | 3637 | A | HW | UH | 1639 | 7.1 | |
| S-1-261 | 4305 | A | HN | SQ | 1797 | 6.7 | |
| S-1-279 | 4521 | A | HS | SN | 1758 | 13.2 | |
| S-1-297 | 3259 | A | HH | SJ | 1654 | 4.5 | |
| S-1-315 | 0273 | C | FW | SH | 1664 | 6.4 | |
| S-1-333 | 0241 | C | FU | UU | 2122 | 11.7 | |
| S-1-351 | 3255 | A | FF | RG | 1803 | 6.4 | |
| S-2-9 | 0064 | B | FT | RD | 2076 | 10.0 | |
| S-2-27 | 0052 | B | GE | RB | 2211 | 5.1 | |
| S-2-45 | 3174 | A | GL | QY | 1800 | 4.5 | |
| S-2-63 | 3799 | A | ID | TF | 1856 | 22.7 | |
| S-2-81 | 3755 | A | IL | TC | 1970 | 4.5 | |
| S-2-99 | 4867 | B | DZ | SZ | 2036 | 4.8 | |
| S-2-117 | 0069 | B | DP | TA | 2244 | 6.5 | |
| S-2-135 | 4496 | A | DV | SU | 1814 | 43.0 | |
| S-2-153 | 0276 | C | DA | TW | 2093 | 3.0 | |
| S-2-171 | 4451 | A | DE | TX | 2117 | 7.1 | |
| S-2-189 | 3540 | B | AW | TS | 1774 | 12.0 | |
| S-2-207 | 3321 | A | BD | TO | 2095 | 6.7 | |
| S-2-225 | 0047 | B | FZ | TN | 1992 | 6.9 | |

continued on next page

| <i>continued from previous page</i> | | | | | | | |
|-------------------------------------|-----------------|-----------------|---------------------|-----------------|--|--------------------------------|--|
| <i>Position</i> | <i>Serial #</i> | <i>PMT Type</i> | <i>Signal Label</i> | <i>HV Label</i> | <i>HV for G = 1 × 10⁷</i> | <i>Dark Current Rate (kHz)</i> | <i>Comments</i> |
| S-2-243 | 0112 | B | HE | UD | 1747 | 0.6 | |
| S-2-261 | 3051 | A | HQ | SP | 1898 | 10.4 | REPLACES #3330 |
| S-2-261 | 3330 | A | HQ | SP | 1859 | 7.0 | FAILED AFTER INSTALLATION REPLACED BY #3051 |
| S-2-279 | 0083 | B | HR | SO | 2016 | 7.3 | |
| S-2-297 | 4111 | B | HO | SI | 1949 | 6.9 | |
| S-2-315 | 4405 | A | HK | SG | 1955 | 4.1 | |
| S-2-333 | 3144 | A | IB | UP | 2287 | 7.9 | |
| S-2-351 | 0271 | C | FY | RH | 2149 | 7.0 | |
| S-3-9 | 0245 | C | FS | RF | 2272 | 4.8 | |
| S-3-27 | 3240 | A | GD | RC | 1702 | 4.0 | |
| S-3-45 | 3692 | A | GM | QZ | 1680 | 9.8 | |
| S-3-63 | 3294 | A | IE | TH | 1988 | 5.7 | |
| S-3-81 | 0096 | B | IN | TD | 2317 | 14.4 | |
| S-3-99 | 3424 | A | DW | SY | 1723 | 6.5 | |
| S-3-117 | 0058 | B | DQ | SW | 2091 | 5.5 | |
| S-3-135 | 0213 | C | DO | ST | 2307 | 6.4 | |
| S-3-153 | 4858 | A | DJ | TV | 2312 | 5.2 | |
| S-3-171 | 3089 | B | DF | QR | 1785 | 4.3 | |
| S-3-189 | 3181 | A | AV | TR | 1917 | 25.8 | |
| S-3-207 | 0067 | B | AZ | TT | 2237 | 0.6 | |
| S-3-225 | 3653 | A | AS | QK | 1927 | 4.7 | |
| S-3-243 | 0127 | B | HF | UE | 2103 | 7.2 | |
| S-3-261 | 4789 | B | HD | QU | 1869 | 6.3 | |
| S-3-279 | 3146 | A | HP | SM | 2168 | 34.2 | |

continued on next page

| <i>continued from previous page</i> | | | | | | | |
|-------------------------------------|-----------------|-----------------|---------------------|-----------------|--|--------------------------------|----------------------------------|
| <i>Position</i> | <i>Serial #</i> | <i>PMT Type</i> | <i>Signal Label</i> | <i>HV Label</i> | <i>HV for G = 1 × 10⁷</i> | <i>Dark Current Rate (kHz)</i> | <i>Comments</i> |
| S-3-297 | 0076 | B | HV | SK | 1973 | 5.8 | |
| S-3-315 | 4568 | B | HJ | SF | 1548 | 7.1 | |
| S-3-333 | 0131 | B | IA | UM | 1754 | 18.5 | |
| S-3-351 | 4644 | B | FG | QX | 1743 | 7.0 | no signal on first test 00/12/15 |
| S-4-9 | 0707 | B | FR | OH | 1847 | 12.8 | |
| S-4-27 | 0019 | B | FK | OF | 1741 | 7.0 | |
| S-4-45 | 4845 | B | FP | OW | 1771 | 19.1 | |
| S-4-63 | 4333 | A | IF | OY | 1866 | 12.5 | 96V below Hamamatsu value |
| S-4-81 | 3843 | A | IO | PC | 1798 | 10.1 | |
| S-4-99 | 3995 | A | DU | OC | 1762 | 5.5 | |
| S-4-117 | 3314 | A | DM | OD | 2043 | 2.5 | |
| S-4-135 | 4591 | B | DK | NW | 1585 | 5.7 | |
| S-4-153 | 3226 | A | CX | NZ | 1748 | 7.2 | |
| S-4-171 | 3270 | A | DH | NJ | 1785 | 6.2 | |
| S-4-189 | 4445 | A | AY | NE | 1683 | 5.9 | no hv on first test 00/12/15 |
| S-4-207 | 4415 | A | BA | NB | 1711 | 6.5 | no hv crimp originally 00/12/15 |
| S-4-225 | 4399 | A | AQ | PE | 1790 | 10.6 | |
| S-4-243 | 4679 | B | HG | PG | 1804 | 10.9 | |
| S-4-261 | 4453 | A | HC | NO | 1604 | 18.2 | |
| S-4-279 | 4089 | A | HB | NM | 1916 | 3.6 | |
| S-4-297 | 3929 | A | GY | PA | 1981 | 15.5 | |
| S-4-315 | 3855 | A | HZ | OT | 1664 | 4.1 | |
| S-4-333 | 4791 | B | HL | NT | 1702 | 9.6 | |
| S-4-351 | 0124 | B | GA | NQ | 1834 | 14.6 | |
| S-5-9 | 3492 | A | FO | OK | 2054 | 4.5 | |
| <i>continued on next page</i> | | | | | | | |

| <i>continued from previous page</i> | | | | | | | |
|-------------------------------------|-----------------|-----------------|---------------------|-----------------|--|--------------------------------|---|
| <i>Position</i> | <i>Serial #</i> | <i>PMT Type</i> | <i>Signal Label</i> | <i>HV Label</i> | <i>HV for $G = 1 \times 10^7$</i> | <i>Dark Current Rate (kHz)</i> | <i>Comments</i> |
| S-5-27 | 3188 | A | FL | OG | 1940 | 4.2 | |
| S-5-45 | 3863 | A | FQ | OX | 1607 | 26.2 | |
| S-5-63 | 3558 | A | GN | OZ | 1886 | 6.0 | 71V below Hamamatsu value |
| S-5-81 | 4548 | A | IQ | OM | 1715 | 6.6 | |
| S-5-99 | 3462 | A | DL | OB | 1917 | 4.8 | |
| S-5-117 | 4545 | A | DR | OE | 1904 | 5.8 | |
| S-5-135 | 4808 | B | DS | NG | 1802 | 11.6 | |
| S-5-153 | 0071 | B | CZ | NX | 2161 | 5.3 | |
| S-5-171 | 3400 | A | DG | NY | 1721 | 6.9 | |
| S-5-189 | 3978 | A | AX | NA | 1644 | 8.1 | no hv crimp originally 00/12/15 |
| S-5-207 | 3519 | A | BC | NC | 1816 | 7.8 | hv not crimped originally 00/12/15 |
| S-5-225 | 4740 | B | AP | PD | 1787 | 9.4 | FAILED AFTER INSTALLATION REPLACED BY #3938 |
| S-5-225 | 3938 | A | BO | VF | 2087 | 0.2 | only tested up to $G = 0.58 \times 10^7$, graph turns over, REPLACES #4740, 400V above Hamamatsu value |
| S-5-243 | 3793 | A | HX | PF | 1846 | 4.6 | |
| S-5-261 | 4424 | A | EN | NP | 1814 | 5.7 | |
| S-5-279 | 4829 | B | HA | NN | 1601 | 6.0 | |
| S-5-297 | 4735 | A | GZ | PB | 1593 | 6.9 | |
| S-5-315 | 4531 | A | HI | OS | 1725 | 6.6 | |
| S-5-333 | 4849 | B | HM | NU | 1905 | 0.9 | |
| S-5-351 | 4842 | B | FI | NR | 1634 | 12.8 | |
| S-6-9 | 5412 | SK | | | 1887 | 45.0 | no signal on first test 0/12/15 |
| S-6-27 | 0373 | C | FN | OV | 1557 | 7.8 | no signal on first test 0/12/15 |

continued on next page

| <i>continued from previous page</i> | | | | | | | |
|-------------------------------------|-----------------|-----------------|---------------------|-----------------|--|--------------------------------|--|
| <i>Position</i> | <i>Serial #</i> | <i>PMT Type</i> | <i>Signal Label</i> | <i>HV Label</i> | <i>HV for G = 1 × 10⁷</i> | <i>Dark Current Rate (kHz)</i> | <i>Comments</i> |
| S-6-45 | 6864 | SK | | | 1920 | 13.3 | |
| S-6-63 | 0372 | C | GO | OO | 1531 | 8.2 | |
| S-6-81 | 0053 | C | IP | ON | 2135 | 1.6 | only tested up to $G = 0.64 \times 10^7$ |
| S-6-99 | 0287 | C | DY | OA | 1999 | 5.4 | |
| S-6-117 | 5168 | SK | | | 1985 | 38.0 | |
| S-6-135 | 0757 | C | DX | NH | 2375 | 2.7 | only tested up to $G = 0.7 \times 10^7$ |
| S-6-153 | 3211 | A | CY | NV | 2022 | 6.9 | |
| S-6-171 | 0180 | C | DI | NI | 2141 | 6.3 | |
| S-6-189 | 6860 | SK | | | 2005 | 6.1 | |
| S-6-207 | 0214 | C | DC | ND | 1970 | 7.8 | |
| S-6-225 | 6873 | SK | | | 1937 | 63.0 | |
| S-6-243 | 0246 | C | HY | NF | 1929 | 5.3 | |
| S-6-261 | 7078 | SK | | | 2273 | 6.6 | |
| S-6-279 | 0283 | C | HD | OU | 2305 | 7.0 | |
| S-6-297 | 3721 | A | HT | OP | 1844 | 6.9 | |
| S-6-315 | 0274 | C | FX | OR | 1807 | 6.9 | |
| S-6-333 | 6862 | SK | | | 1995 | 6.9 | |
| S-6-351 | 0357 | C | GB | NS | 1564 | 6.9 | FAILED AFTER INSTALLATION REPLACED BY #0701 |
| S-6-351 | 0701 | B | GB | NS | 2484 | 8.3 | only tested up to $G = 0.91 \times 10^7$ REPLACES #0357 |
| B-1-9 | 4293 | A | EK | KB | 1731 | 5.9 | |
| B-1-27 | 3952 | A | EX | KA | 2066 | 5.5 | |
| B-1-45 | 0261 | C | EY | JJJ | 1745 | 7.8 | |
| B-1-63 | 3273 | A | EU | LP | 2018 | 4.6 | |
| <i>continued on next page</i> | | | | | | | |

| <i>continued from previous page</i> | | | | | | | |
|-------------------------------------|-----------------|-----------------|---------------------|-----------------|--|--------------------------------|--|
| <i>Position</i> | <i>Serial #</i> | <i>PMT Type</i> | <i>Signal Label</i> | <i>HV Label</i> | <i>HV for G = 1 × 10⁷</i> | <i>Dark Current Rate (kHz)</i> | <i>Comments</i> |
| B-1-81 | 0270 | C | ES | KX | 1923 | 6.0 | |
| B-1-99 | 0294 | C | CE | VD | 1959 | 5.8 | hv trips - use new hv cable (old cable:MD) 00/12/15 |
| B-1-117 | 0295 | C | IZ | LX | 2129 | 5.0 | |
| B-1-135 | 0289 | C | IS | LW | 2091 | 6.3 | |
| B-1-153 | 0250 | C | BW | LQ | 1798 | 4.9 | FAILED AFTER INSTALLATION REPLACED BY #3108 |
| B-1-153 | 3108 | B | BW | LQ | 2051 | 45.2 | REPLACES #0250 |
| B-1-171 | 0174 | C | BY | VB | 1871 | 5.7 | hv trips - use new hv cable (old cable:MJJ) 00/12/15 |
| B-1-189 | 0188 | C | EZ | KW | 2223 | 6.5 | |
| B-1-207 | 0084 | C | JA | KP | 1861 | 2.5 | only tested up to $G = 0.84 \times 10^7$, 84V below Hamamatsu value |
| B-1-225 | 0260 | C | IX | LM | 2177 | 24.4 | |
| B-1-243 | 0255 | C | CW | KF | 2063 | 7.7 | |
| B-1-261 | 0299 | C | AJ | KL | 2038 | 5.3 | FAILED AFTER INSTALLATION REPLACED BY #3335 |
| B-1-261 | 3335 | A | AJ | KL | 2355 | 5.0 | 517V above Hamamatsu value, REPLACES #0299, FAILED AFTER INSTALLATION, REPLACED BY #4649 |
| B-1-261 | 4649 | UNK | AJ | KL | 1650 | 9.2 | actual hv may be lower (june tested), REPLACES #3335 |
| B-1-279 | 0265 | C | CC | LG | 1945 | 30.1 | |
| B-1-297 | 6865 | SK | EE | KD | 1933 | 12.7 | |
| B-1-315 | 3514 | A | CD | MJ | 1962 | 42.9 | FAILED AFTER INSTALLATION REPLACED BY #5362 |
| <i>continued on next page</i> | | | | | | | |

| <i>continued from previous page</i> | | | | | | | |
|-------------------------------------|-----------------|-----------------|---------------------|-----------------|--|--------------------------------|--|
| <i>Position</i> | <i>Serial #</i> | <i>PMT Type</i> | <i>Signal Label</i> | <i>HV Label</i> | <i>HV for G = 1 × 10⁷</i> | <i>Dark Current Rate (kHz)</i> | <i>Comments</i> |
| B-1-315 | 5362 | SK | CD | MJ | 1977 | 113.6 | REPLACES #3514, FAILED AFTER INSTALLATION, REPLACED BY #3633 |
| B-1-315 | 3633 | UNK | CI | KV | 2049 | 15.6 | actual hv may be lower (june tested), REPLACES #5362 |
| B-1-333 | 0063 | B | BZ | KR | 1948 | 5.6 | |
| B-1-351 | 3267 | A | CV | MA | 1642 | 4.2 | |
| B-2-9 | 3984 | A | AN | KG | 1869 | 9.9 | |
| B-2-27 | 0275 | C | BT | KH | 2122 | 10.8 | |
| B-2-45 | 3292 | A | EQ | MF | 1935 | 3.8 | |
| B-2-63 | 0256 | UNK | BV | LN | 2121 | 20.1 | actual hv may be lower (june tested) |
| B-2-81 | 0254 | C | FD | LO | 1854 | 11.0 | |
| B-2-99 | 0238 | C | CA | KI | 1556 | 12.6 | |
| B-2-117 | 3115 | A | CF | LL | 2072 | 3.8 | |
| B-2-135 | 3192 | A | IV | KC | 2192 | 3.5 | |
| B-2-153 | 4586 | UNK | FA | LA | 1683 | 10.0 | actual hv may be lower (june tested) |
| B-2-171 | 0290 | C | BU | KM | 1973 | 8.5 | |
| B-2-189 | 0267 | C | EV | LB | 2120 | 13.5 | |
| B-2-207 | 0006 | C | JB | KJ | 1917 | 7.3 | |
| B-2-225 | 0304 | C | IR | LH | 2138 | 5.9 | |
| B-2-243 | 0189 | C | BS | LY | 1783 | 4.8 | |
| B-2-261 | 4154 | A | AO | LT | 1661 | 7.5 | |
| B-2-279 | 4652 | B | AK | LS | 1559 | 20.0 | |
| B-2-297 | 0374 | C | ED | LE | 1646 | 16.4 | |
| B-2-315 | 0247 | C | CB | LR | 1919 | 6.3 | signal cable is frayed at PMT base 00/12/15 |
| B-2-333 | 0249 | C | EF | LU | 2018 | 7.9 | |

continued on next page

| <i>continued from previous page</i> | | | | | | | |
|-------------------------------------|-----------------|-----------------|---------------------|-----------------|--|--------------------------------|---|
| <i>Position</i> | <i>Serial #</i> | <i>PMT Type</i> | <i>Signal Label</i> | <i>HV Label</i> | <i>HV for G = 1 × 10⁷</i> | <i>Dark Current Rate (kHz)</i> | <i>Comments</i> |
| B-2-351 | 3431 | A | AL | MB | 1868 | 8.0 | |
| B-3-27 | 3886 | A | FB | ME | 1920 | 15.6 | |
| B-3-63 | 0257 | C | ET | KS | 1897 | 4.8 | |
| B-3-99 | 0243 | C | FC | VG | 1594 | 4.9 | hv trips - use new hv cable (old cable:JJM) 00/12/15, FAILED AFTER INSTALLATION REPLACED BY #4595 |
| B-3-99 | 4595 | B | FC | VG | 1524 | 48.5 | REPLACES #0243 |
| B-3-135 | 0172 | C | IY | KE | 1709 | 6.1 | |
| B-3-171 | 0137 | B | FE | KU | 1759 | 8.6 | |
| B-3-207 | 0185 | C | IT | KK | 1929 | 18.4 | |
| B-3-243 | 0244 | A | EB | KQ | 1938 | 4.5 | FAILED AFTER INSTALLATION REPLACED BY #3936 |
| B-3-243 | 3936 | A | EB | KQ | 1697 | 43.6 | REPLACES #0244 |
| B-3-279 | 0233 | C | AM | LC | 1793 | 7.1 | |
| B-3-315 | 5258 | SK | EJ | MM | 1958 | 14.1 | actual hv may be lower (june tested) |
| B-3-351 | 0165 | UNK | EC | LZ | 2238 | 9.6 | actual hv may be lower (june tested), 217V above Hamamatsu value |
| B-4-63 | 4814 | A | EW | MC | 2534 | 10.1 | only tested up to $G = 0.88 \times 10^7$ |
| B-4-135 | 5326 | SK | IU | LK | 1862 | 11.3 | |
| B-4-207 | 6839 | SK | IW | LV | 2085 | 6.5 | |
| B-4-279 | 0259 | C | BX | LD | 1957 | 6.2 | |
| B-4-351 | 5374 | SK | ER | LF | 1940 | 65.2 | actual hv may be lower (june tested) |

Appendix C

Board and Channel Locations

Table C.1: Electronics and high voltage board and channel listings. A – indicates that a PMT has been disconnected from a particular board and channel.

| <i>Serial #</i> | <i>Position</i> | <i>Electronics Board #</i> | <i>Electronics Channel #</i> | <i>High Voltage Board #</i> | <i>High Voltage Channel #</i> | <i>Comments</i> |
|-----------------|-----------------|--------------------------------|----------------------------------|---------------------------------|-----------------------------------|-----------------|
| 0006 | B-2-207 | – | – | 6 | 14 | Deactivated |
| 0019 | S-4-27 | 16 | 6 | 10 | 7 | Deactivated |
| 0023 | T-1-157 | 2 | 6 | 11 | 15 | |
| 0047 | S-2-225 | 9 | 4 | 4 | 5 | |
| 0052 | S-2-27 | 11 | 7 | 1 | 2 | |
| 0053 | S-6-81 | 12 | 5 | 1 | 8 | |
| 0058 | S-3-117 | 7 | 11 | 2 | 2 | Deactivated |
| 0059 | T-3-139 | 2 | 10 | 2 | 10 | |
| 0063 | B-1-333 | 19 | 9 | 5 | 9 | |
| 0064 | S-2-9 | 11 | 4 | 2 | 8 | |
| 0067 | S-3-207 | 9 | 2 | 0 | 2 | Deactivated |
| 0069 | S-2-117 | 7 | 10 | 0 | 0 | |
| 0071 | S-5-153 | 13 | 4 | 1 | 15 | Deactivated |
| 0076 | S-3-297 | 10 | 5 | 4 | 9 | |
| 0083 | S-2-279 | 10 | 1 | 3 | 8 | Deactivated |
| 0084 | B-1-207 | – | – | – | – | Deactivated |
| 0090 | T-3-31 | 4 | 4 | 4 | 10 | |
| 0096 | S-3-81 | 7 | 5 | 0 | 10 | |
| 0112 | S-2-243 | 9 | 7 | 10 | 4 | |
| 0114 | S-1-135 | 8 | 0 | 9 | 9 | |

continued on next page

| <i>continued from previous page</i> | | | | | | |
|-------------------------------------|-----------------|--------------------------------|----------------------------------|---------------------------------|-----------------------------------|-----------------|
| <i>Serial #</i> | <i>Position</i> | <i>Electronics Board #</i> | <i>Electronics Channel #</i> | <i>High Voltage Board #</i> | <i>High Voltage Channel #</i> | <i>Comments</i> |
| 0121 | T-2-139 | 2 | 9 | 5 | 10 | |
| 0124 | S-4-351 | 16 | 0 | 8 | 8 | |
| 0125 | T-1-121 | 3 | 0 | 7 | 4 | |
| 0127 | S-3-243 | 9 | 8 | 2 | 3 | |
| 0128 | S-1-153 | 8 | 3 | 8 | 15 | Deactivated |
| 0131 | S-3-333 | 10 | 11 | 10 | 10 | |
| 0133 | T-1-49 | 4 | 0 | 9 | 6 | |
| 0137 | B-3-171 | 18 | 8 | 10 | 11 | |
| 0165 | B-3-351 | 18 | 1 | 0 | 11 | Deactivated |
| 0172 | B-3-135 | 18 | 2 | 11 | 13 | Deactivated |
| 0174 | B-1-171 | 18 | 6 | 7 | 5 | Deactivated |
| 0175 | T-1-103 | 3 | 2 | 4 | 4 | |
| 0180 | S-6-171 | 13 | 8 | 1 | 14 | |
| 0185 | B-3-207 | – | – | 5 | 13 | Deactivated |
| 0188 | B-1-189 | 18 | 9 | 1 | 7 | Deactivated |
| 0189 | B-2-243 | 17 | 4 | 9 | 2 | |
| 0193 | T-2-157 | 2 | 7 | 0 | 15 | |
| 0210 | T-3-355 | 4 | 10 | 3 | 10 | Deactivated |
| 0213 | S-3-135 | 8 | 2 | 0 | 13 | |
| 0214 | S-6-207 | 14 | 2 | 4 | 11 | Deactivated |
| 0226 | T-3-67 | 3 | 10 | 3 | 2 | |
| 0233 | B-3-279 | 19 | 2 | 9 | 11 | |
| 0238 | B-2-99 | 17 | 7 | 13 | 13 | |
| 0240 | S-1-27 | 11 | 6 | 5 | 6 | |
| 0241 | S-1-333 | 10 | 9 | 1 | 3 | |
| 0245 | S-3-9 | 11 | 5 | 0 | 6 | Deactivated |
| 0246 | S-6-243 | 14 | 8 | 5 | 5 | |
| 0247 | B-2-315 | 20 | 7 | 6 | 3 | Deactivated |
| 0248 | T-1-139 | 2 | 8 | 3 | 14 | |
| 0249 | B-2-333 | 19 | 10 | 3 | 12 | |
| 0254 | B-2-81 | 17 | 5 | 7 | 12 | |
| 0255 | B-1-243 | – | – | 2 | 7 | Deactivated |
| 0256 | B-2-63 | 17 | 1 | 1 | 6 | Deactivated |
| 0257 | B-3-63 | 17 | 2 | 6 | 11 | |
| 0259 | B-4-279 | 19 | 3 | 4 | 15 | Deactivated |
| 0260 | B-1-225 | 19 | 4 | 1 | 11 | |
| 0261 | B-1-45 | 21 | 9 | 10 | 13 | Deactivated |

continued on next page

| <i>continued from previous page</i> | | | | | | |
|-------------------------------------|-----------------|--------------------------------|----------------------------------|---------------------------------|-----------------------------------|-----------------|
| <i>Serial #</i> | <i>Position</i> | <i>Electronics Board #</i> | <i>Electronics Channel #</i> | <i>High Voltage Board #</i> | <i>High Voltage Channel #</i> | <i>Comments</i> |
| 0265 | B-1-279 | 19 | 0 | 5 | 11 | |
| 0267 | B-2-189 | 18 | 10 | 2 | 11 | |
| 0270 | B-1-81 | – | – | 6 | 12 | Deactivated |
| 0271 | S-2-351 | 11 | 1 | 1 | 1 | Deactivated |
| 0272 | T-1-175 | 2 | 2 | 6 | 9 | Deactivated |
| 0273 | S-1-315 | 10 | 6 | 12 | 6 | |
| 0274 | S-6-315 | 15 | 8 | 8 | 2 | |
| 0275 | B-2-27 | – | – | 1 | 13 | Deactivated |
| 0276 | S-2-153 | 8 | 4 | 2 | 15 | |
| 0283 | S-6-279 | 15 | 2 | 0 | 1 | Deactivated |
| 0287 | S-6-99 | 12 | 8 | 3 | 5 | Deactivated |
| 0289 | B-1-135 | – | – | – | – | Deactivated |
| 0290 | B-2-171 | – | – | 4 | 13 | Deactivated |
| 0292 | T-2-121 | 3 | 1 | 4 | 1 | |
| 0293 | S-1-9 | 11 | 3 | 0 | 7 | |
| 0294 | B-1-99 | 17 | 6 | 4 | 3 | Deactivated |
| 0295 | B-1-117 | 17 | 9 | 1 | 10 | |
| 0304 | B-2-225 | 17 | 3 | 1 | 12 | |
| 0372 | S-6-63 | 12 | 2 | 13 | 11 | |
| 0373 | S-6-27 | 16 | 8 | 13 | 8 | |
| 0374 | B-2-297 | 19 | 5 | 12 | 11 | |
| 0377 | T-2-13 | 4 | 7 | 12 | 12 | |
| 0701 | S-6-351 | 16 | 2 | 14 | 14 | |
| 0707 | S-4-9 | 16 | 3 | 7 | 11 | |
| 0757 | S-6-135 | 13 | 2 | 0 | 12 | |
| 2037 | T-3-211 | 6 | 10 | 11 | 9 | |
| 2041 | T-1-211 | 6 | 8 | 7 | 9 | |
| 3039 | T-2-193 | 2 | 1 | 0 | 9 | Deactivated |
| 3051 | S-2-261 | 9 | 10 | 6 | 4 | |
| 3089 | S-3-171 | 8 | 8 | 9 | 14 | |
| 3091 | T-1-319 | 5 | 2 | 12 | 4 | |
| 3099 | T-2-319 | 5 | 3 | 5 | 3 | |
| 3108 | B-1-153 | – | – | – | – | Deactivated |
| 3115 | B-2-117 | 17 | 10 | 2 | 12 | |
| 3139 | T-2-49 | 4 | 1 | 0 | 8 | Deactivated |
| 3144 | S-2-333 | 10 | 10 | 0 | 5 | |
| 3146 | S-3-279 | 10 | 2 | 1 | 0 | Deactivated |

continued on next page

| <i>continued from previous page</i> | | | | | | |
|-------------------------------------|-----------------|--------------------------------|----------------------------------|---------------------------------|-----------------------------------|-----------------|
| <i>Serial #</i> | <i>Position</i> | <i>Electronics Board #</i> | <i>Electronics Channel #</i> | <i>High Voltage Board #</i> | <i>High Voltage Channel #</i> | <i>Comments</i> |
| 3151 | S-1-81 | 7 | 3 | 10 | 12 | |
| 3174 | S-2-45 | 11 | 10 | 9 | 5 | |
| 3181 | S-3-189 | 8 | 11 | 3 | 0 | Deactivated |
| 3188 | S-5-27 | 16 | 7 | 5 | 7 | Deactivated |
| 3192 | B-2-135 | – | – | 1 | 9 | Deactivated |
| 3205 | T-1-13 | 4 | 6 | 1 | 4 | |
| 3211 | S-6-153 | 13 | 5 | 3 | 15 | Deactivated |
| 3226 | S-4-153 | 13 | 3 | 10 | 15 | |
| 3240 | S-3-27 | 11 | 8 | 11 | 7 | |
| 3255 | S-1-351 | 11 | 0 | 8 | 6 | Deactivated |
| 3259 | S-1-297 | 10 | 3 | 12 | 7 | |
| 3267 | B-1-351 | – | – | – | – | Deactivated |
| 3270 | S-4-171 | 13 | 6 | 9 | 15 | |
| 3273 | B-1-63 | 17 | 0 | – | – | Deactivated |
| 3292 | B-2-45 | 18 | 11 | 5 | 14 | |
| 3294 | S-3-63 | 7 | 2 | 4 | 0 | |
| 3297 | S-1-63 | 7 | 0 | 11 | 0 | |
| 3312 | T-1-283 | 5 | 8 | 5 | 4 | |
| 3314 | S-4-117 | 12 | 9 | 3 | 3 | Deactivated |
| 3321 | S-2-207 | 9 | 1 | 2 | 6 | Deactivated |
| 3334 | S-1-189 | 8 | 9 | 3 | 1 | |
| 3361 | T-2-283 | 5 | 9 | 11 | 5 | Deactivated |
| 3363 | T-2-211 | 6 | 9 | 12 | 10 | |
| 3400 | S-5-171 | 13 | 7 | 11 | 14 | |
| 3424 | S-3-99 | 7 | 8 | 11 | 2 | |
| 3428 | S-1-99 | 7 | 6 | 10 | 0 | |
| 3429 | T-3-247 | 6 | 4 | 11 | 6 | |
| 3431 | B-2-351 | 18 | 0 | 7 | 15 | |
| 3462 | S-5-99 | 12 | 7 | 6 | 1 | |
| 3466 | T-3-175 | 2 | 4 | 9 | 8 | |
| 3492 | S-5-9 | 16 | 4 | 2 | 9 | |
| 3516 | T-1-247 | 6 | 2 | 2 | 4 | Deactivated |
| 3519 | S-5-207 | 14 | 1 | – | – | Deactivated |
| 3540 | S-2-189 | 8 | 10 | 8 | 0 | Deactivated |
| 3558 | S-5-63 | 12 | 1 | 7 | 1 | |
| 3633 | B-1-315 | 19 | 6 | 3 | 11 | |
| 3637 | S-1-243 | 9 | 6 | 12 | 8 | Deactivated |

continued on next page

| <i>continued from previous page</i> | | | | | | |
|-------------------------------------|-----------------|--------------------------------|----------------------------------|---------------------------------|-----------------------------------|-----------------|
| <i>Serial #</i> | <i>Position</i> | <i>Electronics Board #</i> | <i>Electronics Channel #</i> | <i>High Voltage Board #</i> | <i>High Voltage Channel #</i> | <i>Comments</i> |
| 3641 | T-2-301 | 5 | 7 | 10 | 2 | |
| 3653 | S-3-225 | 9 | 5 | 5 | 1 | Deactivated |
| 3688 | T-2-355 | 4 | 9 | 8 | 7 | |
| 3692 | S-3-45 | 11 | 11 | 12 | 13 | |
| 3693 | T-2-175 | 2 | 3 | 6 | 10 | |
| 3721 | S-6-297 | 15 | 5 | 8 | 3 | Deactivated |
| 3745 | S-1-225 | 9 | 3 | 3 | 7 | |
| 3755 | S-2-81 | 7 | 4 | 4 | 14 | |
| 3793 | S-5-243 | 14 | 7 | 7 | 7 | |
| 3799 | S-2-63 | 7 | 1 | 7 | 3 | |
| 3808 | T-2-247 | 6 | 3 | 7 | 8 | |
| 3843 | S-4-81 | 12 | 3 | 9 | 10 | |
| 3855 | S-4-315 | 15 | 6 | 12 | 5 | |
| 3863 | S-5-45 | 16 | 10 | 13 | 10 | |
| 3872 | T-2-31 | 4 | 3 | 13 | 7 | |
| 3886 | B-3-27 | 21 | 8 | – | – | Deactivated |
| 3929 | S-4-297 | 15 | 3 | 4 | 8 | |
| 3936 | B-3-243 | 19 | 8 | – | – | Deactivated |
| 3937 | T-1-301 | 5 | 6 | 10 | 1 | |
| 3938 | S-5-225 | 14 | 4 | 2 | 5 | Deactivated |
| 3952 | B-1-27 | 18 | 7 | 2 | 13 | |
| 3966 | T-1-337 | 5 | 0 | 9 | 4 | |
| 3978 | S-5-189 | 13 | 10 | 12 | 2 | |
| 3984 | B-2-9 | 18 | 4 | 7 | 14 | |
| 3988 | T-2-229 | 6 | 7 | 11 | 3 | |
| 3995 | S-4-99 | 12 | 6 | 9 | 0 | |
| 4001 | T-3-319 | 5 | 4 | 7 | 6 | |
| 4035 | T-1-193 | 2 | 0 | 1 | 5 | |
| 4089 | S-4-279 | 15 | 0 | 6 | 2 | |
| 4111 | S-2-297 | 10 | 4 | 4 | 7 | |
| 4154 | B-2-261 | 17 | 11 | 12 | 14 | |
| 4290 | T-2-103 | 3 | 3 | 13 | 1 | |
| 4293 | B-1-9 | – | – | 10 | 14 | Deactivated |
| 4305 | S-1-261 | 9 | 9 | 9 | 3 | Deactivated |
| 4333 | S-4-63 | 12 | 0 | 7 | 2 | |
| 4399 | S-4-225 | 14 | 3 | 9 | 1 | |
| 4405 | S-2-315 | 10 | 7 | 4 | 6 | |
| <i>continued on next page</i> | | | | | | |

| <i>continued from previous page</i> | | | | | | |
|-------------------------------------|-----------------|--------------------------------|----------------------------------|---------------------------------|-----------------------------------|-----------------|
| <i>Serial #</i> | <i>Position</i> | <i>Electronics Board #</i> | <i>Electronics Channel #</i> | <i>High Voltage Board #</i> | <i>High Voltage Channel #</i> | <i>Comments</i> |
| 4415 | S-4-207 | 14 | 0 | 11 | 8 | |
| 4424 | S-5-261 | 14 | 10 | 8 | 11 | Deactivated |
| 4428 | S-1-117 | 7 | 9 | 8 | 1 | |
| 4445 | S-4-189 | 13 | 9 | 12 | 1 | |
| 4451 | S-2-171 | 8 | 7 | 2 | 14 | |
| 4453 | S-4-261 | 14 | 9 | 13 | 9 | |
| 4496 | S-2-135 | 8 | 1 | 8 | 13 | |
| 4521 | S-1-279 | 10 | 0 | 10 | 3 | |
| 4531 | S-5-315 | 15 | 7 | 11 | 4 | |
| 4545 | S-5-117 | 12 | 10 | 6 | 0 | Deactivated |
| 4548 | S-5-81 | 12 | 4 | 11 | 12 | Deactivated |
| 4568 | S-3-315 | 10 | 8 | 13 | 4 | |
| 4573 | T-3-103 | 3 | 4 | 13 | 2 | |
| 4578 | T-1-31 | 4 | 2 | 8 | 9 | |
| 4586 | B-2-153 | 18 | 5 | 12 | 15 | Deactivated |
| 4591 | S-4-135 | 13 | 0 | 13 | 15 | |
| 4595 | B-3-99 | 17 | 8 | 13 | 0 | |
| 4610 | T-3-283 | 5 | 10 | 8 | 4 | |
| 4618 | S-1-171 | 8 | 6 | 8 | 14 | |
| 4628 | T-2-337 | 5 | 1 | 10 | 9 | |
| 4636 | T-2-67 | 3 | 9 | 11 | 1 | |
| 4637 | T-1-229 | 6 | 6 | 13 | 3 | Deactivated |
| 4640 | T-1-67 | 3 | 8 | 12 | 3 | |
| 4644 | S-3-351 | 11 | 2 | 10 | 5 | |
| 4649 | B-1-261 | – | – | – | – | Deactivated |
| 4652 | B-2-279 | 19 | 1 | 13 | 14 | |
| 4679 | S-4-243 | 14 | 6 | 8 | 5 | |
| 4735 | S-5-297 | 15 | 4 | 13 | 5 | Deactivated |
| 4789 | S-3-261 | 9 | 11 | 7 | 10 | |
| 4791 | S-4-333 | 15 | 9 | 11 | 11 | |
| 4807 | T-2-265 | 6 | 1 | 0 | 3 | |
| 4808 | S-5-135 | 13 | 1 | 9 | 12 | |
| 4814 | B-4-63 | – | – | 14 | 15 | Deactivated |
| 4815 | T-2-85 | 3 | 7 | 5 | 0 | Deactivated |
| 4820 | S-1-45 | 11 | 9 | 8 | 12 | |
| 4827 | T-1-85 | 3 | 6 | 6 | 13 | Deactivated |
| 4829 | S-5-279 | 15 | 1 | 13 | 6 | |

continued on next page

| <i>continued from previous page</i> | | | | | | |
|-------------------------------------|-----------------|--------------------------------|----------------------------------|---------------------------------|-----------------------------------|-----------------|
| <i>Serial #</i> | <i>Position</i> | <i>Electronics Board #</i> | <i>Electronics Channel #</i> | <i>High Voltage Board #</i> | <i>High Voltage Channel #</i> | <i>Comments</i> |
| 4833 | T-1-355 | 4 | 8 | 10 | 6 | |
| 4842 | S-5-351 | 16 | 1 | 12 | 9 | Deactivated |
| 4845 | S-4-45 | 16 | 9 | 9 | 7 | |
| 4849 | S-5-333 | 15 | 10 | 6 | 5 | Deactivated |
| 4858 | S-3-153 | 8 | 5 | 0 | 14 | Deactivated |
| 4866 | T-1-265 | 6 | 0 | 11 | 10 | |
| 4867 | S-2-99 | 7 | 7 | 3 | 6 | |
| 4869 | S-1-207 | 9 | 0 | 8 | 10 | |
| 5168 | S-6-117 | 12 | 11 | 4 | 2 | |
| 5258 | B-3-315 | 20 | 8 | 4 | 12 | |
| 5326 | B-4-135 | – | – | 7 | 13 | Deactivated |
| 5374 | B-4-351 | 18 | 3 | 5 | 12 | |
| 5412 | S-6-9 | 16 | 5 | 6 | 6 | Deactivated |
| 6839 | B-4-207 | – | – | – | – | Deactivated |
| 6860 | S-6-189 | 13 | 11 | 14 | 8 | |
| 6862 | S-6-333 | 15 | 11 | 3 | 13 | |
| 6864 | S-6-45 | 16 | 11 | 6 | 7 | |
| 6865 | B-1-297 | 19 | 4 | 5 | 8 | |
| 6873 | S-6-225 | 14 | 5 | 5 | 2 | Deactivated |
| 7078 | S-6-261 | 14 | 11 | 0 | 4 | Deactivated |

Appendix D

Deactivated PMTs

Table D.1: Listing of deactivated PMTs in the Outer Detector

| <i>Serial #</i> | <i>Position</i> | <i>Date Turned Off</i> | <i>Reason for Deactivation</i> |
|-------------------------------|-----------------|----------------------------|------------------------------------|
| 0058 | S-3-117 | November 30, 2001 | Signal path failure |
| 0083 | S-2-279 | November 30, 2001 | Signal path failure |
| 0294 | B-1-99 | November 30, 2001 | Signal path failure |
| 4293 | B-1-9 | November 30, 2001 | Signal path failure |
| 4424 | S-5-261 | November 30, 2001 | Signal path failure |
| 4545 | S-5-117 | November 30, 2001 | Signal path failure |
| 4548 | S-5-81 | November 30, 2001 | Signal path failure |
| 4649 | B-1-261 | November 30, 2001 | Signal path failure |
| 0084 | B-1-207 | November 30, 2001 | High voltage path failure |
| 0128 | S-1-153 | November 30, 2001 | High voltage path failure |
| 3108 | B-1-153 | November 30, 2001 | High voltage path failure |
| 3255 | S-1-351 | November 30, 2001 | High voltage path failure |
| 3267 | B-1-351 | November 30, 2001 | High voltage path failure |
| 3273 | B-1-63 | November 30, 2001 | High voltage path failure |
| 3314 | S-4-117 | November 30, 2001 | High voltage path failure |
| 3321 | S-2-207 | November 30, 2001 | High voltage path failure |
| 3519 | S-5-207 | November 30, 2001 | High voltage path failure |
| 3886 | B-3-27 | November 30, 2001 | High voltage path failure |
| 3936 | B-3-243 | November 30, 2001 | High voltage path failure |
| 4735 | S-5-297 | November 30, 2001 | High voltage path failure |
| 4815 | T-2-85 | November 30, 2001 | High voltage path failure |
| <i>continued on next page</i> | | | |

| <i>continued from previous page</i> | | | |
|-------------------------------------|-----------------|----------------------------|------------------------------------|
| <i>Serial #</i> | <i>Position</i> | <i>Date Turned Off</i> | <i>Reason for Deactivation</i> |
| 4849 | S-5-333 | November 30, 2001 | High voltage path failure |
| 4858 | S-3-153 | November 30, 2001 | High voltage path failure |
| 0256 | B-2-63 | December 19, 2001 | Noisy |
| 0261 | B-1-45 | December 19, 2001 | Noisy |
| 0210 | T-3-355 | February 18, 2002 | Noisy |
| 4814 | B-4-63 | February 18, 2002 | Noisy |
| 6873 | S-6-225 | March 4, 2002 | Flasher |
| 0275 | B-2-27 | March 6, 2002 | Noisy |
| 3637 | S-1-243 | March 6, 2002 | Noisy |
| 3653 | S-3-225 | March 6, 2002 | Noisy |
| 3721 | S-6-297 | March 6, 2002 | Flasher. It was noisy in 11/2001 |
| 4305 | S-1-261 | March 6, 2002 | Noisy |
| 3188 | S-5-27 | March 25, 2002 | Flasher. It was noisy in 11/2001 |
| 0255 | B-1-243 | May 2, 2002 | High voltage path failure |
| 4827 | T-1-85 | July 25, 2002 | Noisy |
| 4637 | T-1-229 | September 11, 2002 | Noisy |
| 0185 | B-3-207 | September 13, 2002 | Flasher/noisy tube |
| 3192 | B-2-135 | September 16, 2002 | Noisy. May still work |
| 5412 | S-6-9 | October 11, 2002 | Noisy |
| 0245 | S-3-9 | November 1, 2002 | Noisy |
| 3516 | T-1-247 | November 8, 2002 | Noisy |
| 0006 | B-2-207 | November 11, 2002 | Noisy |
| 0270 | B-1-81 | November 11, 2002 | Noisy |
| 5326 | B-4-135 | November 11, 2002 | Noisy |
| 3039 | T-2-193 | November 13, 2002 | Noisy |
| 0283 | S-6-279 | December 11, 2002 | Noisy |
| 0259 | B-4-279 | January 28, 2003 | Noisy |
| 4586 | B-2-153 | February 24, 2003 | Noisy |
| 0174 | B-1-171 | February 25, 2003 | Noisy |
| 0188 | B-1-189 | February 25, 2003 | Noisy |
| 0214 | S-6-207 | March 10, 2003 | Noisy |
| 0287 | S-6-99 | March 10, 2003 | Noisy |
| 3139 | T-2-49 | March 13, 2003 | Noisy |
| 0165 | B-3-351 | May 10, 2003 | Noisy |
| 0172 | B-3-135 | May 10, 2003 | Noisy |
| 3540 | S-2-189 | May 10, 2003 | Noisy |
| 4842 | S-5-351 | May 10, 2003 | Noisy |
| <i>continued on next page</i> | | | |

| <i>continued from previous page</i> | | | |
|-------------------------------------|-----------------|----------------------------|------------------------------------|
| <i>Serial #</i> | <i>Position</i> | <i>Date Turned Off</i> | <i>Reason for Deactivation</i> |
| 7078 | S-6-261 | May 10, 2003 | Noisy |
| 0271 | S-2-351 | May 24, 2003 | Noisy |
| 0019 | S-4-27 | Unknown | Noisy |
| 0067 | S-3-207 | Unknown | Noisy |
| 0071 | S-5-153 | Unknown | Noisy |
| 0247 | B-2-315 | Unknown | Noisy |
| 0272 | T-1-175 | Unknown | Noisy |
| 0289 | B-1-135 | Unknown | Noisy |
| 0290 | B-2-171 | Unknown | Noisy |
| 3146 | S-3-279 | Unknown | Noisy |
| 3181 | S-3-189 | Unknown | Noisy |
| 3211 | S-6-153 | Unknown | Noisy |
| 3361 | T-2-283 | Unknown | Noisy |
| 3938 | S-5-225 | Unknown | Noisy |
| 6839 | B-4-207 | Unknown | Noisy |

Bibliography

- [Agl99] M. Aglietta et al. *Measurement of the Neutron Flux Produced by Cosmic-Ray Muons with LVD at Gran Sasso*. In *Proceedings of the 26th International Cosmic Ray Conference*, volume 2, page 44, Salt Lake City, Utah, 1999.
- [Ahm02] Q.R. Ahmad et al. *Direct Evidence for Neutrino Flavor Transformation from Neutral-Current Interactions in the Sudbury Neutrino Observatory*. *Physical Review Letters*, **89**(2002) 011301.
- [App94] Application Software Group. *GEANT: Detector Description and Simulation Tool*. CERN, 1994.
- [App95] Application Software Group. *Physics Analysis Workstation: An Introductory Tutorial*. CERN, 1995.
- [Bah98] J.N. Bahcall, P.I. Krastev, and A.Y. Smirnov. *Where Do We Stand with Solar Neutrino Oscillations?* *Physical Review D*, **58**(1998) 1–22.
- [Bau95] G.S. Bauer. *Medium Power Spallation Neutron Sources for Research Applications*. *Neutrons and Their Applications*, Proc. SPIE 2339, (1995) 156–169.
- [Ber00] B. Berger. *KamLAND Electronics Test Data*. KamLAND Note 00-05, 2000.
- [Bev92] P.R. Bevington and D.K. Robinson. *Data Reduction and Error Analysis for the Physical Sciences*. McGraw-Hill Inc., 1992.
- [Bro02] Brookhaven National Laboratory. *Report BNL325*. website URL: <http://www.nndc.bnl.gov/nndc/nudat>, 2002.

- [Bus99] J. Busenitz et al. *Proposal for U.S. Participation in KamLAND*. 1999.
- [Byr95] J. Byrne. *Neutrons, Nuclei, and Matter: An Exploration of the Physics of Slow Neutrons*. Institute of Physics Publishing, Bristol, U.K., 1995.
- [Cas73] G.L. Cassiday, J.W. Keuffel, and J.A. Thompson. *Calculation of the Stopping-Muon Rate Underground*. *Physical Review D*, **7**(1973) 2022–2031.
- [Cha02] V. Chazal et al. *Investigation of Fast Neutron Production by 190 GeV/c Muon Interactions on Different Targets*. *Nuclear Instruments and Methods, Section A*, **490**(2002) 334–343.
- [Coo97] N.G. Cooper et al. *Celebrating the Neutrino*. Technical Report 25, Los Alamos National Laboratory, 1997.
- [Cow56] C.L. Cowan, Jr., F. Reines, F.B. Harrison, H.W. Kruse, and A.D. McGuire. *Detections of the Free Neutrino: A Confirmation*. *Science*, **124**(1956) 103.
- [Dan62] G. Danby et al. *Observation of High-Energy Neutrino Reactions and the Existence of Two Kinds of Neutrinos*. *Physical Review Letters*, **9**(1962) 36.
- [Egu03] K. Eguchi et al. *First Results from KamLAND: Evidence for Reactor Anti-Neutrino Disappearance*. *Physical Review Letters*, **90**(2003).
- [Fas88] G. Fasano and R. Vio, 1988. website URL: <http://lib.stat.cme.edu/multi/leiv2>.
- [Fuj01] B. Fujikawa. *Estimation of the Mean Neutron Capture Time in the KamLAND Scintillator*. KamLAND Note 01-09, 2001.
- [Fuk98] Y. Fukuda et al. *Measurement of the Solar Neutrino Flux from Super-Kamiokande's First 300 Days*. *Physical Review Letters*, **81**(1998) 1158–1162.
- [Hag00] T. Hagner et al. *Muon-Induced Production of Radioactive Isotopes in Scintillation Detectors*. *Astroparticle Physics*, **14**(2000) 33–47.
- [Hag02] K. Hagiwara et al. *The Review of Particle Physics*. *Physical Review D*, **66**(2002).
- [Ham00] Hamamatsu Corporation, 2000. website URL: <http://usa.hamamatsu.com/cmp-glossary/current-amp.htm>.

- [Jel58] J.V. Jelley. *Čerenkov Radiation and Its Applications*. Pergammon Press, New York, 1958.
- [Kha83] F.F. Khalchukov et al. *High Energy Hadron Background in Proton Decay Experiments*. *Il Nuovo Cimento*, **6C**(1983) 320–326.
- [Kod01] K. Kodama et al. *Observations of Tau Neutrino Interactions*. *Physics Letters B*, **504**(2001) 218–224.
- [Mes01] J.A. Messimore, L. DeBraeckeleeer, C.R. Gould, H.J. Karwowski, D.M. Markoff, K. Nakamura, and W. Tornow. *Installation and Assembly of the KamLAND Outer Detector*. Triangle Universities Nuclear Laboratory Progress Report, **XL**(2001) 84–87.
- [Per00] D.H. Perkins. *Introduction to High Energy Physics*. Cambridge University Press, Cambridge, 2000.
- [Rei53] F. Reines and C.L. Cowan, Jr. *Detection of the Free Neutrino*. *Physical Review*, **92**(1953) 830–831.
- [Roh01] R.M. Rohm, L. DeBraeckeleeer, C.R. Gould, W. Tornow, and A.R. Young. *Simulation of the KamLAND Water-Čerenkov Veto Detector*. Triangle Universities Nuclear Laboratory Progress Report, **XL**(2001) 88–90.
- [Upd63] J. Updike. *From Telephone Poles and Other Poems*. A. Knopf, New York, 1963.
- [Wan01] Y-F. Wang, V. Balic, G. Gratta, A.Fassò, S. Roesler, and A. Ferrari. *Predicting Neutron Production from Cosmic-ray Muons*. *Physical Review D*, **64**(2001).